

POLISH ACADEMY OF SCIENCES – WROCLAW BRANCH
WROCLAW UNIVERSITY OF TECHNOLOGY

ARCHIVES OF CIVIL AND MECHANICAL ENGINEERING

Quarterly
Vol. X, No. 4

WROCLAW 2010

EDITOR IN CHIEF

ZBIGNIEW GRONOSTAJSKI

EDITORIAL LAYOUT AND PROOF-READING

WIOLETTA GÓRALCZYK

TYPESSETTING

SEBASTIAN ŁAWRUSEWICZ

SECRETARY

WIOLETTA GÓRALCZYK

Publisher: Committee of Civil and Mechanical Engineering
of Polish Academy of Sciences – Wrocław Branch,
Faculty of Civil Engineering and Faculty of Mechanical Engineering
of Wrocław University of Technology

© Copyright by Oficyna Wydawnicza Politechniki Wrocławskiej, Wrocław 2010

OFICyna WYDAWNICZA POLITECHNIKI WROCLAWSKIEJ

Wybrzeże Wyspiańskiego 27, 50-370 Wrocław

<http://www.oficyna.pwr.wroc.pl>

e-mail: ofiewyd@pwr.wroc.pl

ISSN 1644-9665

Drukarnia Oficyny Wydawniczej Politechniki Wrocławskiej. Zam. nr 1010/2010.

Contents

B. BARTCZAK, D. GIERCZYCKA-ZBROZEK, Z. GRONOSTAJSKI, S. POLAK, A. TOBOTA, The use of thin-walled sections for energy absorbing components: a review	5
M. DZIEDZIC, S. TURCZYN, Experimental and numerical investigation of strip rolling from dual phase steel	21
M. HYRCZA-MICHALSKA, J. ROJEK, O. FRUITOS, Numerical simulation of car body elements pressing applying tailor welded blanks – practical verification of results	31
M. KOWALIK, Application of longitudinal cold rolling method in mass production of stepped shafts used in combustion engines	45
M. PIETRZYK, Ł. MADEJ, Ł. RAUCH, R. GOŁĄB, Multiscale modelling of microstructure evolution during laminar cooling of hot rolled DP steels	57
W. PRESZ, R. CACKO, Analysis of the influence of a rivet yield stress distribution on the micro-SPR joint – initial approach	69
H. SADŁOWSKA, A. KOCANĀDA, On the problem of material properties in numerical simulation of tube hydroforming	77
F. STACHOWICZ, T. TRZEPIECIŃSKI, T. PIEJA, Warm forming of stainless steel sheet	85
T. TRZEPIECIŃSKI, 3D elasto-plastic FEM analysis of the sheet drawing of anisotropic steel sheet	95
K. ŻABA, The influence of heat treatment on selected physical properties of aluminized steel strips.....	107

Spis treści

B. BARTCZAK, D. GIERCZYCKA-ZBROZEK, Z. GRONOSTAJSKI, S. POLAK, A. TOBOTA, Zastosowanie profili cienkościennych na elementy pochłaniające energię: przegląd	5
M. DZIEDZIC, S. TURCZYN, Badania laboratoryjne i analiza numeryczna procesu walcowania taśm ze stali <i>dual phase</i>	21
M. HYRCZA-MICHALSKA, J. ROJEK, O. FRUITOS, Praktyczna weryfikacja rezultatów symulacji numerycznej tłoczenia elementów karoserii samochodowej z wsadów spawanych laserem	31
M. KOWALIK, Zastosowanie metody walcowania wzdłużnego na zimno w masowej produkcji wałków stopniowanych w silnikach spalinowych	45
M. PIETRZYK, Ł. MADEJ, Ł. RAUCH, R. GOŁĄB, Wieloskalowy model rozwoju mikrostruktury podczas laminarnego chłodzenia stali DP walcowanych na gorąco	57
W. PRESZ, R. CACKO, Wpływ rozkładu naprężenia uplastyczniającego w mikronicie na możliwość powstania połączenia w procesie mikro-SPR	69
H. SADŁOWSKA, A. KOCANĀDA, Własności materiałowe w modelowaniu komputerowym kształtowania hydromechanicznego rur	77
F. STACHOWICZ, T. TRZEPIECIŃSKI, T. PIEJA, Kształtowanie na półgorąco blachy ze stali odpornej na korozję	85
T. TRZEPIECIŃSKI, Sprężysto-plastyczna analiza 3D procesu wytłaczania blach stalowych anizotropowych za pomocą MES	95
K. ŻABA, Wpływ obróbki cieplnej na wybrane właściwości fizyczne aluminiowanych taśm stalowych	107

The use of thin-walled sections for energy absorbing components: a review

B. BARTCZAK, D. GIERCZYCKA-ZBROŹEK, Z. GRONOSTAJSKI,
S. POLAK, A. TOBOTA

Wrocław University of Technology, Wyrzeże Wyspiańskiego 25, 50-370 Wrocław, Poland.

This paper presents the key aspects of the use of thin-walled sections for collision energy absorbing components. The process of deformation of thin-walled structures and the parameters expressing their energy absorption are described in detail. The research on improving the energy absorption of thin-walled sections, through the use of, e.g., tailored blanks, polyurethane foams and mechanical joining methods, conducted for many years in the Institute of Production Engineering and Automation at Wrocław University of Technology is reported.

Keywords: *energy absorption, thin-walled structures, press joining, tailored blanks*

1. Introduction

Although vehicle designs and road infrastructure are constantly improved, it is not possible to completely eliminate road accidents. Traffic collisions often result in serious and even fatal injuries to the persons involved. Therefore the aim of engineers working in the field of passive safety is to minimize the consequences of an accident when the latter cannot already be avoided. Car passive safety components include systems which absorb energy during a crash. The role of structures designed to deform

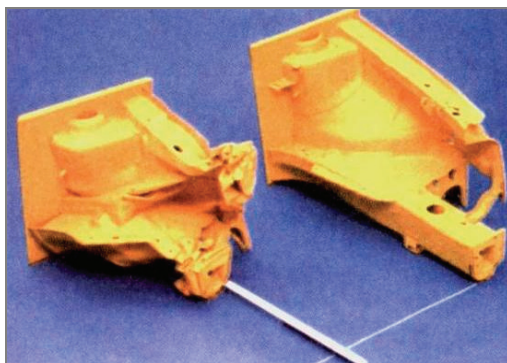


Fig. 1. Collision energy absorbing thin-walled components [7]

(Figure 1) is to reduce not only the loads acting on the passengers inside the vehicle but also the ones acting on the persons involved in the accident who are outside the car (e.g. in collisions involving pedestrians or cyclists) [1–6].

In order to design the most effective structures the new ideas are searched. The aim of paper is to present the major researched carried out at the Engineering Forming Department at Wrocław University of Technology which concerned application of tailored blanks, polyurethane foams and mechanical joining in energy absorbing thin-walled components.

2. Deformation of thin-walled components

The load-bearing capacity of thin-walled components is mostly determined by their stability and when they are allowed to work after they lose stability. The fact that a thin-walled structure loses its stability under load (even a critical one) does not mean that its load-bearing capacity is exhausted or that the structure will fail. For example, in the case of longitudinal car members it is a desirable phenomenon owing to which kinetic collision energy is gradually converted into the energy of the plastic deformation of the structure. A properly designed car body may significantly reduce the range of overloads acting on the passengers during a car crash and so reduce the likely injuries.

In the literature on energy absorption by structures one can find various parameters describing the thin-walled structure's ability to absorb kinetic energy. The parameters enable comparative analyses of different sections. Usually the following parameters: P_{\max} , P_m , CFR , γ are used for this purpose [8–10].

Maximum impact force P_{\max} is the force registered during the formation of the first progressive deformation fold. The maximum force value determines the form and way in which the structural components responsible for energy absorption begin to deform. Average impact force P_m , indicating the component's capacity to absorb kinetic energy, is defined as a ratio of absorbed energy E to total specimen shortening δ . The value of this force versus time is the key parameter for car designers.

$$P_m = \frac{E}{\delta}. \quad (1)$$

The impact force effectiveness coefficient, calculated as a ratio of average force P_m to greatest initial-deformation force P_{\max} , is a measure of the tested component's plastic deformability.

$$CFE = \frac{P_m}{P_{\max}}. \quad (2)$$

Deformability coefficient γ is defined as the progressive shortening δ of section to its total length l :

$$\gamma = \frac{\delta}{l}. \quad (3)$$

The behaviour of a thin-walled component subjected to quasi-static load can be divided into the following stages (Figure 2):

1. uniform compression,
2. global bending,
3. local collapse of the component's middle or end cross section.

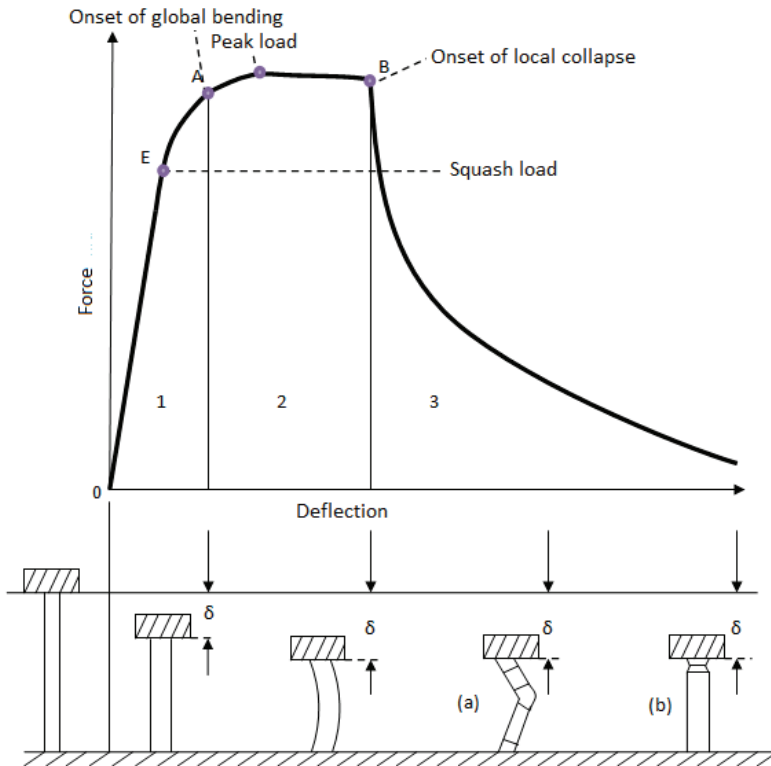


Fig. 2. Stages in behaviour of thin-walled column under quasi-static load [11]

Uniform compression in the elastic range accompanies loading up to point E, passing into the elastic-plastic range (between points E and A). Bifurcation point A corresponds to Eulerian buckling. In the transitional zone (denoted as range A–B), the local collapse mechanism is triggered. Point B corresponds to the onset of the failure mechanism characteristic for the given geometrical parameters of the test piece. If the

cross section in the middle of the column undergoes deformation before the column's end cross section is deformed, global bending will occur (a). If deformation begins in the column's end cross section, progressive folding will occur (b) [11].

Abramowicz et al. [11] tested 128 thin-walled columns rectangular and circular in cross section and differing in their shape factor. The shape factor was defined as a ratio of wall width to wall thickness for the rectangular column and as a ratio of diameter to wall thickness for the circular column. The shape factor ranged from 5.5 to 38 for the rectangular columns and from 9.6 to 48 for the circular columns. The range of column length was so chosen as to ensure the observation of both global bending and folding. For the rectangular columns the column length/wall width ratio was in a range of 2.4–51.2 and the column length/diameter ratio for the circular columns was in a range of 2.2–35.9. The test pieces were subjected to quasi-static compression in a strength tester and dynamically deformed by means of a drop hammer.

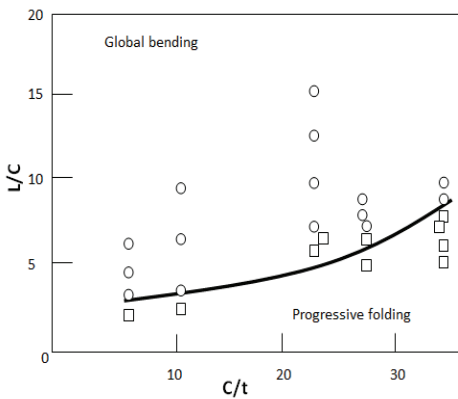


Fig. 3. Deformation of thin-walled columns rectangular in cross section, subjected to quasi-static load [11]. \square – progressive folding, o – global bending, C/t – ratio of wall width to wall thickness, L/C – ratio of column length to wall thickness

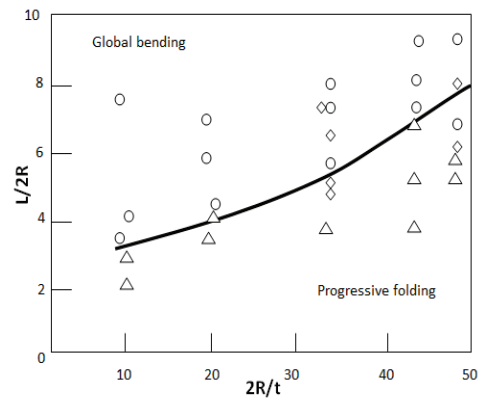


Fig. 4. Deformation of thin-walled columns circular in cross section, subjected to quasi-static and dynamic load [11]. Δ – progressive folding, o – global bending, \square – transition from progressive folding to global bending in advanced stage of deformation, $2R/t$ – ratio of diameter to wall thickness, $L/2R$ – ratio of column length to diameter

The behaviour of stocky columns, i.e. whose ratio of length to wall thickness or diameter is low, (below the curve in Figures 3 and 4) contrasts with the behaviour of slender columns (above the curve in Figures 3 and 4). In the case of dynamic load, the main factors influencing the course of thin-walled section deformation are: the transitional reaction and the effects connected with inertia and stress propagation. In the most cases collapse starts progressing from the column's side being impacted. Depending on the column's slenderness the collapse may have the form of global bending or progressive folding. A column which started to progressively fold may still undergo bending, even in a very advanced stage of squashing [11].

3. Tailored blanks

Tailored blanks are made from sheets of steel differing in its, thickness and strength [12, 20–21]. The sheets are joined together by laser welding and formed into profile parts joined together (usually) by spot welding (Figure 5). The size of the welds must be such as to ensure proper strength of the joints and spacing of joints guarantees progressive deformation. The available literature does not supply much information on the dynamic deformation of collision energy absorbing sections made of laser welded metal sheets.

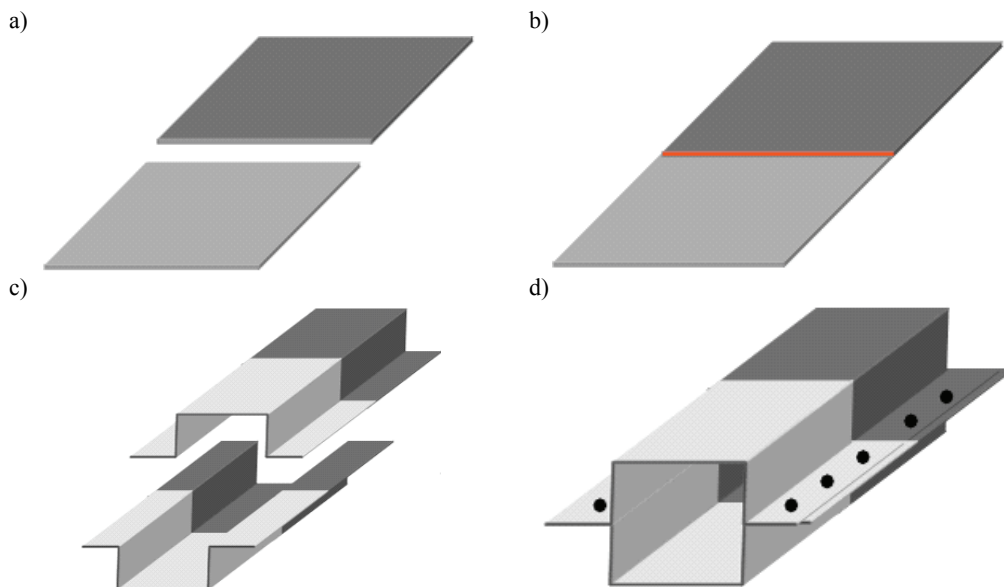


Fig. 5. How tailored blanks are made: a) component parts are cut out from (specified grade) steel sheets, b) are welded by laser, c) formed into profiles and d) joined by spot welding [10]

Two types of thin-walled sections with different percentages of the particular steels: 50%USB+50%DC01 and 25%USB+75%DC01 (denoted respectively USB50-DC50 and USB25-DC75) were tested as part of the research into energy absorption by tailored blanks carried out in the Institute of Production Engineering and Automation [10]. The chemical composition and the properties of the steels are presented in Table 1.

Table 1. Chemical composition and properties of steels used in tested tailored blanks

Steel symbol	Maximum concentration of elements, %									Mechanical properties		
	C	P	S	Mn	Ti	Si	Ni	Cu	Cr	R_e , MPa	R_m , MPa	A , %
DC01	0.1 2	0.04 5	0.04 5	0.6	0.0 5	–	–	–	–	280	410	32
USB	0.0 4	0.00 7	0.00 9	0.2 5	–	0.0 2	0.0 2	0.0 4	0.0 3	220	380	31

The aim of the tests was to investigate the way in which the thin-walled components folded and absorbed energy. The specimens were upset forged by means of a drop hammer with a 100.5 kg rammer and a striking velocity of 6.7 m/s. Rammer deceleration was registered by a piezoelectric accelerometer.

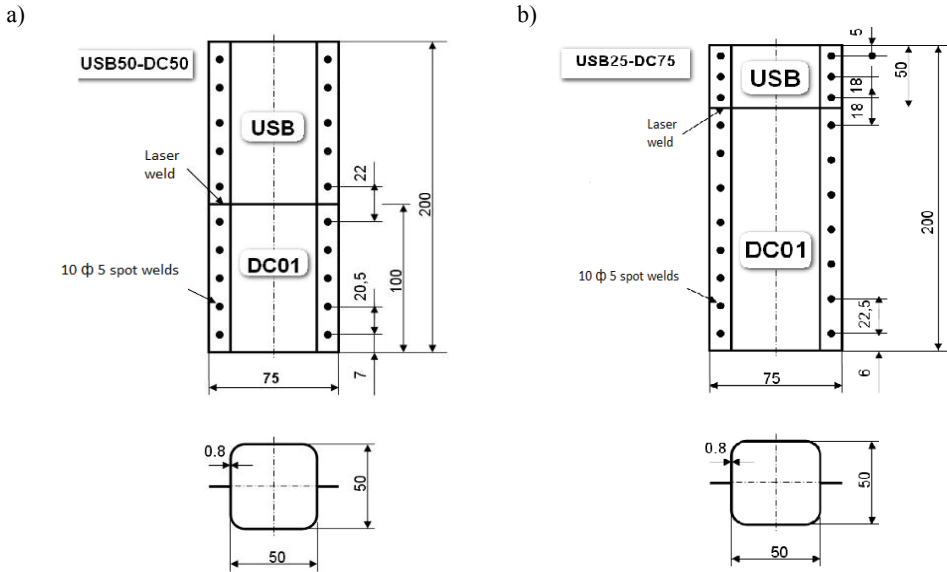


Fig. 6. Outlines of tailored blanks used in dynamic tests: USB50-DC50 – tailored blank containing 50% of steel USB and 50% steel DC01, USB25-DC75 – tailored blank containing 25% of steel USB and 75% of steel DC01 [10]

The thin-walled sections were struck from end made from the more deformable steel (USB) sheet. The deformed test pieces are shown in Figure 7. In both cases, the USB part of the test piece did not absorb the whole kinetic energy of the rammer and sheet DC01 deformed. For all the tested tailored blanks advantageous progressive deformation was observed and no cracks appeared in the laser weld.

Figure 8 shows the dependence between displacement and energy absorption. In the case of tailored blank USB25-DC75, for a displacement larger than 45 mm energy absorption intensifies because then the stronger steel DC01 begins to deform. A similar situation occurs towards the end of deformation of section USB50-DC50. Test pieces USB25-DC75 absorbed collision energy faster because of the higher percentage of the stronger sheet. In the case of tailored blank USB25-DC75 a higher value (56%) of the coefficient of effectiveness (*CFE*) was obtained, which is advantageous with regard to force variation minimization during a collision (Table 2) [10].

Table 2. Parameters describing capacity to absorb energy by tested tailored blanks, defined by relations (1–3)

Type of tailored blank	δ mm	P_m kN	CFE %	P_{max} kN	γ %
USB50-DC50	99	22.7	40	57.3	50
USB25-DC75	82	25.1	56	45	40

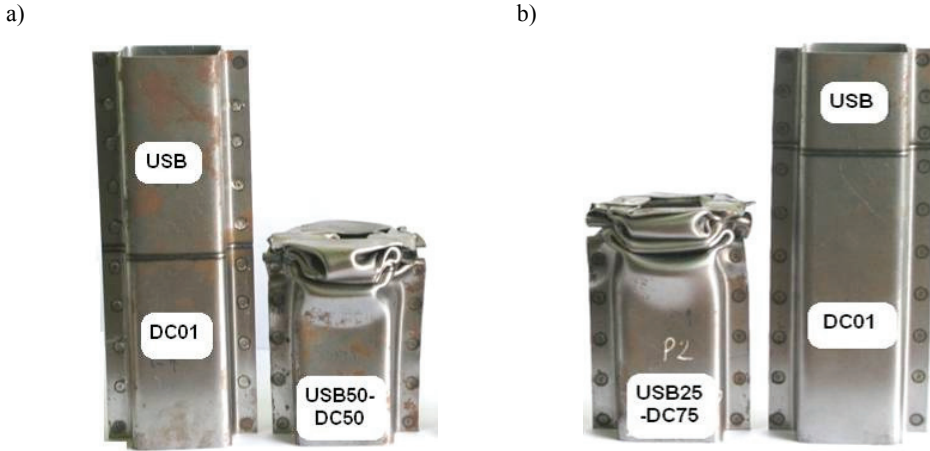


Fig. 7. Tailored blanks before and after deformation: a) tailored blank containing 50% of steel USB and 50% of steel DC01, b) tailored blank containing 25% of steel USB and 75% of steel DC01 [10]

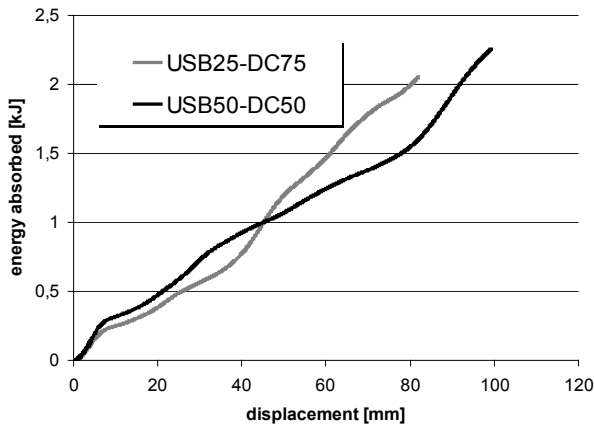


Fig. 8. Amount of absorbed energy versus displacement (the two tailored blanks absorbed a similar amount of energy) [10]

The tests showed that thin-walled sections' energy absorption and the maximum and average deformation force can be controlled through gradient section stiffness. Even better results can be obtained if more than two component parts with progressive change of strength are used.

4. Components filled with foam

In profile filled with foam energy is also dissipated through the bending, deformation and breaking of the cells from which foam is made up. Its other advantages include a low price, very small weight and ease in forming complicated shapes [13].

Figure 9 shows the stress-strain dependence for stiff polyurethane foam subjected to static compression. It is apparent that at low strain (below 5%) linear elasticity is observed and from the slope of the curve one can approximate Young's modulus of the foam. As the force increases, the foam's cells are compressed and crushed until plastic deformation. Gradual upsetting occurs when the force is kept approximately constant (the flat area in the graph) until the foam cell walls come into contact. Then compaction takes place and the stress rapidly increases. The largest amount of energy is absorbed in the area of the almost linear stress increase [13].

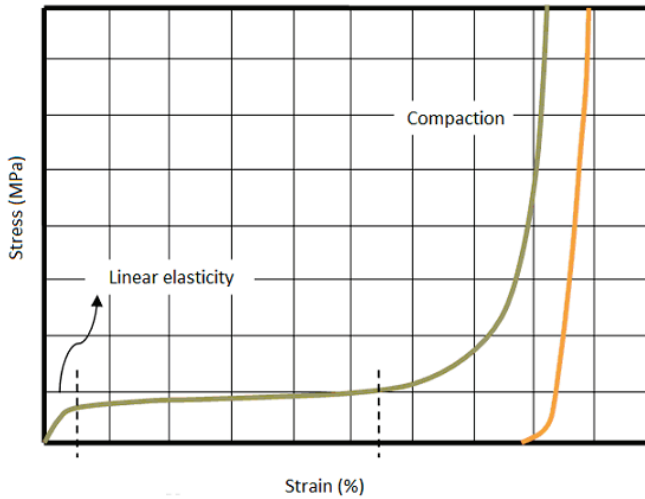


Fig. 9. Typical stress-strain curve for plastic foams under static compression [13]

Figure 10 shows the stress-strain dependence for foams characterized by three different densities. The shaded area under the graph represents the same amount of energy absorbed by the foams. Since it undergoes compaction the lower density foam is capable of absorbing the given amount of energy under large strain. Whereas the higher density foams can absorb the same amount energy under lower strain and higher stress.

The absorbed energy of foam is a function of stress:

$$W = \int_0^{\varepsilon} \sigma(\varepsilon) d\varepsilon. \quad (4)$$

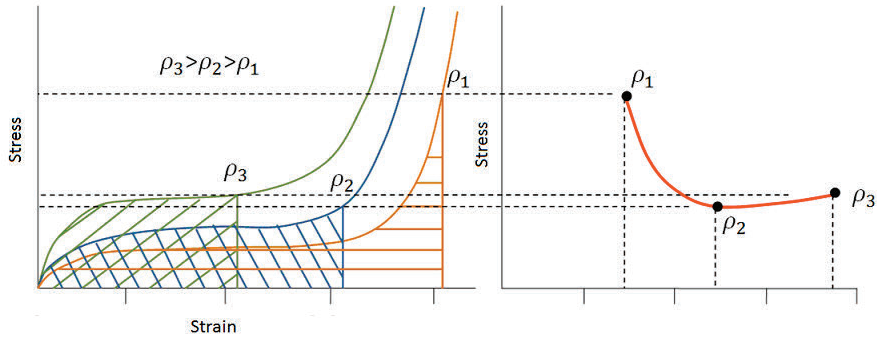


Fig. 10. Stress-strain dependence for foams with different densities [13]



Fig. 11. Comparison of dynamic and static method of upsetting specimens: a) symmetric specimens with single wall and similar packing densities, b) asymmetric specimens with single wall and similar packing densities, c) tubular specimens with similar packing densities, d) asymmetric specimens with double wall and similar packing densities, f) specimens with double wall and similar packing densities [9]

A series of specimens differing in their shape and packing density were made in the Metal Forming Processes Department at Wrocław University of Technology. The specimens were then subjected to upsetting. The deformation shape of the statically and dynamically upset specimens shows that the way in which folds form is similar. There is similarity in the outline of the layers of folds (Figure 11).

An examination of the geometry of the specimens after upsetting shows that the tubular specimens deform most desirably followed by symmetric and asymmetric specimens. In the case of the latter specimens the deformation process is very irregular and the deformation geometry is unrepeatable. An analysis of the energy dissipation results with regard to deformation mode uniformity shows that the best results are obtained for one- and two-layer tubular specimens with a packing density higher than 80 kg/m^3 . Longitudinal members made of such components are currently not used in the construction of cars but considering the way in which they absorb energy and their energy absorption capacity, they are likely to be used as car body reinforcing components in the future.

To sum up, polyurethane foam fillers improve impact energy absorption. Energy dissipation is the better, the higher the density of the filler. However, because of the lower degree of deformation, acceleration is increased.

5. Clinching

Currently the most commonly used methods of joining structural components are spot welding and laser welding [18]. Innovative materials, including ones covered with anticorrosion coatings, are difficult to weld [16, 19]. Moreover, in order to minimize costs, new less expensive methods of joining are sought. An example of such a method is press joining (also called clinching).

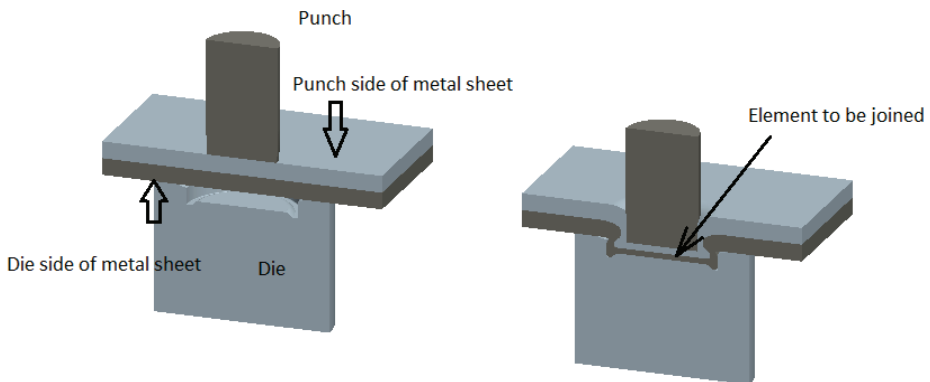


Fig. 12. Successive stages in clinching [15]

Press joining (clinching) enables joining two or more thin metal sheets merely through local plastic deformation. In most cases, cold clinching is used, but novel materials,

such as magnesium alloys, require higher joining temperature because of their limited deformability at ambient temperature [14]. Figure 12 shows the successive stages in clinching according to the Eckold concept [15–16].

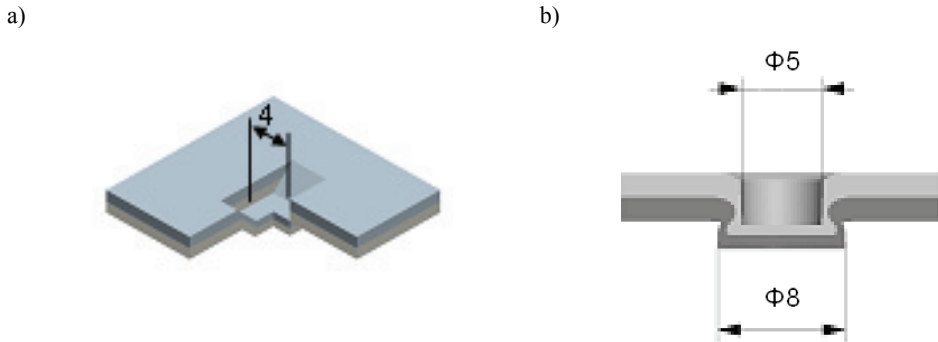


Fig. 13. Types of press joining joints, a) rectangular press joining H-PJ b) round press joining R-PJ [15]

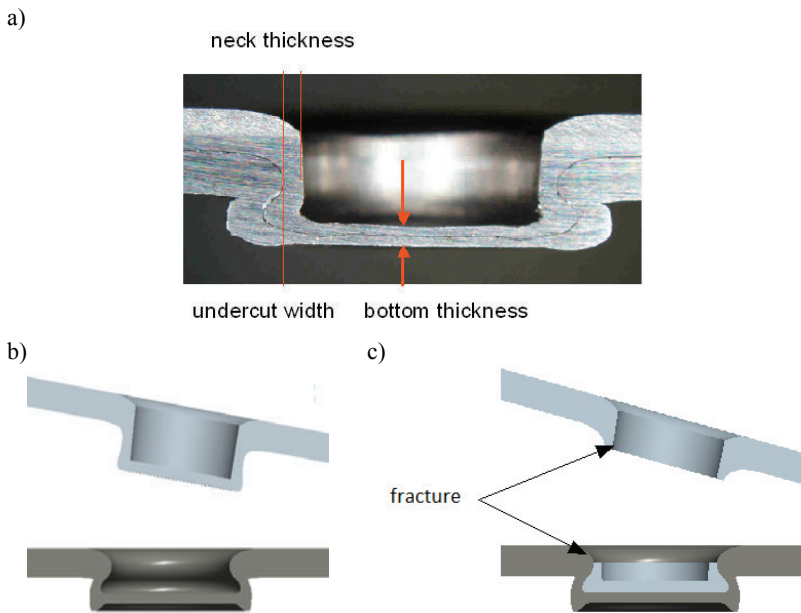


Fig. 14. Cross section of round press joining R-PJ and two types of joint failure [8, 15]

Clinching consists in local pressing of one metal sheet into another metal sheet in order to lock the bottom of the sheet being pressed in against the sheet being pressed out. A protrusion and a cavity form respectively on the pressed out side and the pressed in side of the sheet. The quality of such joints depends on the plasticity of the press joined

materials, the process parameters, the dimensions and shapes of the tools and the magnitude of the pressures proper for the materials being joined.

Depending on the shape of the press joining tools and the cutting/plastic deformation percentage ratio, clinched elements with different geometries are obtained. Figure 13 shows the tested press joining joints used by the firm Eckold.

The cross section of the R-PJ joint together with its characteristic dimensions is shown in Figure 14a. The main parameters which determine the joint failure force are neck thickness and undercut width. If neck thickness is too small, the upper sheet fractures within the neck (Figure 14c). If the undercut is too small, the joint separates without sheet fracture (Figure 14b) [8].

Thanks to its numerous advantages, press joining proves to be particularly useful when other joining methods reach their technological limits or when it is necessary to use an economical and environmentally friendly technology.

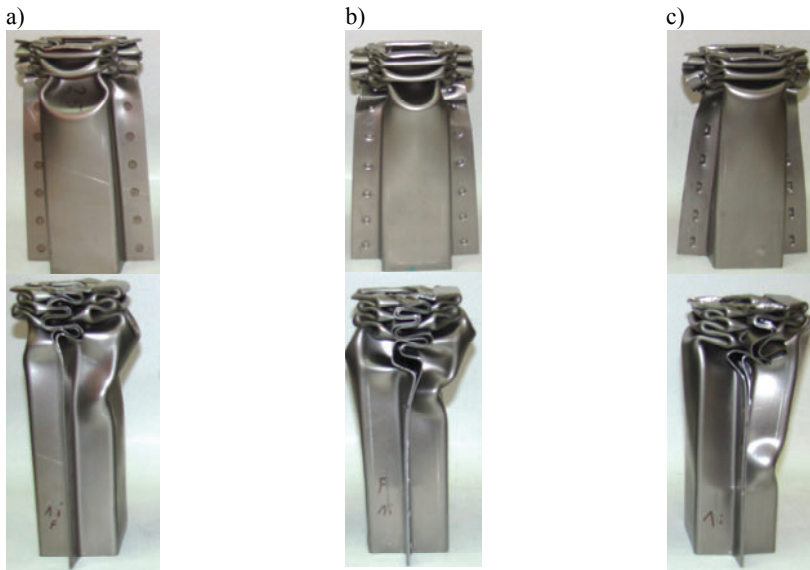


Fig. 15. Deformed thin-walled section joined by: a) spot welding (SW), b) round press joining (R-PJ), c) rectangular press joining (H-PJ) [17]

The tests showed that thin-walled sections joined by round press joining are characterized by the best progressive deformation and the best collision energy absorption parameters (Table 3 and Figure 15 b). Even though the strength of press joining joints is lower than that of welded joints, the forces which such sections can carry and the energy absorption by them (particularly in the case of round press joining) are comparable. Transition from progressive folding to global bending was observed only in the specimens clinched by rectangular press joining, which could have been due to the failure of the joint and results in large displacement.

Table 3. Parameters describing capacity to absorb energy by tested tailored blanks

Designation	δ [mm]	P_{\max} [kN]	P_m [KN]
SW-s1	0.109	312.3	50.2
SW-s2	0.107	327.3	51.3
R-PJ-s1	0.102	303.8	46.8
R-PJ-s2	0.105	293.1	50.8
H-PJ-s1	0.116	276.1	46.0
H-PJ-s2	0.129	312.2	40.3

The test results also indicate that in the case of alloys of aluminium (which is difficult to weld) the difference between the strength of welded joints and that of press joining joints is not large. It should be noted that the strength of press joining joints is more repeatable than that of spot welded joints [17].

Press joining is much cheaper than spot welding. The research showed that press joining can be used to join energy absorbing components in the car industry not only for economic reasons but also because of the limitations of the other joining methods in the case of innovative materials.

6. Conclusion

The research has demonstrated the high energy absorption of thin-walled sections. Designers can choose from the many methods of forming and joining them. Thin-walled sections can be made from various metal sheets and can be joined also by laser welding (tailored blanks). By combining a steels with different strength in tailored blanks profiles one can obtain the desired deformation.

The strength and energy absorption of thin-walled sections can be increased by filling them with polyurethane foam. As the density of the foam increases so does the energy absorption by the section, but also the acceleration increases. In this technology an optimum relation between the density of the foam used and the section's strain range should be worked out.

Press joining (clinching) is a relatively new method of joining thin-walled sections. The most advantageous, considering the deformation mode and the range of absorbed energy, is round press joining. Clinching enables joining aluminium alloys and it is more repeatable than point welding.

Acknowledgements

This research work has been financially supported by the Ministry of Science and Higher Education, grant no. N N508 484838. The licenses of program ProEngineer of Wrocław Centre for Networking and Supercomputing was used in the article.

References

- [1] Wierzbicki T., Andrzejewski H.: *Impulsive loading of viscoplastic cylindrical shells*, Proc. Symp. Plastic Analysis of Structures, Iassy, September, 1972, pp. 461–479.
- [2] Wierzbicki T., Abramowicz W.: *On the crushing mechanics of thin walled structures*, Journal of Appl. Mech., Vol. 50, No. 4a, 1983, pp. 727–734.
- [3] Jones N., Wierzbicki T. Editors.: *Structural crashworthiness and failure*, Amsterdam: Elsevier Applied Science, 1993.
- [4] Hallquist J.O.: *A Procedure for the solution of finite-deformation contact-impact problems by the finite element method*, Lawrence Livermore National Lab. Livermore, 1976.
- [5] Stasiak P.: *New idea of child car seat according to new safety system of participants of road traffic*, Eksploatacja i Niezawodność – Maintenance and Reliability, Issue 4, 2008, pp. 42–48.
- [6] Kisiłowski J., Zalewski J.: *Chosen problems of road accidents analyses in Poland in the period between 1995 and 2004*, Eksploatacja i Niezawodność – Maintenance and Reliability, Issue 1, 2008, pp. 37–43.
- [7] Rusiński E.: *Zasady projektowania konstrukcji nośnych pojazdów samochodowych*, Oficyna Wydawnicza Politechniki Wrocławskiej, Wrocław, 2002.
- [8] Polak S.: *Zastosowanie metod przetłaczania do łączenia profili cienkościennych absorbujących energię podczas zderzenia*, PhD Thesis, Institute of Predication Engineering and Automation, Wrocław University of Technology, Wrocław 2008.
- [9] Gronostajski J., Gronostajski Z., Jaśkiewicz K., Niechajowicz A., Ornatowski D., Struś M., Tobota A., Ziemia H.: *Pochłanianie energii przez wybrane elementy nadwozia podczas dynamicznego obciążania*, Raporty Inst. Technol. Masz. Autom. PWroc., Ser. SPR No. 21, 2003, pp. 274.
- [10] Gronostajski Z., Karbowski P., Polak S.: *Analiza doświadczalna i numeryczna deformacji profilu typu tailored blanks pochłaniającego energię zderzenia*, FIMM 2007, Warszawa, 17–19.05.2007.
- [11] Abramowicz W., Jones N.: *Transition from initial global bending to progressive buckling of tubes loaded statically and dynamically*, International Journal of Impact Engineering, Vol. 19, No. 5–6, 1997, pp. 415–437.
- [12] Grosman F., Hycza-Michalska M.: *Podatność do kształtowania plastycznego wsadów spawanych laserowo*, 17th International Scientific and Technical Conference Design and Technology of Drawpieces and Die Stampings, Poznań, 2008.
- [13] Avalor M., Belingardi G., Montanini R.: *Characterization of polymeric structural foams under compressive impact loading by means of energy – absorption diagram*, International Journal of Impact Engineering, Vol. 25, No. 5, 2001, pp. 455–472.
- [14] Hahn O., Horstmann M.: *Mechanical joining of magnesium components by means of inductive heating – realization and capability*, Materials Science Forum, Vol. 539–543, 2007, pp. 1638–1643.
- [15] Materials obtained from firm ECKOLD.
- [16] Niechajowicz A., Tobota A.: *Dynamic tension testing of DP600, DP800 steel and Al 6061 T4 alloy sheets by means of rotary hammer*, Archives of Metallurgy and Materials, Vol. 54, No. 3, 2009, pp. 647–657.
- [17] Gronostajski Z., Polak S.: *The application of clinching techniques to join impact energy absorbing thin-walled aluminium sections*, Archives of Metallurgy and Materials, Vol. 54, No. 3, 2009, pp. 695–703.

- [18] Rusiński E., Kopczyński A., Czmochowski J.: *Tests of thin-walled beams joined by spot welding*, Journal of Materials Processing Technology, Vol. 157, 2004, pp. 405–409.
- [19] Adamus J.: *Theoretical and experimental analysis of the sheet-titanium forming process*, Archives of Metallurgy and Materials, Vol. 54, No. 3, 2009, pp. 705–709.
- [20] Rojek J., Hycza-Michalska M., Bokota A., Piekarska W.: *Determination of mechanical properties of the weld zone of tailor-welded blanks*, Computer Methods in Materials Science, Vol. 9, No. 1, 2009, pp. 153–158.
- [21] Qarakhani M., Masoumi A., Pashirehpour J.: *Investigation on drawing depth in sheet hydroforming of tailor-welded blanks*, Computer Methods in Materials Science, Vol. 9, No. 1, 2009, pp. 159–165.

Zastosowanie profili cienkościennych na elementy pochłaniające energię: przegląd

Przedstawiono najważniejsze aspekty związane z zastosowaniem struktur cienkościennych w elementach pochłaniających energię zderzenia. Szczegółowo omówiono proces deformacji struktur cienkościennych oraz parametry opisujące ich energochłonność. Opisano także metody poprawy energochłonności struktur cienkościennych łączonych techniką *tailored blanks*, poprzez przetłaczanie mechaniczne oraz wypełnianych pianką poliuretanową, testowane w Instytucie Technologii Maszyn i Automatykacji Politechniki Wrocławskiej.



Experimental and numerical investigation of strip rolling from dual phase steel

M. DZIEDZIC, S. TURCZYN

AGH University of Science and Technology, al. Mickiewicza 30, 30-059 Kraków, Poland.

The paper focuses on hot rolled and fast cooled dual phase (DP) steel strips for automotive application. The analysis carried out in this work includes many tests and experiments such as: dilatometric and plastometric tests, Gleeble simulations of hot rolling process, simulation of strip cooling after rolling and hot rolling of DP steel samples in laboratory conditions.

The main part of the paper contains the results of experimental rolling of DP steel samples in laboratory conditions. Especially, the influence of cooling rate on phase volume fraction and some mechanical properties of DP strips have been analysed. The realized hot rolling with controlled cooling of DP samples in laboratory conditions allowed for obtaining diversified steel microstructure and thus wide range of mechanical properties. The results of the analysis carried out in this work provide the useful data for the designing of thermo-mechanical rolling of DP steel strips.

Keywords: *dual phase steels (DP), thermo-mechanical rolling, Gleeble simulation, mechanical properties*

1. Introduction

Automotive industry requires steel producers to continuously accommodate the production to the consumer's demands. Practically, it brings to a compromise between high cold-workability of steel sheet and rigidity of a car body draw-piece. The steels meeting these requirements include DP steels and belong to the newer type called advanced high strength steels (AHSS). Forecast contribution of these steels to vehicle manufacture of reduced mass is shown in Figure 1. DP steels are a group of low-carbon micro-alloyed steels, whose structure consists of soft ferritic matrix, in which 20–70% of martensite is distributed, Figure 2. Depending on the process route and steel composition, hot rolled strips can have a microstructure containing some quantities of bainite.

DP steels show very high strength as well as ductility, high level of homogeneous strain, good formability, weldability and excellent absorption of mechanical energy during high-speed deformation [1, 8]. Depending on martensite volume fraction, the tensile strength (R_m) ranges from 500 to about 1000 MPa, and total elongation amounts to 12–34 %. The dual-phase structure of these steels results in adequately low yield stress (R_e) and high ultimate tensile strength (R_m), allowing for obtaining sufficiently low R_e/R_m ratio. Soft ferrite facilitates the beginning of plastic deformation, while hard martensite increases the strength of steel [2–3, 5]. DP steels show high strain-hardening

coefficient n , which determines the maximum allowable stretch of sheets. A higher n -value compared to a lower one means a deeper part can be stretched. Microstructural internal stresses occurring during martensite formation increase the density of mobile dislocations that facilitate the beginning of plastic deformation and prevent from the occurrence of discontinuities at the physical yield point. DP steels also show continuous workability with no need to perform temper rolling, the occurrence of BH effect after preliminary deformation as well as low value of the planar anisotropy coefficient of sheets. In spite of excellent properties of DP steels, the automotive industry takes advantage of them only to a small degree [6–7].

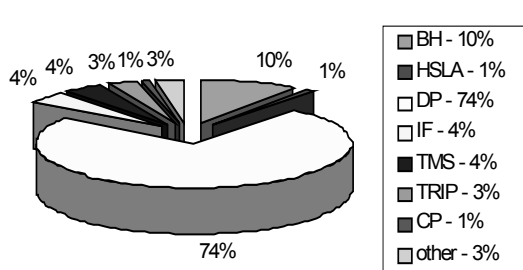


Fig. 1. Forecast contribution of steel grades to the production of a modern car [8]

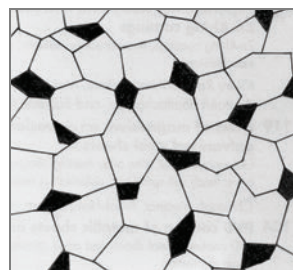


Fig. 2. Islands of martensite in a matrix of ferrite in DP steels

The prevailing technology of DP steel strip production consists of the following processes:

- hot rolling as the thermo-mechanical process,
- cold rolling (after hot rolling) with recrystallization annealing in the two-phase region ($\alpha + \gamma$) and controlled cooling from this region to the temperature of martensite transformation, which aims at avoiding pearlite reaction.

However, the technology that seems to be prevailing in the future is hot strip rolling realized in modern rolling mills integrated with continuous casting of thin ingots.

2. CCT diagram

The samples for tests were prepared from special cast of DP steel (cast A), which was made in laboratory condition. Chemical composition of DP steel was designed according to the standard EN 10336, Table 1. It is close to that of low-carbon deep-drawing steels (DDQ). In order to improve hardenability, it contains increased manganese and silicon content. As the elements facilitating the obtaining of ferritic-

Table 1. Chemical composition of the investigated DP steel (cast A)

C	Mn	Si	Cr	Ni	Mo	Al.
0.10	1.49	0.52	0.04	0.02	0.01	0.06

-martensitic structure after recrystallization annealing, additions of chromium and molybdenum was also applied.

In order to obtain the cooling curves, the start and finish temperatures of phase transformations (critical temperatures), physical simulation of a cooling process was performed using dilatometer (DT1000 type). The critical temperatures (Ac_{1p} , Ac_{1k} , Ac_3 , Ar_3 and Ar_1) were determined with application of the method based on volume difference between austenite and ferrite. In order to construct CCT diagram the specimens from DP steel were austenitized in the temperature range above Ac_3 , and subsequently cooled at different cooling rates, while recording changes in specimen's elongation as a function of temperature. The obtained CCT diagram is shown in Figure 3. The precise CCT curves are the basis to the design of technology allowing for obtaining the most favourable material properties, considering further processing. CCT diagram contains the data about the start and finish temperatures of phase transformations and hardness values obtained in the cooling process with different rates.

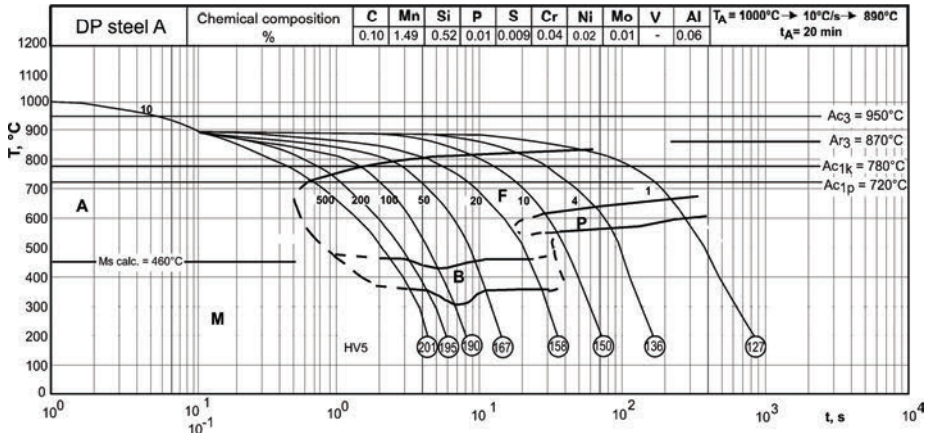


Fig. 3. Detailed CCT diagram obtained for DP steel (cast A)

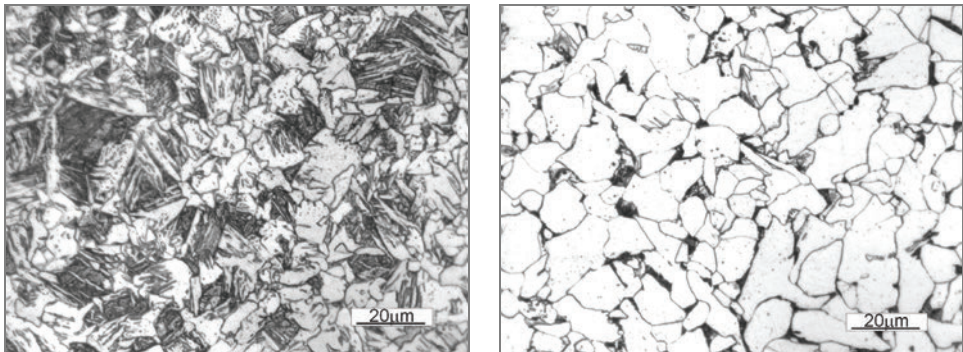


Fig. 4. Microstructure of DP steel after controlled cooling with rate 100 °C/s (left) and 10 °C/s (right)

Particularly, in case of analysed DP steel (cast A) it was found that cooling from finish-rolling temperature at the rate of 100 °C/s leads to obtaining the ferritic-bainitic microstructure with hardness of about 190 HV, Figure 4 (left), while when applying the cooling rate of 10 °C/s the ferritic-pearlitic structure develops, Figure 4 (right).

3. Computer and physical simulation of hot rolling

3.1. Plastometric tests and Gleeble simulation

Prior to computer calculations a series of tests were performed using torsional plastometer. The obtained results in a form of flow stress variations as a function of temperature, strain and strain rate were loaded into computer program as the material database. The example flow stresses for DP steel (cast A) are presented in Figure 5.

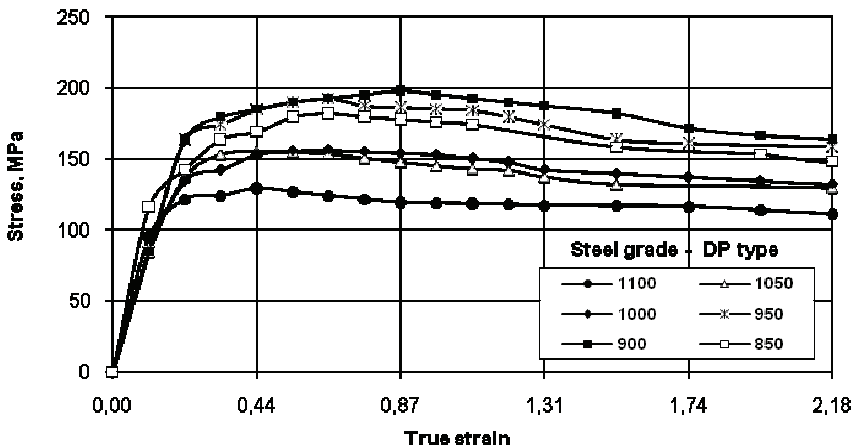


Fig. 5. Flow stresses for DP steel obtained from torsion tests for various temperatures in °C and strain rate equal 2 s⁻¹

Physical modelling of the process of hot rolling in six final passes, as in industrial process, was realized with application of Gleeble 3800 simulator. The test parameters, i.e. temperature of rolled strip, strain, strain rate and idle time between passes, were selected to represent the deformation conditions occurring in real process as precisely as possible. Example results, obtained for rolling of DP strip, are shown in Figure 6. The Gleeble simulations also confirmed results obtained from dilatometric tests. The cooling of specimens from deformation temperature at the rate of 50 °C/s leads to obtaining the ferritic-bainitic structure with hardness of about 180 HV, Figure 7.

The performed plastometric tests, including Gleeble simulations, allowed for determining the changes of flow stress as a function of temperature, strain, and strain rate. Prior to further calculations and tests, these relationships were stored in the material database of computer program.

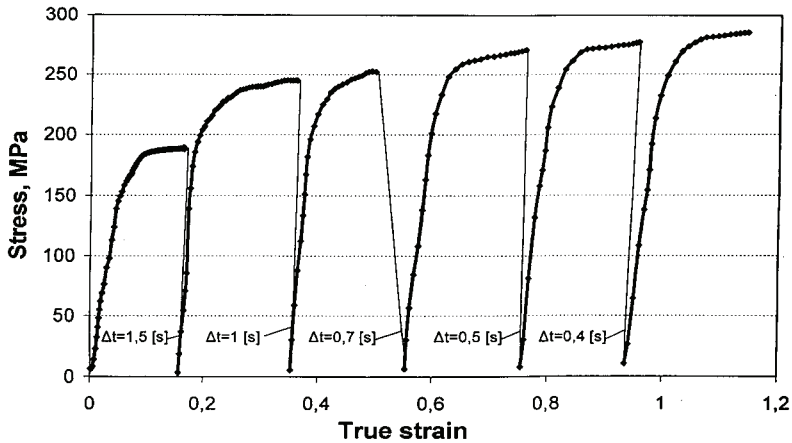


Fig. 6. Simulation of strip rolling in six final passes using Gleeble 3800 (final temperature 890 °C, final strain rate about 100 s⁻¹)

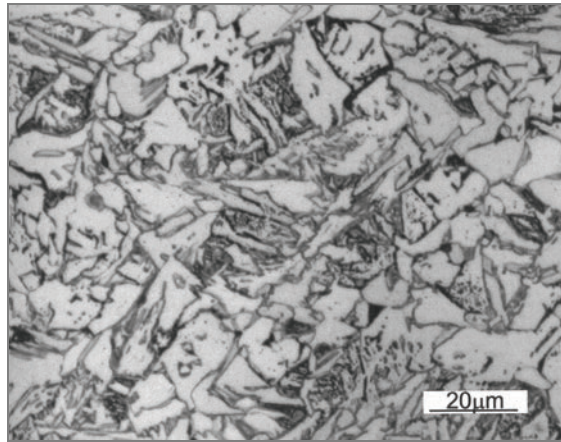


Fig. 7. Microstructure of DP steel obtained from Gleeble simulations after cooling with rate 50 °C/s

3.2. Computer simulation of strip cooling

Numerical methods were used to help proper phase engineering during thermo-mechanical rolling. The process of strip cooling after hot rolling was analysed in detail. In order to obtain evaluation of the roll-end temperatures of the strip, the simulation of hot strip rolling with application of computer program (FormFEM/ROLL) has been applied [4]. The results of calculations contribute also to better understanding of flow pattern of a strip in the roll stands, as well as the distributions of temperature, stresses and strains in a strip being deformed. For simulation of strip cooling after hot rolling commercial software (TTSteel) was used. Cooling rates ranging from 500 °C/s to 1 °C/s were se-

lected and simulation was performed for cooling from the temperature of 890 °C. The chemical compositions of steel as well as cooling temperature-time relationships determined by dilatometer were stored in the program database. The effect of chemical composition on the critical temperatures and time of phase transformations was taken into account basing on the following equations:

$$T(i) = A_0 + \sum [A(i) c(i)] \quad (3)$$

$$S(i) = \exp \{B_0 + \sum [B(i) c(i)]\} \quad (4)$$

where:

- T – critical temperature of the i -th transformation,
- S – time of the i -th transformation,
- A_0, B_0 – regression constants,
- $A(i), B(i)$ – regression coefficients,
- $c(i)$ – content of alloying element.

Regression constants and coefficients in Equations (3) and (4) were computed by the inner code of the program on the basis of known curves of phase transformations. The effect of cooling rate on phase composition and forecast mechanical properties of dual phase steel is presented in Figures 8 and 9.

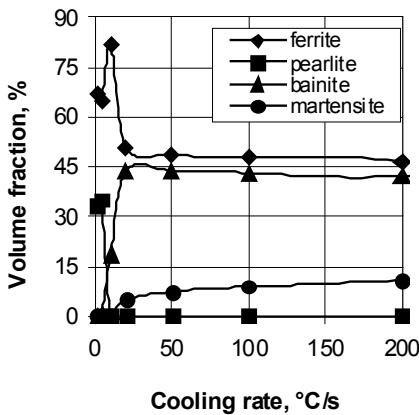


Fig. 8. Influence of cooling rate on phase volume fractions (according to *TSteel* results)

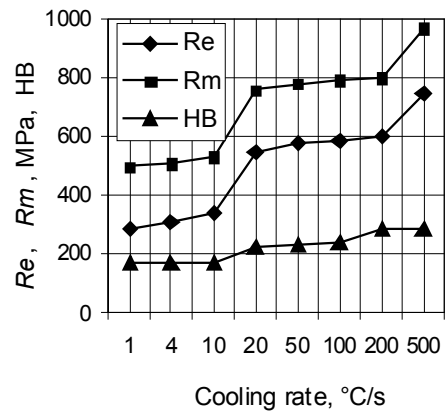


Fig. 9. Influence of cooling rate on mechanical properties (according to *TSteel* results)

The results of calculation confirm that the cooling rate higher than 20 °C/s makes it possible to obtain the ferritic-bainitic-martensitic microstructure, while at the cooling rate lower than 10 °C/s only the ferritic-pearlitic structure develops. The software allows determining the critical temperatures and CCT curves for theoretical cooling

with different cooling rates. It also allows for prediction phase composition and forecast mechanical properties of investigated steels [3–4]. All these investigations were the basis to the planning of further research e.g. rolling parameters of DP samples in laboratory condition.

4. Experimental rolling

The samples for experimental rolling were prepared from special cast of DP steel (cast A). The round ingot of diameter 210/190 mm and length 400 mm was cast in laboratory condition. After head and tail cropping it was preliminary hot deformed to the flat specimens of dimensions $12.4 \times 26.8 \times 120$ mm. These specimens were used in experimental hot rolling and cooling, which schedule is presented in Table 2.

Table 2. Schedule of experimental rolling and controlled cooling of dual phase steel samples

Series	Hot rolling				Cooling
	Heating temp., °C	Roll end temperature	Number of passes	Reductions in the passes, %	Cooling way
2P – A	1250	above Ar ₃	2	2×60	water
2P – B	1250	above Ar ₃	2	2×60	air
3P – C	1250	below Ar ₃	3	2×60 + 1×35	water
3P – D	1250	below Ar ₃	3	2×60 + 1×35	water spray
3P – E	1250	below Ar ₃	3	2×60 + 1×35	air
3P – F	1250	below Ar ₃	3	2×60 + 1×35	water + holding in ferrite region

5. Results and discussion

The complexity of processes taking place in hot rolling conditions creates a wide range of possibilities of controlling the microstructure and mechanical properties of thermo-mechanically treated strips. However, the principal deciding factor is the ensuring of controlled cooling rate, from finish-rolling temperature in austenite range to coiling temperature. The realized rolling of DP samples in laboratory conditions together with controlled cooling allowed for obtaining diversified steel microstructures, depending on the roll-end temperatures and the cooling rates, Table 3.

Some mechanical properties of strip samples obtained after experimental rolling in three passes and controlled cooling with different rate are presented in Figures 10 and 11.

The increase of cooling rate after hot rolling above the critical cooling rate results in increased martensite volume fraction in steel, and thus higher strength and lower formability of investigated strip samples. The cooling rates for different coolants (water, water sprinkle, air) were computing after some tests where thermovision camera (Therma-CAM S60) was applied for recording temperature decrease of the samples.

Martensitic phase prevails (from 66 to 70%) when using water cooling (rate about 100 °C/s) and thus very high strength (R_e , R_m , and HV) and low formability (A_c , A_{50}) of steel strips were obtained. In case of water spray cooling (rate about 15 °C/s), the

bainitic phase (41% for 3P-D samples) was formed. Thus, lower but enough high strength and better formability of strip samples were obtained. When air was used as a coolant (rate about 4 °C/s), only ferritic-pearlitic microstructures were observed.

Table 3. Average content of phase fraction in DP steel after thermo-mechanical rolling

Series	Roll end temperature, °C	Phase content ^{*)} %
2P – A	909	F–30.4; M–69.6
2P – B	880	F–66.0; P–34.0
3P – C	787	F–34.4; M–65.6
3P – D	747	F–59.3; B–40.7
3P – E	725	F–79.0; P–21.0
3P – F	768	F–69.4; M–19.1; B–11.5

^{*)} F – ferrite, M – martensite, B – bainite

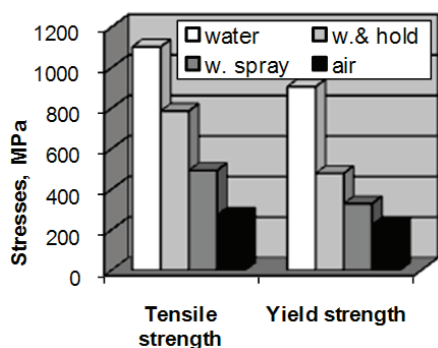


Fig. 10. Comparison of tensile strength and yield strength for strip samples rolled in three passes

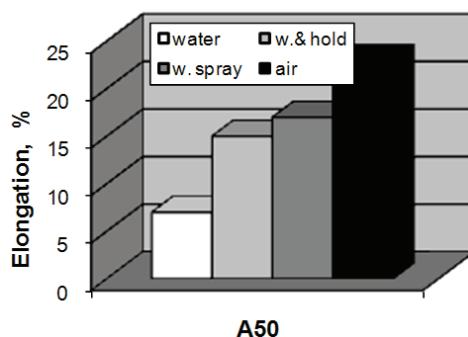


Fig. 11. Comparison of elongations (A_{50}) for strip samples rolled in three passes

However, the best results were obtained when water cooling with holding inside ferrite region (about 7 s) was applied (3P–F samples). In this case hot rolled strips had microstructure containing much lower of martensite (19.1 %) and some quantities of bainite (11.5 %). The obtained microstructure results in adequately low yield stress ($R_e = 479$ MPa) and high ultimate strength ($R_m = 786$ MPa), allowing for obtaining sufficiently good R_e/R_m ratio (equal 0.61) and acceptable level of cold formability ($A_{50} = 15\%$). By combining a number of different microstructures a wide range of mechanical properties of DP steel strips are possible for obtaining. This shows that rolling mills can adjust processing of DP strips to meet the applications requirements demanded by the automotive industry.

6. Conclusions

The results of investigations presented in this work provide useful information for the designing of hot rolling of dual phase steel strips as the thermo-mechanical process.

Although, the industrial hot rolling process requires more complex data, the obtained results can be very useful for the designing or adjusting such processes. For example it can be taken into consideration in the new built hot strip mill $L = 2250$ mm. The obtained results also allow for formulating the more general conclusions:

1. The analysis of strip cooling after hot rolling with application of dilatometric tests and *TTSteel* program allows evaluating important process parameters, used in further research. The obtained results show that the cooling rate higher than 20 °C/s makes it possible to obtain the ferritic-martensitic (or bainitic) microstructure, while at the cooling rate lower than 10 °C/s only the ferritic-pearlitic microstructure develops.

2. The most satisfactory results of experimental rolling were obtained when water-cooling with holding inside ferrite region was applied (3P–F samples). In this case hot rolled strips had microstructure containing much lower of martensite (19.1%) and some quantities of bainite (11.5%). The obtained microstructure results in adequately low yield stress ($R_e = 479$ MPa) and high ultimate strength ($R_m = 786$ MPa), allowing for obtaining very good R_e/R_m ratio (equal 0.61) and acceptable level of cold formability ($A_{50} = 15\%$).

3. By combining a number of different microstructures a wide range of mechanical properties of DP steel strips are possible for obtaining. This allows rolling mills to adjust process parameters to meet market requirements, especially demanded by the automotive industry.

4. The complexity of industrial hot rolling process requires more detailed investigations than were made in this work. However, the results of the analysis provide useful data for the designing of thermo-mechanical rolling of DP steel strips or adjusting existing processes to meet very high requirements demanded by the automotive industry.

Acknowledgements

Financial assistance of Polish Ministry of Science and Higher Education (AGH Project No. 11.11.110.939) is acknowledged.

References

- [1] Bleck W., Papaefthymiou S., Frehn A.: *Microstructure and tensile properties in DP and TRIP steels*, Proc. of Conf. for Mechatronics, Patras, 2004, pp. 55–61.
- [2] Bodin A., Flemming J., Jansen E.F.M.: *Development of as-hot-rolled low-silicon and micro alloyed dual-phase steels*, Proc. of Conf. 42nd MWSP, ISS, Vol. 38, Ontario, 2000, pp. 563–571.
- [3] Dziedzic M., Turczyn S.: *Mechanical properties of dual phase steel strips obtained in thermomechanical rolling process*, Hutnik – Wiadomości Hutnicze, Vol. 73, No. 12, 2006, pp. 551–557.
- [4] Dziedzic M., Turczyn S.: *Thermomechanical rolling of dual phase steel strips*, Proc. of 5th Int. Conf. on Industrial Tools, Velenje, Celje, 2005, pp. 197–202.

- [5] Pichler A, Hribering G., Angerer R.: *Aspects of the production of dual phase and multiphase steel strips*, Proc. of Conf. 41st MWSP, ISS, Vol. 37, Baltimore, 1999, pp. 37–59.
- [6] Reichert B., Freier K.: *Stahlwerkstoffe für den modernen Leichtbau*, Proc. of Conf. Meform, 2003, Freiberg, pp. 104–118.
- [7] Turczyn S., Dziedzic M.: Rolling of car body sheets made from new generation steel, *Hutnik – Wiadomości Hutnicze*, Vol. 69, No. 4, 2002, pp. 126–132.
- [8] www.ulsab-avc.org. *Ultra light steel auto body advanced vehicle technology (ULSAB-AVC) programme*, Date of access: February, 2008.

Badania laboratoryjne i analiza numeryczna procesu walcowania taśm ze stali *dual phase*

Artykuł dotyczy procesu walcowania na gorąco i następnie szybkiego chłodzenia taśm ze stali ferrytyczno-martenzytycznej (*dual phase*), przewidzianych do budowy samochodów. Prowadzona analiza wykorzystywała wiele metod i technik badawczych m.in.: badania dylatometryczne, próby skręcania na plastometrze, symulacje procesu walcowania na maszynie Gleeble i obliczenia numeryczne procesu chłodzenia po walcowaniu oraz obszerne badania procesu walcowania i chłodzenia stali DP w warunkach laboratoryjnych.

Główną część artykułu stanowią badania i wyniki uzyskane podczas walcowania próbek ze stali DP w warunkach laboratoryjnych. W szczególności analizowano wpływ szybkości chłodzenia po walcowaniu na skład fazowy i niektóre własności mechaniczne. Przeprowadzone badania w warunkach laboratoryjnych pozwoliły na otrzymanie dosyć zróżnicowanych pod względem fazowym mikrostruktur i w efekcie własności mechanicznych w dosyć szerokim zakresie. Badanie te dostarczają cennych informacji, niezbędnych dla zrozumienia i prawidłowego projektowaniu cieplno-plastycznego procesu walcowania taśm ze stali typu DP.



Numerical simulation of car body elements pressing applying tailor welded blanks – practical verification of results

M. HYRCZA-MICHALSKA

The Silesian University of Technology, Akademicka 2A, 44-100 Gliwice, Poland.

J. ROJEK

IPPT PAN, Warszawa, Poland.

O. FRUITOS

CIMNE, Barcelona, Spain.

The cycle of investigations on applying tailor welded blanks (TWB) for sheet forming processes was conducted at Department of Materials Technology of the Silesian University of Technology and as The European Research Project Acronym SIM-TWB. The model of tailor welded blank (TWB model) have been worked out and great number of FEM simulations of stamping process of different geometry drawpieces using TWB were conducted. The paper presents the practical verification of simulation results of stamping process of car body drawpieces: B-pillar and reinforcement of floor of boot, applying TWB for stamping. Stampack – a commercial program for FEM simulation was applied, as well as worked out 5-zones TWB model have been used. The practical verification showed the good agreement of results of simulation and practical experiments of stamping processes of both chosen drawpieces. Hence worked out TWB model is proper and recommend to simulation of TWB forming processes.

Keywords: *tailor blank model, FEM simulation, STAMPACK software, forming of tailored blanks, B-pillar forming*

1. Introduction

The full exploitation of the advantages offered by tailor-blanks is presently limited due to the design and production complications that currently exist. Without adequate simulation to reduce the project time, costly trial-and-error methods are required to enhance the process and make the changes necessary. Because of this the cycle of investigations on applying tailor welded blanks (TWB) for sheet forming processes was providing at Department of Materials Technology of the Silesian University of Technology and as The European Research Project Acronym SIM-TWB. The need for the SIM-TWB project was therefore clear: advances in simulation technology must be made soon in order to take full advantage of concurrent engineering approaches to reduce time and cost, improve quality and safety and enable advances in tailor-welded-blank technology and usage. In this context the use of Finite Element Method (FEM) with specifics devel-

opments for tailor-welded blank technology is a way to achieve the objectives exposed above. The first laboratory and industrial experience with stamping of laser welded blanks, which was elaborate in Department of Materials Technology of the Silesian University of Technology (SUT), allowed to start research on tubes hydroforming processes. The recognition of joined sheet and weld joint mechanical properties and proper their drawability evaluation gave the parameters for lead up finite element method (FEM) simulation of forming and hydroforming of tailor blanks. In papers [1–2] were presented methods of drawability evaluation for both processes using welded blanks and tubes. Part of description of technical developments of FEM simulation using STAMPACK with added software modules for tailor blank is presented in this paper. Different models of tailor blank were tested and simulations were provided by CIMNE (Spain), IPPT-PAN (Poland), QUANTECH A.Z. (Spain), IST (Portugal), SUT (Poland) and industrial partners as a part of SIM-TWB project cooperation work. The most proper model of tailor blank was applied into STAMPACK software and used for FEM simulation of B-pillar pressing.

2. Using STAMPACK and extend model of tailor blank

The mathematical definition of the model to be used for the weld seam included the sheet alignment, welding process and the heat affected zone aspects. The definition of the program structure, input parameters, user interface, weld seam database requirements and user definition of the tailor-blanks has been performed based on the current commercial version of the STAMPACK software and earlier investigation of SIM-TWB European Consortium Partners. This specification assisted the definition of the experimental work required in order to characterize these models properly. Tested models are presented in Figure 1.

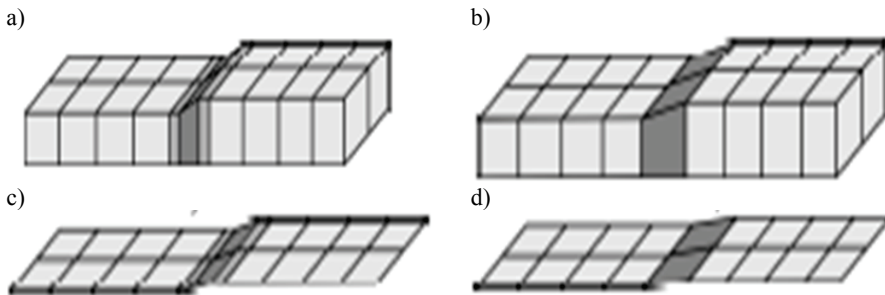


Fig. 1. Finite element models of tailor blank: a), c) 5 zone model, b), d) 3 zone model

FEM studies were carried out to characterise welding, finite element method (FEM) based numerical simulations have been used as an additional aid to study the complex thermal-mechanical-metallurgical interaction during welding. These studies made possible to carry out parameter studies more cheaply than by doing so experimentally.

These studies have been done by IPPT-PAN. Temperature distribution and evolution has been analysed. Residual stresses have been obtained in the weld zone. Development of weld macroscopic constitutive model: the improvement of the model formulated together with CIMNE, IPPT-PAN, IST and SUT to the mathematical formulation of the macroscopic material behaviour of the weld heat affected zone (HAZ) [3–7]. It is a simple model, with few input parameters, relatively accurate but simple for non weld-expert users. Development of complete weld seam behaviour model: the inclusion of the combined geometrical effects such as sheet alignments (different sheet thicknesses welding top-top, bottom-bottom, centre-centre, etc.) that produce bending and torsion forces along the weld with the weld material constitutive effects (virgin material, HAZ, transition zone, etc.) were done. A series of preliminary tests have been carried out and simulations of the experimental work on the blanks will provide initial verification that the models work correctly. The numerical model was completed in the finite element code STAMPAK [8]. Verification tests have been completed to show that the numerical model correctly represents complex deformation of TWBs. Adaptation of user-interface for tailor-blank modelling (TL) – the already existing STAMPAK user interface to enable the user to easily define tailor blanks and the characteristics of the weld-line were done by QUANTECH A. Z. The basic idea is that the user define the different blank zones as well as the weld-seam – this will obviously be more complicated than the current method of just defining the blank material.

3. Blank, material properties and tools definition

An explanation of the initial available information for the simulation of B-Pillar process allowed its final STL representation. The final B-Pillar piece STL representation, shown in Figure 2, was obtained by optical digitalization technology. The inverse engineering process was starting from it to design the tailor welded blank (TWB) deep drawing process. Moreover the advantages, disadvantages and limitations of this kind of technology are shown. The experimental and simulated results comparison is done too. The forming limit curve (FLC) has been used as failure criterion. The STL definition from optical digitalization of final piece was proposed by Silesian University. In Figure 2 a general view of final piece described by 195079 triangular facets, is shown.

Through STL definition, a complete simulation of B-Pillar process has been done. This inverse engineering process was done thanks to SIM-TWB project specific software (STAMPAK).

The main advantages of optical digitalization technology are:

- The simplicity. In one operation, without manual manipulation, the geometry of final piece is obtained.
- Moreover, one file and one layer content all the blank definition. The output format of optical digitalization is totally compatible with software used in simulation. The lecture was OK. It had zero warning or error messages.

- The surface description quality is high. The density of triangular facets is function of curvature. The stretching effect is used to reduce the total number of facets: If there is one curvature direction only, high relation aspect is used.

- The surfaces normal sense is uniform all over the piece.

However, optical piece digitalization also has disadvantages:

- It is not possible to know the exact geometry of tools (die, punch, blankholder) because the final piece is affected by springback effect. In B-pillar case there are some walls that have negative slopes.

- If the process has two steps, is not possible to know the tools geometry of the first operation.

- If drawbeads were used during the deep drawing its profile is acknowledged. Only in blocking drawbeads case, the profile of them is reproduced approximately in the final shape.

- The optical digitalization reproduces one face of the final piece, only. The steps in punch, die and blankholder are not visible in function of the face used for digitalization task.

- It's impossible to know where the blank initial positioning is.

- The STL mesh definition has not the suitable position to define the optimal forming direction.



Fig. 2. Geometrical description of final piece (195 079 triangular facets)

The main limitation in simulation of the process is that the geometries of different tools (blankholder, punch and die) were not defined. To simulate the process an approximation from the available geometric information (STL mesh) was done. However, this approximation is not possible to do without errors. The exterior limit of accordance radius of die is used to define the inner border of blankholder.

Other important parameters must be defined by the user:

- blankholder force,
- blankholder velocity (in clamping),
- punch velocity,
- frictional coefficients,
- damping coefficients.

The suitable information to simulate the process is the blank boundary definition (in IGES format for example) or a complete dimensional definition of the initial blank. In this case the information available is shown in Figure 3.

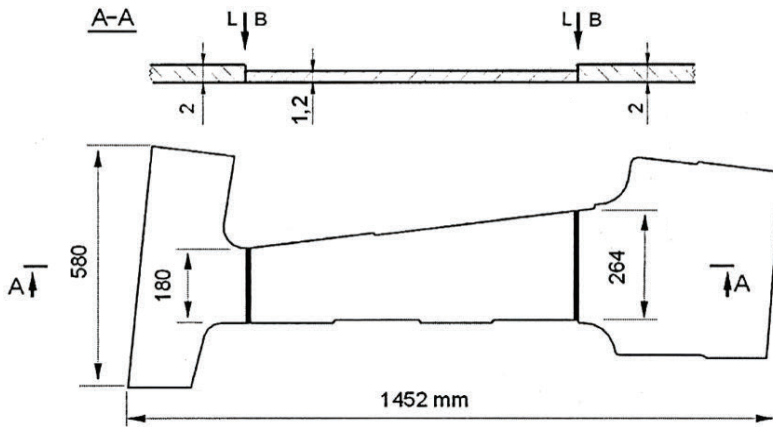


Fig. 3. Partial description of blank dimensions

However, through STAMPAK pre-processor, a good approximation of the blank format in its initial configuration was done. The methodology to create the initial blank format is:

- Take the Figure 5 as background of STAMPAK pre-processor.
- Draw the figure contour with lines (straight or NURBS), and also the radius of the figure using Stampack edit geometry facilities.
- Define the weld lines and heat affected zones (HAZ).
- Scale the model to real dimensions.

A good approximation of the localization of weld lines have been done by the method explained above. Once the model geometry is succeeded the mesh could be done. This method is a good approximation of the real blank shape. In the Figure 4 the measures of the STAMPAK geometry is shown.

To define the HAZ (heat affected zones) and weld lines (WL) dimensions has adopted a strategy similar to that is explained in [1–7]. In B-Pillar process an additional zone must be defined in order to improve the CPU times. That's because the element sizes of the HAZ and WL zones are lower that the element size all over the sheet. Small element size imposes limitation on the time step length in the explicit

integration scheme. This leads to large number of time steps required for the solution. A commonly used method to increase efficiency of the solution consists in scaling the mass (density) of small elements [9] to increase the critical time step. Mass scaling should be introduced carefully in order not to increase inertial effects excessively. Based on our experience the density has been scaled 20 times in transition zone and 40 times in HAZ and WL. Hence, the zones dimensions are:

- 1 mm of width in HAZ,
- 0.5 mm of width in WL,
- 6 mm of width in transition.

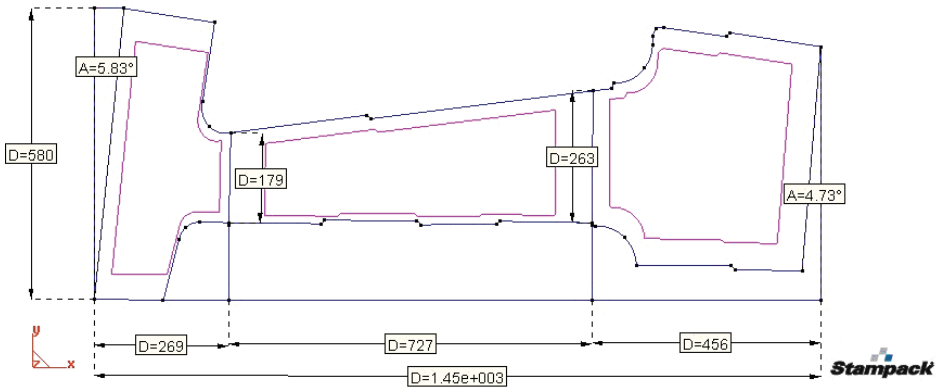


Fig. 4. Initial blank geometry in STAMPACK

The assignation of the blank materials is more complex than in non TWB process, and in this case the difficulty is higher because the blank have 8 different zones, where 7 different materials have to be informed in the specific interface. The different zones and its parameters for steel simulation are explained in the Table 1. In Figure 5 a graphical interface menu of zones definition is shown.

Table 1. Steels mechanical characteristics (partial) by zones

Zone Name	Material	Thickness (mm)	Density (kg/m ³)	Mec. Properties
cubeta	DX56D	2.0	7800	Std.
trans2mm	DX56D	2.0	156000	Std.
haz2mm	DX56D	2.0	312000	10% increased
wl	DX54D	1.6	312000	20% increased
haz12mm	DX54D	1.2	312000	10% increased
trans12mm	DX54D	1.2	156000	Std.
central	DX54D	1.2	7800	Std.
rail	DX56D	2.0	7800	Std.

The tools definition has been done from the final piece. The tools geometries were done by inverse engineering process. In this case both the punch, as the blankholder as the die had to be created. Every simulation parameters were assigned into mesh, be-

cause the geometry of the tools did not exist. To create the punch, a cut of STL mesh was done. The interior part of the cut was the punch. It has 184481 triangular contact faces. In Figure 6 the punch is shown. The blankholder was created from the sum of two zones: the interior zone (near to accordance die ratio) and the exterior zone.

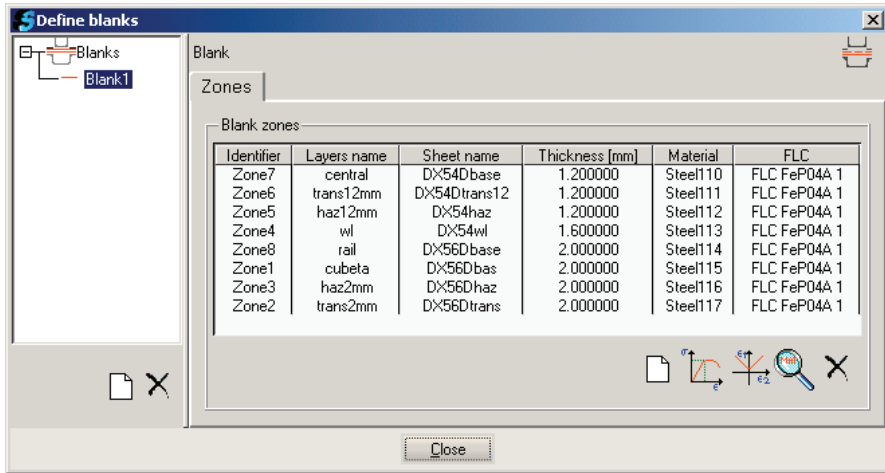


Fig. 5. Interface zones definition

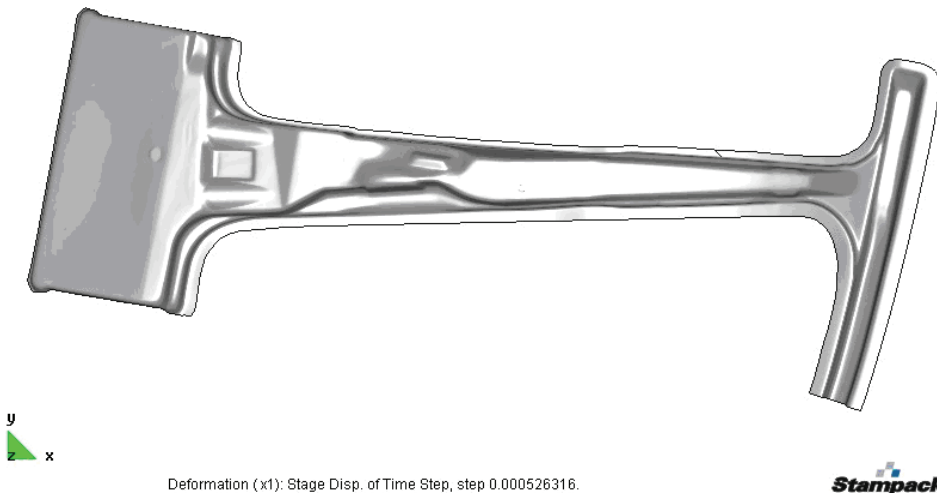


Fig. 6. Punch definition

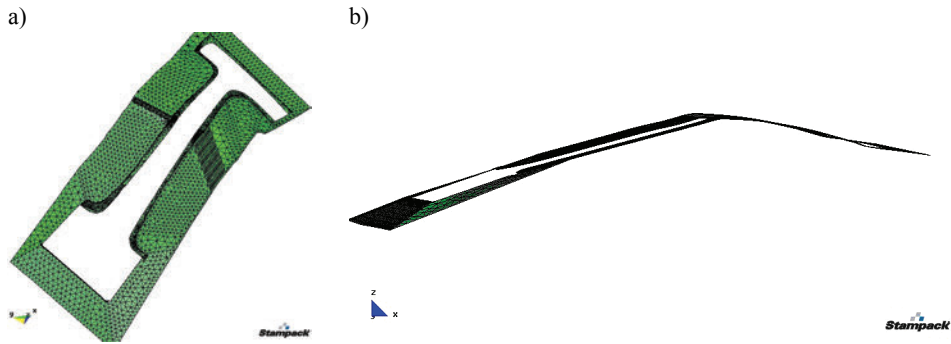


Fig. 7. a) Complete blankholder – interior and exterior, b) blankholder curvature

The blankholder has 12831 triangular contact faces in total. The interior zone was obtained by a cut of STL mesh. The exterior zone was done from STL file. This file was imported in STAMPAK environment, then was exported in *.dxf files, and then opened in STAMPAK environment once again. By this way, the final format of the blank could be worked like geometry (not in mesh mode).



Fig. 8. a) Die smoothed mesh, b) general blank's mesh, c) mesh in weld area

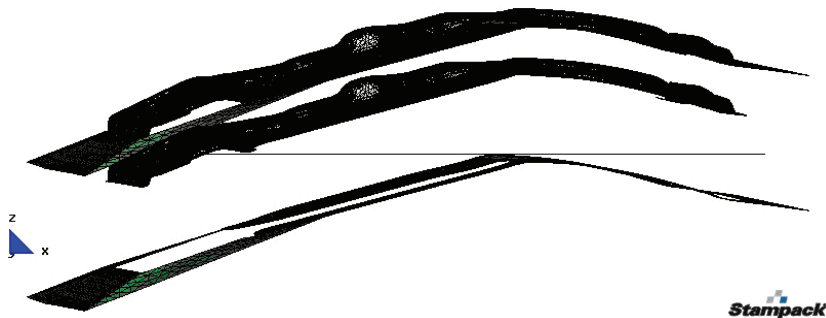


Fig. 9. Initial tools and blank positioning

Once the final blank format was opened in STAMPAK as geometry, the copy of exterior points were done to get the interior line of exterior zone. The exterior part had

to be the same curvature that the rest of the blankholder. The complete blankholder and its curvature are shown in Figures 7 respectively. The die is the sum of final blank format (sent in STL file) added to the exterior zone of the blankholder. The die has 198232 triangular contact faces. In Figure 8 the die is shown.

The mesh criterion was obtaining a regular element size in the different zones. The element size searched was 7.5 all over the blank, except in the HAZ and WL that was 0.5 in width and 2 mm on length (Figure 8c). In the transition zones the element size increases from 2 to 7.5 mm. The blank mesh total elements are 19824 BST (Basic Shell Triangle) elements (see Figure 8b).

The relative position of blank and die is necessary to simulate correctly the process. In this case, we supposed that the tools were on correctly position (not the most optimized) and it is also supposed that the blank was horizontal. In this case, the punch stroke is optimized, and the initial positioning of tools and blank is shown in Figure 9.

4. Simulation results

For prepared model of blank, dies and blankholder for forming B-pillar, the simulation results for steel (DX54D and DX56D) are shown. There is also described one geometric limitation in simulation and its cause is explained. The strokes of the model are:

- blankholder stroke: approximately 275 mm,
- punch stroke: approximately 105 mm,
- the punch is not activated at the beginning.

The main contact parameters of the model are:

- cut off: 1e-5,
- penalty: 0.1,
- frequency: 1000.

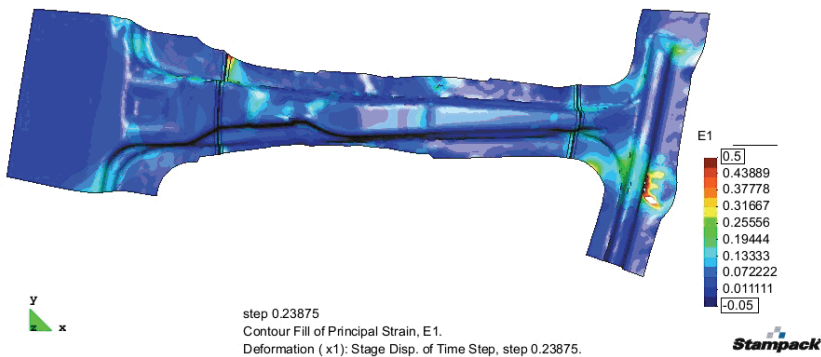


Fig. 10. Simulated distribution of main strain (ϵ_1) at the end of the process of stamping B-pillar

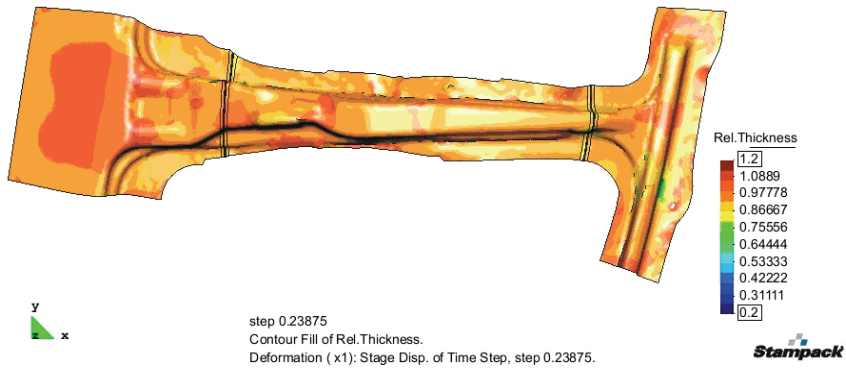


Fig. 11. Simulated relative thickness at the end of the process of stamping B-pillar

Other parameters are damping in blankholder stage: 50% in 0.01 seconds and damping in forming stage: 50% in 0.1 seconds. The results obtained in tested model are shown in Figures 10 and 11. In some zones the results are not quite good. That's because the tools were not fine defined because the punch and the die are equal (extracted from STL file), and the final piece had springback with negative walls. That's the reason of the blank's penetrations in the tools.

5. Experimental results comparison

The experimental results comparison has been done with model formed in steel material and the FLC curves made by the Silesian University of Technology. In experimental results four zones have been studied. These zones are shown in the Figure 12.

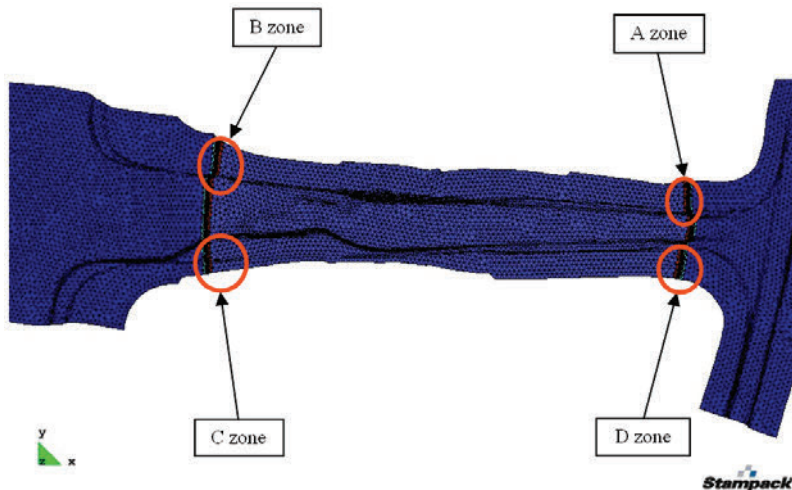


Fig. 12. Experimental study zones in B-Pillar

There were analyzed the experimental FLC for joined sheet blanks and results of stamping B-pillar in four zones. Exemplary comparison of experiment and simulation FEM results is shown for zone B (Figures 13 and 14) and zone C (Figures 13 and 15).

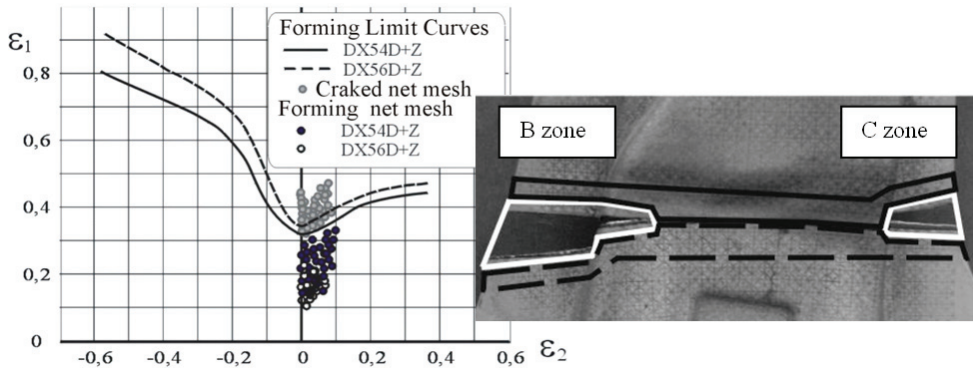


Fig. 13. Experimental results in B zone of B-pillar

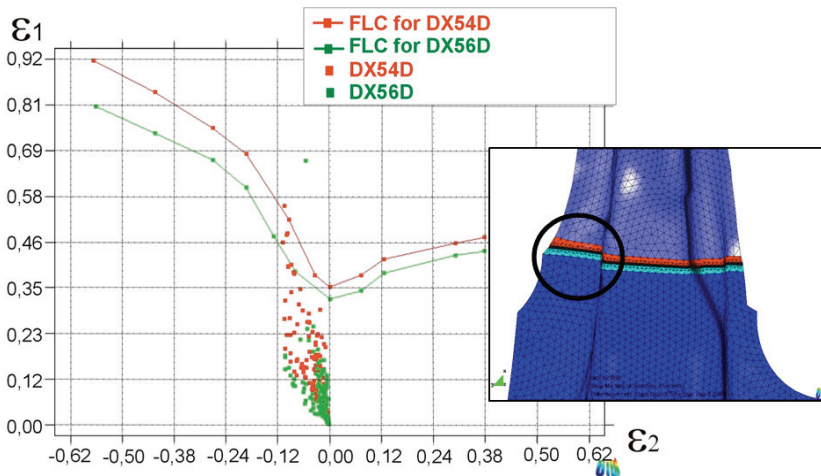


Fig. 14. Simulation results in B zone of B-pillar

Defined method of TWB drawability evaluation based on laboratory tests with seam weld behaviour analysis in according to forming limit curves of joined sheets, laboratory tests and hardness measurements on cross section of weld area have helped to define 5-zones model of TWB and applied this model to accurate simulation. Laboratory tests for TWBs joined of different materials and using different welding techniques, allowed to choose proper joining techniques for steel materials. Possibility of experimental work on sheet blanks and Tailor Welded

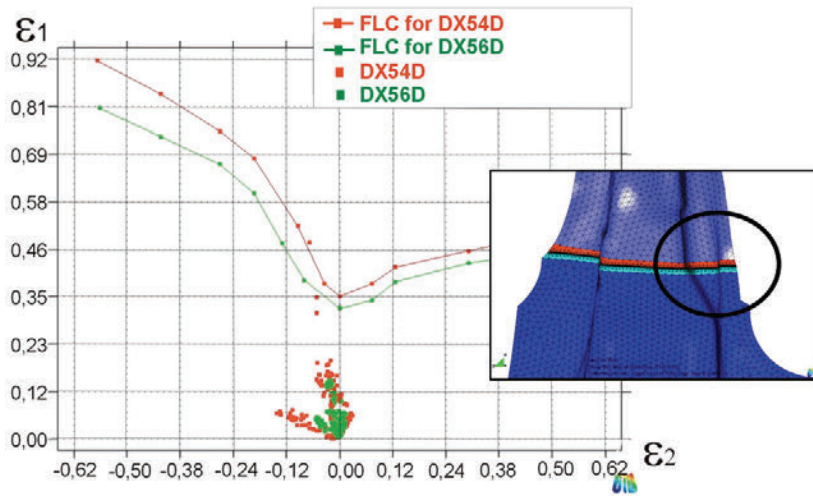
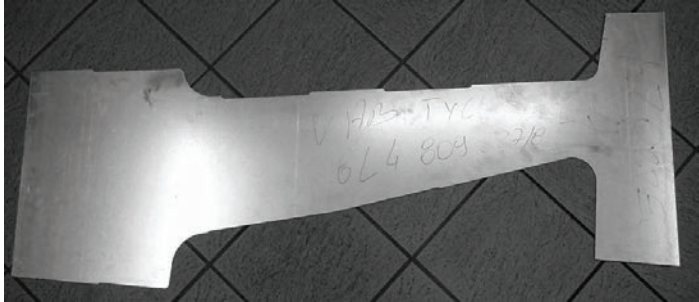
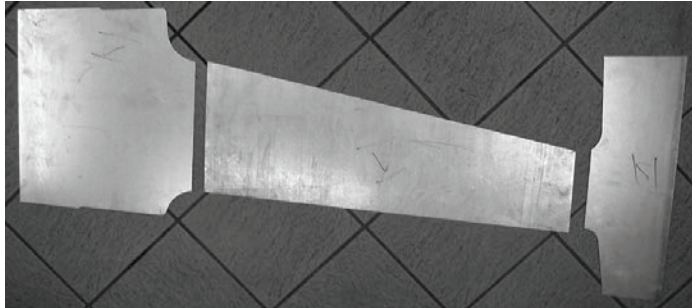


Fig. 15. Simulation results in C zone of B-pillar

Table 2. Blank type for B-pillar comparison of weight

Blank type for B-pillar	Weight
Typical blank (2 mm thick) 	11.50 kg
TWB (2 mm + 1.2 mm + 2 mm thicknesses) 	9.61 kg
Weight reduction result (16%)	1.89 kg

Blanks (TWB) has been defined. Steels TWBs have prepared by IST and Polish Welding Centre of Excellence (PWCoE). After materials for testing had been defined, sheet alignment of TWBs has set. At Magna Cosma FORMPOL Sp. z o.o. stamping plant in Tychy was realized industrial application of TWBs base on earlier industrial experience on TWBs. Industrial tests have been provided to manufacture drawpiece of B-pillar from accurate designed TWBs. The major aim of designed TWBs was to reduce thickness of sheet (in the end to reduce the weight of blank – see exemplary figure) and execute it in proper area of the blank. Tests of welding techniques and study on proper laser welding parameters made by IST and PWCoE, allowed to execute good welds, it means welds of good drawability properties and accurate for stamping processes. Industrial test of stamping B-pillar from TWBs obtain 16% weight reduction for designed blank (see table 2). It corresponds with planned vehicle weight reduction.

The data consists of basic properties, drawability properties and FLCs coordinate for testing and simulated materials PS has delivered. All partners could use it. PS has prepared numerical model of B-pillar geometry and CIMNE, based on it, has done simulation of stamping using Stampack software for this drawpiece.

6. Conclusions

The conclusions extracted in this industrial TWB benchmark (B-Pillar) are:

- Through an inverse engineering an approximation of tools can be defined.
- The contact forces are lower than 4000 KN, which is the maximum capacity of the press machine.
- The STL transfer information from optical digitalization was quite well and acceptable. The STL mesh file had not errors.
- With STAMPACK geometry edition capacities, from a figure of initial blank the geometry of the blank can be created.
- The planar strain distribution, from simulation, approximates the experimental results. Some variations in blankholder parameters, tools definition (punch and die) could be done to optimize the process.
- In weld seam (weld line and HAZ) the behaviour of $\varepsilon_1/\varepsilon_2$ relation is near to Poisson coefficient in most cases.
- The CPU times have been optimized with density scale and regular element size.

References

- [1] Hycza-Michalska M., Rojek J.: *Laserowe spawanie wsadów do tłoczenia. Wybrane problemy wytwarzania i symulacja numeryczna*, Mechanik, Vol. 4, 2009, pp. 274–281.
- [2] Rojek J., Hycza-Michalska M., Bokota A., Piekarska W.: *Determination of mechanical properties of the weld zone of tailor-welded blanks*, Computer Methods in Materials Science, Vol. 9, No. 1, 2009, pp. 333–336.

- [3] Pielą A., Hyrcza M., Lisok J.: *Model spoiny laserowej we wsadach do tłoczenia typu tailored blanks*, Przegląd Mechaniczny, Vol. 4, 2001, pp. 19–22.
- [4] Pielą A., Rojek J.: *Validation of results of numerical simulation of deep drawing of tailor welded blanks*, Archives of Metallurgy, Vol. 48, No. 1, 2003, pp. 37–51.
- [5] Rojek J., Jovicevic J., Oñate E.: *Industrial applications of sheet stamping simulation using new finite element models*, Journal of Materials Processing Technology, Vol. 60, No. 1–4, 1996, pp. 243–247.
- [6] Rojek J., Oñate E., Postek E.: *Application of explicit FE codes to simulation of sheet and bulk metal forming processes*, Journal of Materials Processing Technology, Vol. 80–81, 1998, pp. 620–627.
- [7] Rojek J., Oñate E.: *Sheet springback analysis using a simple shell triangle with translational degrees of freedom only*, International Journal of Forming Processes, Vol. 1, No. 3, 1998, pp. 275–296.
- [8] STAMPAK 7.01, Data input manual (draft version), Ed. Quantech ATZ S.A., Barcelona, Spain, 2007.
- [9] Olovsson, L., Simonsson, K., Unosson, M.: *Selective mass scaling for explicit finite element analyses*, International Journal for Numerical Methods in Engineering, Vol. 63, No. 10, 2005, pp. 1436–1445.

Praktyczna weryfikacja rezultatów symulacji numerycznej tłoczenia elementów karoserii samochodowej z wsadów spawanych laserem

W ramach cyklu badań nad zastosowaniem wsadów spawanych laserowo, prowadzonych w Katedrze Technologii Materiałów Politechniki Śląskiej oraz w ramach projektu Europejskiego SIM-TWB opracowano model WSL i przeprowadzono szereg symulacji numerycznych MES procesu tłoczenia zróżnicowanych konstrukcyjnie elementów z blach spawanych laserem. W artykule przedstawiono praktyczną weryfikację wyników symulacji tłoczenia wybranych wytłoczek karoseryjnych, a mianowicie: słupka B oraz wzmocnienia podłogi bagażnika, tłoczonych z wsadów spawanych laserowo. Do symulacji zastosowano komercyjny program STAMPAK oraz opracowany model 5-warstwowy wsadu spawanego. Weryfikacja praktyczna wykazała dobrą zgodność wyników symulacji i eksperymentów praktycznych tłoczenia obu wybranych wytłoczek, a co za tym idzie opracowanego modelu wsadu spawanego.



Application of longitudinal cold rolling method in mass production of stepped shafts used in combustion engines

M. KOWALIK

Technical University of Radom, ul. Krasickiego 54, 26-600 Radom, Poland.

This paper presents little-known, innovative technology of cold rolling of stepped shafts. The method makes it possible to form and finish-up machine parts in the rolling process, which is associated with strengthening of material due to cold work. The author presents the results of investigations on the influence of the state of stress during cold plastic work on material's structure and its strength properties. The tests were carried out on shafts formed by longitudinal cold rolling (LCR), made of alloy steel, quenched and tempered before rolling to the hardness 34HRC. The influence of deformation degree on structural changes and increase of material strength is shown. Examples are given illustrating application of CLR technology in producing machine parts of shaft type designed for combustion engines.

Keywords: cold plastic deformation, longitudinal rolling of stepped shafts, strength properties

1. Description of process of longitudinal cold rolling of stepped shafts

The method of longitudinal rolling is one of the modern methods of precise cold plastic working of shafts [1]. It consists in forming the shaft's steps by means of appropriately shaped rolls. The rolls have a cylindrical part, whose task is to transmit the loads onto support sleeves, and the working part whose contour reflects the shape of transverse cross-section of the formed shaft step. For example, to form shaft steps of circular cross-section, one uses the rolls whose working part consists of a toroidal surface and two conical surfaces.

A general scheme of forming of stepped shafts by longitudinal rolling method is shown in Figure 1. The shaft (1), fixed in the way enabling its elongation in the forming process, is placed between two forming rolls (2), each of whom is supported by two support sleeves (3). The forming rolls (2) have a cylindrical part, whose task is to transmit the loads onto support sleeves (3). The support sleeves (3) can revolve around their axes, in this way allowing the forming rolls (2) to rotate during the process of rolling. Plastic forming of the shaft consists in making several – or a dozen or so – working passages, in which one can distinguish the following phases.

The squeezing phase is characterized by transverse dislocation of forming rolls, which under the influence of external forces shift towards the axis of the shaft. In the result of pressure exerted on the shaft, the shape of working part of the rolls is repro-

duced on the shaft, and this is accompanied by small elongation of the shaft. During the first working passage, the squeezing phase continues until the required diameter of the shaft is reached.

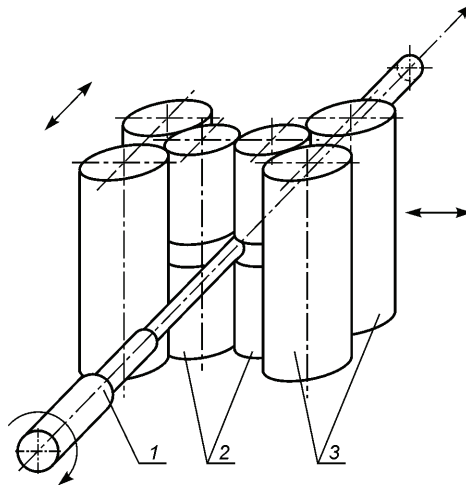


Fig. 1. Scheme of forming shafts by longitudinal rolling method

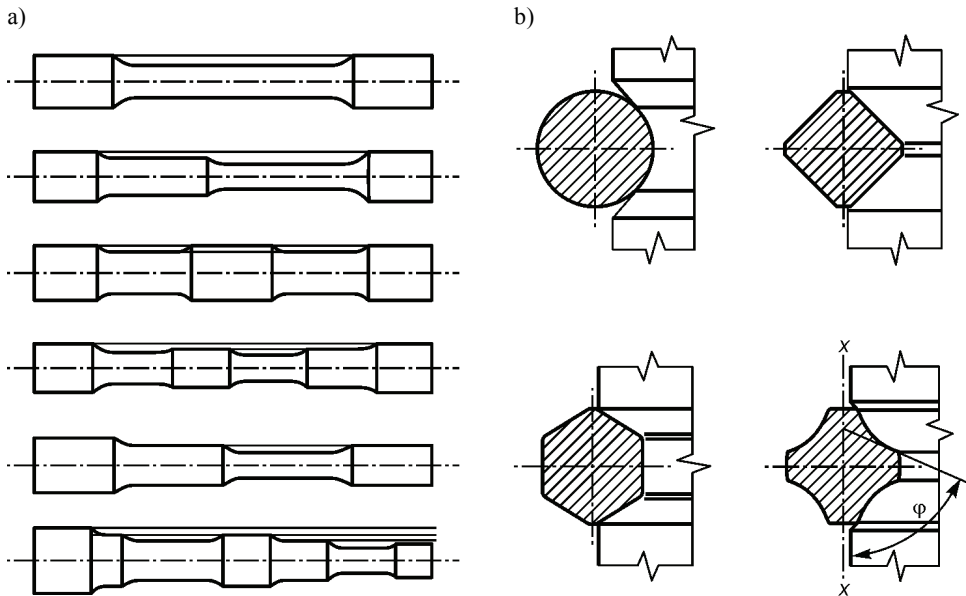


Fig. 2. Examples of stepped shafts that can be made by longitudinal rolling method:
a) examples of step arrangements; b) achievable cross-sections of steps

The rolling phase is characterized by the movement of forming rolls along the shaft axis, during which forming of the shaft in its transverse cross-section takes place, and (simultaneously) there appears elongation caused by the decrease in dimensions of the shaft's transverse cross-section. In this phase, the forming rolls roll on the generating line of the profiled shaft. To obtain the required transverse cross-section of the shaft within all the distance of forming, one maintains constant pressure of the mechanism with forming rolls against the rigid stop. Consequently, the forming rolls retract off the formed shaft and return to the initial position, while the shaft rotates by 90° (for circular cross-section). The complete forming of the shaft and reaching the required length needs from several to over ten working passages. The number of passages depends on the required accuracy, applied parameters of working, and initial geometry of the shaft. Multi-step shafts are produced by forming several steps along the length of the shaft; in this case, it is necessary to apply at least as many forming roll couples as the number of steps of different cross-sections. Possibilities of forming shafts of different cross-sections are presented in Figure 2.

Among undeniable advantages of longitudinal rolling method one can mention: large possibilities of forming shafts of variable contours and dimensions of transverse cross-section in one working operation, the possibility of making shafts from high-strength materials, very high durability of tools resulting from the character of working, and easiness of introducing automatic control in the forming process.

2. Influence of stress state during forming on strength properties of shafts

Considering the system of forces acting on the shaft in the forming process, one can distinguish two kinds of longitudinal rolling: in the pulling system, with the use of tensile force (Figure 3a), and in the pushing system, with the use of compression force (Figure 3b). In both cases, the phases of the rolling cycle are similar, but the states of stress in the formed shaft are different.

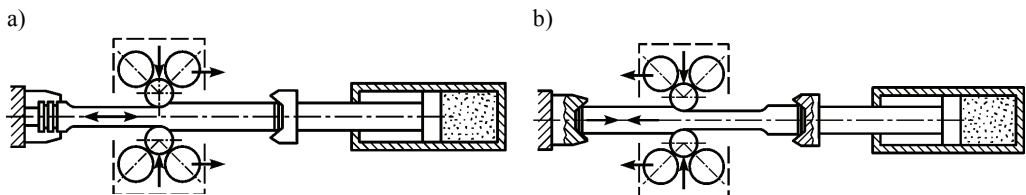


Fig. 3. Variants of longitudinal rolling: a) in pulling system; b) in pushing system

In the pulling system, there appears an axial tensional force in the shaped step of the shaft, while elongation of the material is consistent with the direction of rolling. This variant of the process is designed for slim shafts of small diameters. When rolling is performed in the pushing system, the direction of rolling is opposite to shaft's elongation. The forming rolls strongly press the shaft against the spindle of the rolling machine, which makes it easier to fix the shaft. However, the shaft must not be too

long and have too low diameter because of danger of buckling caused by the axial compression force during machining.

In the process of forming in the pulling system, the material is subjected to biaxial compression appearing in the deformation zone, accompanied by uniaxial tension (Figure 4a). In the case of deformation in the pushing system, a tree-axial compression appears in the deformation zone (Figure 4b). In order to determine values of the forming forces, we developed a numerical model of longitudinal rolling. For numerical analysis of the process, we used the software package MSC.Marc+MENTAT 2005 known as an effective tool for spatial analysis of plastic working processes [7]. The FEM simulation was carried out for a real-size model of the shaft and the tools, taking into account actual kinematics of the process. The working rolls with tangent contour (Figure 5a) were modelled as undeformable ones, which made it possible to take into account in the model only the contour of the outer surface (Figure 5b) [2–3].

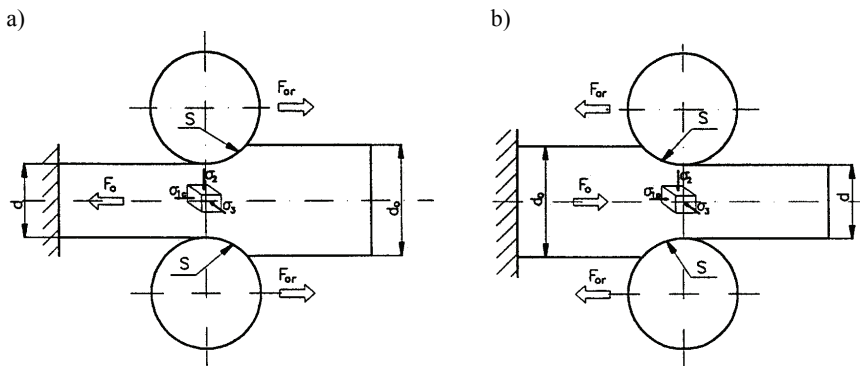


Fig. 4. Models of load on the shaft and state of stress in the process of longitudinal rolling: a) in pulling system, b) in pushing system

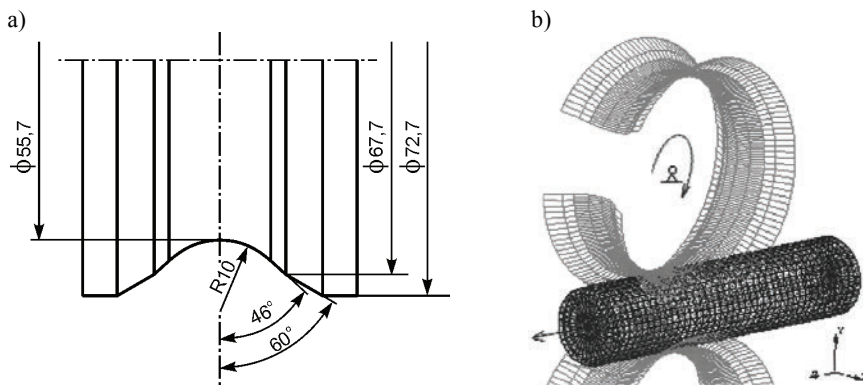


Fig. 5. Characteristic quantities assumed in numerical simulation of longitudinal rolling process: a) contour of working roll, b) model of contour of roll's surface

The shaft subjected to deformation had a 24 mm diameter, which was reduced to 20 mm by rolling in the pulling and pushing systems. The imposed boundary condition allowed the nodes lying on the shaft's axis to move only in axial direction. The assumed elastoplastic model of the material had the following parameters: Young's modulus 2.1×10^5 MPa, Poisson's ratio 0.3, yield point 970 MPa. To describe contact phenomena between the shaft and the rolls, we used the Coulomb's law with a factor of 0.1. Simulation calculations were performed for the first and the second rolling passage in whom appear the greatest deformations (rotation by 90° applied between passages). The results of simulation of roll pressure force during the cold work phase and the first rolling passage in the pulling and pushing system are presented in Figure 6a.

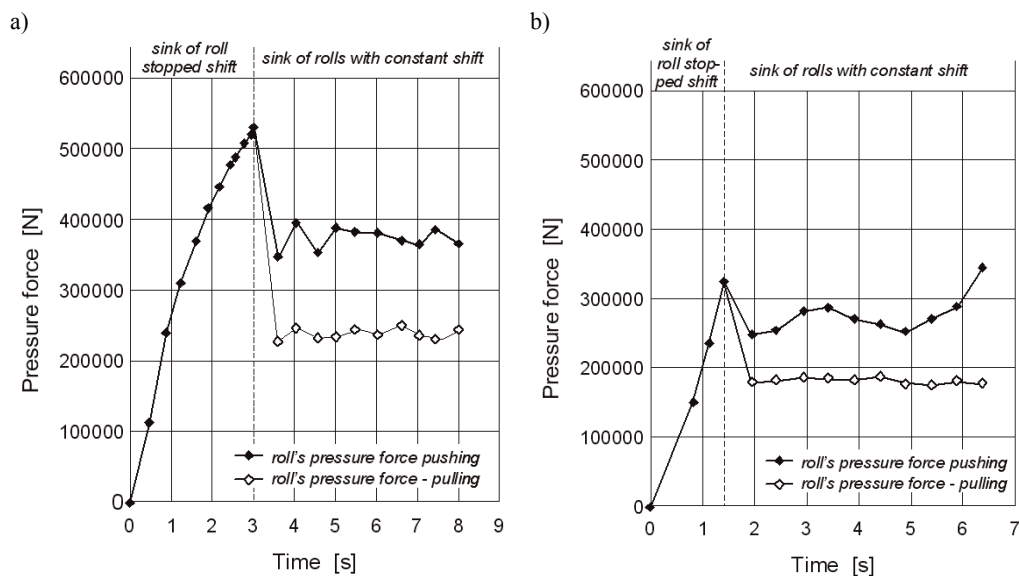


Fig. 6. Pressure force of the rolls in cold work and rolling phases: a) first forming passage; b) second passage – after rotating the shaft by 90°

The course of roll pressure force in the cold work phase is the same for both rolling methods. At the moment when the rolling phase starts, the pressure force drops to approx. a half of its value, because the area of contact between the roll and the rolled shaft decreases. In the pulling method, the sense of stresses is consistent with the direction of deformation. In the second rolling passage, after rotation of shaft by 90° , the pressure force in the pulling method is smaller than that in the first passage, despite the fact that the contact surface does not change (Figure 6).

Figure 7 shows results of simulation of the longitudinal force for the first and the second rolling passage. The value of pulling force is lower in both first and second (after rotation of shaft by 90°) rolling passage, which is due to consistent directions of stress and deformation.

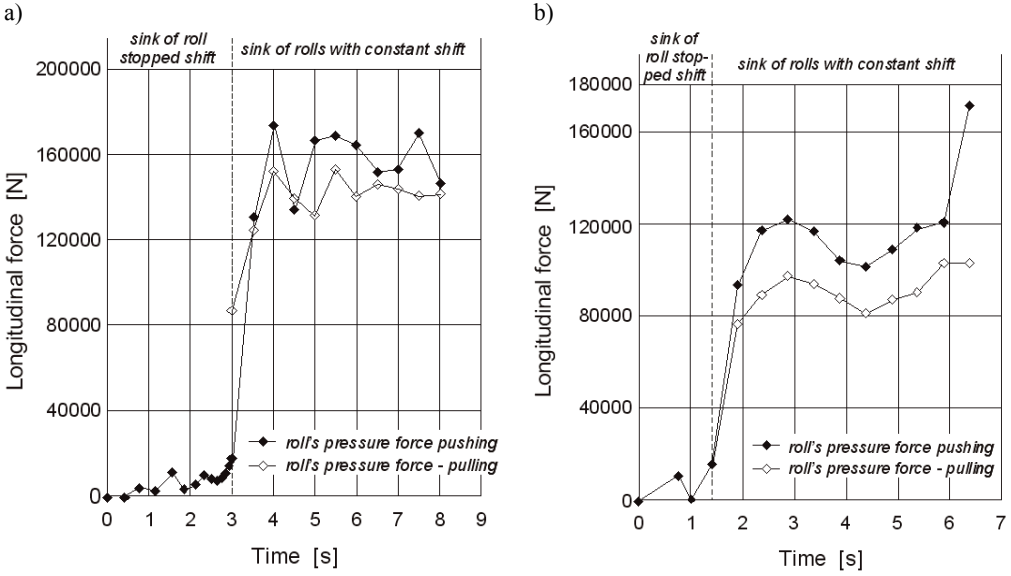


Fig. 7. Longitudinal force of rolling; a) first rolling passage;
b) second passage – after rotation of shaft by 90°

To evaluate the strains, we take into account the changes of linear dimensions and areas in appropriate cross-sections. The dimensions and cross-section areas of the strained shaft are related to those existing in the shaft without strain; in this way, we define the relative strain ε_1 , which is commonly recognized as the measure of strain (Figure 8)

$$\varepsilon_1 = \frac{l - l_0}{l_0}. \quad (1)$$

After transformation and introducing the condition of constant volume we obtain:

$$\varepsilon_1 = \frac{d^2 - d_0^2}{d_0^2}, \quad (2)$$

where:

l_0 – initial length for rolling,

l – length of rolling,

d_0 – initial diameter for rolling,

d – diameter after rolling.

Metallographic examinations and strength tests were carried out on shafts of initial diameters of 11, 15, 19, 21 and 23 mm, which were rolled to obtain a diameter of 10 mm.

Consequently, the resulting strains were: $\varepsilon_1 = 0.21$; 1.25; 2.61; 3.41; 4.29. The lengths of rolling were selected so that to obtain a shaft of structure satisfying the requirements of strength examinations in the test of uniaxial static tension [4]. The examinations were carried out on shafts made of alloy, chrome-nickel-molybdenum steel type 40HMNA, quenched and tempered before forming to the hardness of 34HRC. This kind of steel has world-wide application in construction of high-performance machine elements, especially shafts, and has its equivalents available in many countries.

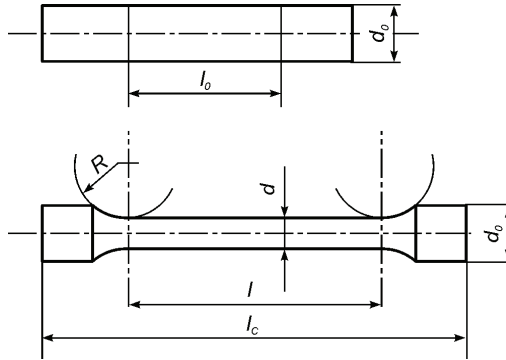


Fig. 8. Scheme of shaft before and after forming: l_0 – initial length, d_0 – initial diameter, R – working radius of roll, d – formed diameter, l – length after forming

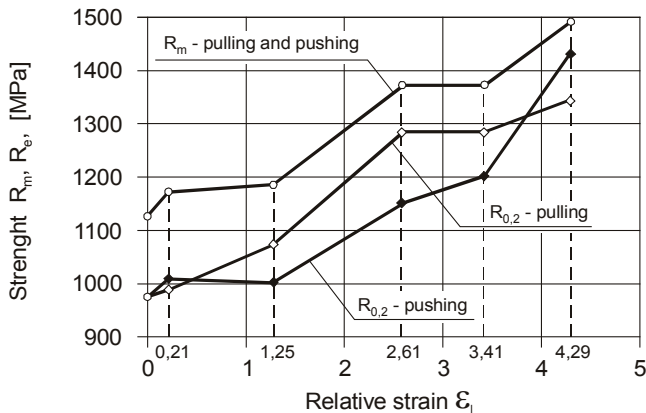


Fig. 9. Dependence of conventional yield point $R_{0,2}$ and tensile strength R_m on shaft's relative strain ε_1 for pulling and pushing methods of rolling

The research revealed monotonous increase of the value of conventional yield point $R_{0,2}$ with increasing relative strain (Figure 9), with a clear tendency of saturation after exceeding the strain value of $\varepsilon_1 = 2.61$. The shafts formed by pulling method exhibited a higher yield point. The value of tensile strength R_m increased with growing strain, and was the same for shafts formed by pulling and pushing methods.

3. Influence of strain on material structure in process of longitudinal rolling

The process of longitudinal rolling causes uniform changes of material structure in the whole cross-section of the formed shaft, irrespective of method used to produce the strain [4]. The shafts were made of alloy steel 40HMNA quenched and tempered before forming to the hardness of 34HRC. After this treatment, the steel had a sorbitic structure with grains in the form of needles (Figure 10a) [5], which were oriented in different directions. In the result of strain, the material elongated, and the grains took orientation consistent with strain, i.e. parallel to the shaft axis. For the strain value $\varepsilon_1 = 1.25$ one could already see certain directionality in grain orientation (Figure 10b), and when strain increased above $\varepsilon_1 = 2.61$ (Figure 10c and 10d) the grains became clearly oriented along the direction of rolling, creating the characteristic texture of internal work-hardening.

The polished metallographic specimens were taken from the shaft's axial cross-section, parallel to the direction of rolling. The image of metallographic structure did not change within the whole longitudinal cross-section of the rolled shaft's step.

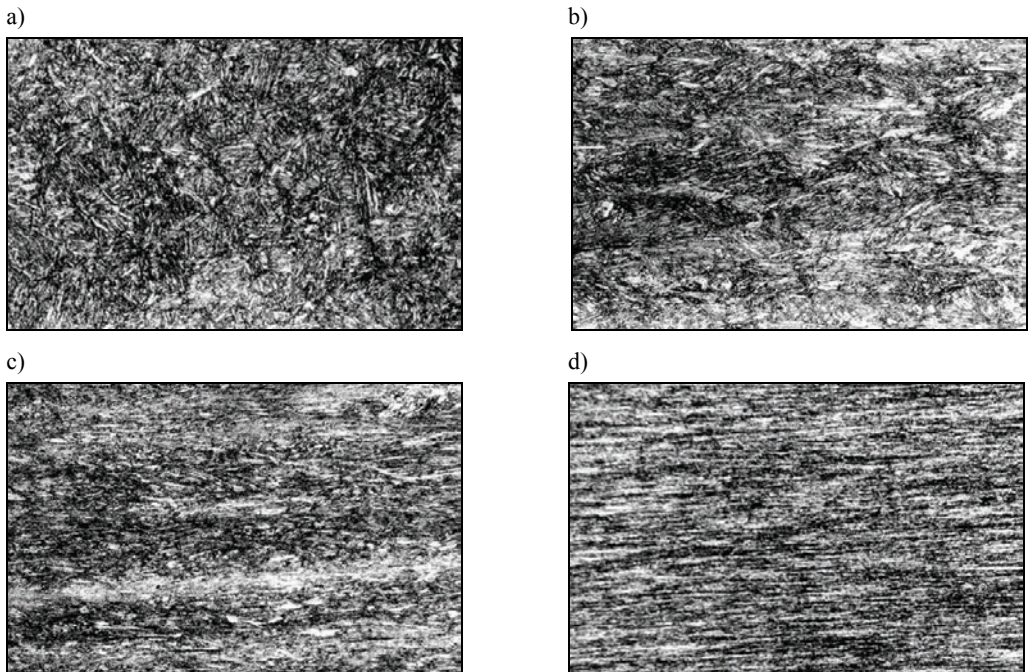


Fig. 10. Structure of shafts made with different strain ε_1 ; metallographic specimens oriented parallel to direction of strain: a) strain $\varepsilon_1 = 0$, b) strain $\varepsilon_1 = 1.25$, c) strain $\varepsilon_1 = 2.61$, d) strain $\varepsilon_1 = 4.29$, magnification $400\times$

In the shafts rolled by pulling and pushing methods, in which the relative strain reached the value of $\varepsilon_1 = 4.29$, the grains were evidently compressed and elongated, and took orientation parallel to the direction of strain.

4. Examples of application of longitudinal rolling method in production of stepped shafts combustion engines

Application of longitudinal cold rolling method in production of shafts increases their static strength by approx. 20% and fatigue life by 50% [4], at the same time reducing consumption of the shaft's material, on average by approx. 30%, depending on dimensions of the rolled shafts. The method of longitudinal cold rolling, applied in the conditions of mass production in automotive industry, is definitively competitive to conventional machining technology because of economical use of the material and easy automatization of the production process (due to the absence of swarf). Plastic forming of shafts causes that their mechanical properties ameliorate, and the costs resulting from the wear of tools are significantly reduced. For example, one pair of rolls can be used to produce 10 000 to 15 000 shafts.

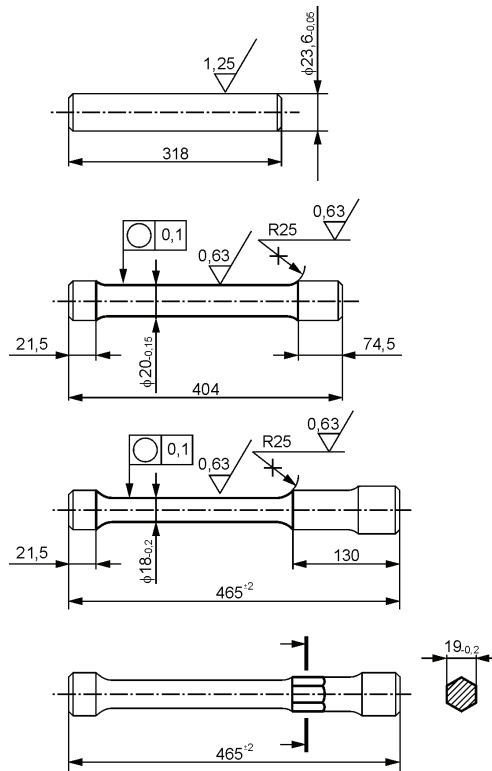


Fig. 11. Stages of rolling process of stay bolt

Figure 11 presents the changes of shapes and dimensions of the material in consecutive stages of forming a stay bolt of an internal-combustion engine. The bolt's material is a piece of alloy steel 40HNMA quenched and tempered to the hardness of 34–36HRC, of initial diameter 23.6 mm and length 318 mm. Before the start of cold rolling, the edges of shaft's faces were cut to facilitate fixing the shaft in the rolling mill of pushing type. The shaft is formed by three pairs of rolls that interchange automatically. In the first stage, when the shaft is formed to a 20 mm diameter, its elongation equals 82 mm. In the second stage, when the shaft's step of 18 mm diameter is formed, the elongation equals 61 mm. Finally, a hexagonal segment of 19 mm size (distance between sides) is rolled on the 20 mm step of the shaft made in the first stage.

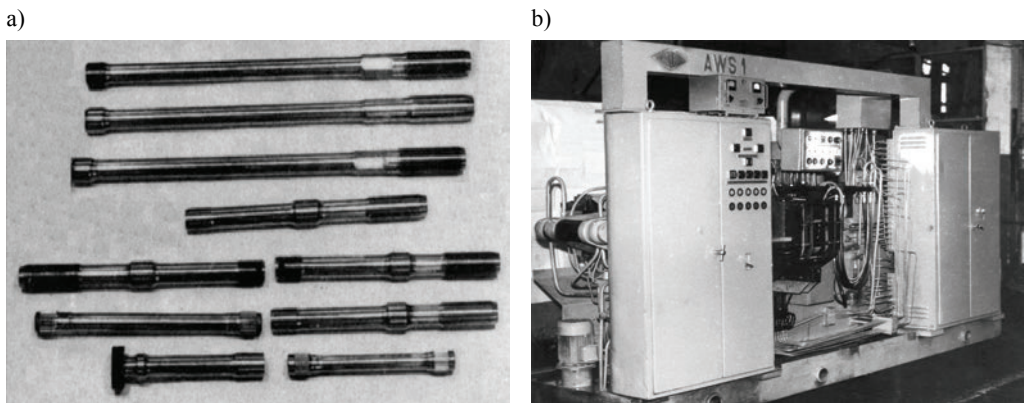


Fig. 12. Rolling mill, and shafts made by longitudinal rolling method: a) stepped shafts formed by cold longitudinal rolling method, b) automated rolling mill AWS-1

The number of rolling passages necessary to obtain the required dimensions ranges from 4 to 6 in each rolling process. When rolling circular parts of the shaft, rotation of roller mill spindle by 90° takes place after each passage of forming rolls, while the hexagonal part is rolled with 60° rotation steps. In the result of rolling, the material of shaft elongates from 318 mm to 465 mm, i.e. by 147 mm, which gives an approx. 30% saving of the material. The total time of forming of the stay bolt shown in Figure 11 equals 2.5 min, and is four times shorter than that required in conventional machining. Figure 12a presents some parts of combustion engines produced on mass scale on the rolling mill AWS-1 (Figure 12b). In the shafts made by longitudinal rolling method, the forming process is always associated with a reduction of the initial diameter of semi-finished product. In the case when the required difference in shaft's diameters is small, all surfaces of the shaft, are subjected to rolling. Longitudinal rolling in this case is the finishing technological operation. It is also possible to form the shaft by rolling applied alternatively with machining. In such a case, rolling is applied to selected surfaces of the shaft initially shaped by machining. It is particularly purposeful

when low roughness and high fatigue life of selected surfaces is required. The rolling mill shown in Figure 2b can work in pulling as well as pushing system, and is equipped with an automatic changer that exchanges the forming rolls and the formed shafts. The maximal force of cold work of the rolls equals 440 kN, the longitudinal rolling force 240 kN, the rolling speed is 1.5–5 m/min, and the total installed power is 22 kW [6].

5. Summary

The technology of longitudinal rolling of stepped shafts is fully competitive to conventional machining in small-lot production, as well as in mass production. The main advantage of the method is that it makes it possible to form finished surfaces of shafts made of alloy steel after quenching and tempering. Another good point is strengthening of shaft's material by cold work, which improves its static strength properties and increases fatigue life.

The research have shown that the process of longitudinal cold rolling of shafts made of alloy steel 40HNMA, quenched and tempered to the hardness 34HRC before rolling, evidently improves material's strength properties. The state of stress arising during rolling influences the value of conventional yield point $R_{0.2}$. The tensional strength R_m is the same, in the whole range of strain, for shafts made by pulling and pushing method. The conventional yield point $R_{0.2}$ in the strain range $\varepsilon_1 = 1.25\text{--}3.41$ in the shafts formed by pulling method is generally higher than that in shafts made by pushing method. However, at any given relative strain ε_1 , microscopic images and scanning photographs obtained in fractographic and metallographic examinations have not shown any differences in of material structure between the two methods. Both in pulling and pushing method one observed the development of material texture with the increase of strain.

References

- [1] Jezierski J. et al.: *Forming stepped shafts by longitudinal rolling method* (in Polish), *Mechanik*, No. 11, 1983.
- [2] Kowalik M., Trzepieciński T.: *Numerical modelling of longitudinal rolling process of circular-section shafts* (in Polish), *Prace Naukowe Politechniki Warszawskiej, Mechanika*, Warszawa, 2009, Vol. 226.
- [3] Kowalik M.: *Influence of surface roughness on thrust force value in finishing rolling of stepped shafts* (in Polish), *Mechanik*, No. 4, 2010.
- [4] Kowalik M.: *Examination of selected mechanical properties of stepped shafts made by cold longitudinal rolling with different degree of elongation. PhD Thesis*, Radom Technical University, 1996.
- [5] Przybyłowicz K.: *Metaloznawstwo*, WNT Warszawa, 1992.
- [6] *The report CBPR 02.04 from investigations of longitudinal rolling*, Years 1987–1990.
- [7] *MSC Marc Volume B: Element Library*, MSC Software Corporation, 2005.

Zastosowanie metody walcowania wzdłużnego na zimno w masowej produkcji wałków stopniowanych w silnikach spalinowych

Artykuł prezentuje mało znaną nowoczesną i innowacyjną technologię kształtowania na zimno wałków stopniowanych. Jest to metoda kształtowania części maszyn na gotowo, w której wykorzystane jest umocnienie materiału poprzez zgniot. W pracy zaprezentowano wyniki z badań wpływu stanu naprężenia podczas kształtowania plastycznego na zimno na strukturę materiału i własności wytrzymałościowe. Badania przeprowadzono na wałkach otrzymanych metodą walcowania wzdłużnego na zimno (LCR) ze stali stopowej ulepszonej cieplnie przed kształtowaniem do twardości 34HRC. Pokazano wpływ wielkości odkształcenia na zmianę struktury i wzrost wytrzymałości materiału. Załączono przykłady zastosowania technologii CLR do wytwarzania części typu wałek przeznaczonych do silników spalinowych.



Multiscale modelling of microstructure evolution during laminar cooling of hot rolled DP steels

M. PIETRZYK, Ł. MADEJ, Ł. RAUCH, R. GOŁĄB

Akademia Górniczo-Hutnicza, ul. Mickiewicza 30, 30-059 Kraków, Poland.

Accelerated cooling of DP steel strips after hot rolling is considered in the paper. The work is focused on the multi scale model based on the Cellular Automata method as well as on conventional models. Dilatometric tests were performed to identify the coefficients in the models for a DP steel. These models are implemented in the computer system, which simulates controlled cooling of products after hot rolling. This system is described briefly in the paper. Results of numerical tests, which show an influence of the cooling parameters on the structure of the DP steels, are presented in the paper, as well. Arbitrary laminar cooling system, composed of n_1 boxes in the first section and n_2 boxes in the second section, is considered. Such parameters as strip thickness and velocity, the number of active boxes in the first section of the laminar cooling, the time interval between the two sections and water flux in the sections were independent variables in the analysis. The optimal cooling schedule is the main result of the work.

Keywords: *dual phase steels, laminar cooling, phase transformation models, cellular automata*

1. Introduction

Dual Phase steels belong to a group of steel grades widely used in the automotive industry. Two phase microstructure containing predominantly ferrite and 20–30% of martensite, is the basis of certain special properties of these steels. Required relation between volume fractions of ferrite and martensite, which is crucial for the quality of steel, is obtained through special heat treatment during laminar cooling after rolling. However, proper control of cooling parameters in this process is difficult. That is the reason why computer simulation of phase transformation during cooling plays an important role in design of the optimal cooling conditions. Application of the conventional models of phase transformations based on the Avrami equation [1] to design of the laminar cooling parameters is described in the earlier work [2]. There are certain limitations of this model, which encouraged Authors to search for more advanced solutions capable to account explicitly for the material microstructure. Since cellular automata (CA) were successfully used by various researchers to modelling phase transformations [3–4], this technique was selected in the present work. The first attempt of application of the CA method to modelling phase transformations in DP steels is described in [5]. The objective of the present work is to

develop further, as well as to test and validate, the model of phase transformations for the DP steels based on the CA technique and to compare it with the conventional models. Process of laminar cooling of these steels after hot rolling was selected as an example for simulations.

2. Dual phase steels

Structure of the DP steels is composed of ductile ferrite and hard martensite. Volume fraction of martensite F_m in majority of products does not exceed 30% [6]. Such phase composition and second phase morphology give high strength and ductility of products. The main features of DP steels are:

- Lack of the yield point.
- Low $R_{0.2}/R_m$ ratio, within 0.50–0.75, which prevents steep gradients of stresses in cold formed products.
 - High hardening coefficient, particularly at low strains, which reduces residual stresses in cold formed products.
 - Large uniform and total elongations.
 - The DP steel strips can be obtained in two ways:
 - For thick strips, directly after hot rolling. Two stages of laminar cooling are applied. During the first stage the strip is cooled rapidly to the ferritic transformation temperature and maintained at this temperature until the required volume fraction of ferrite is reached. Rapid cooling is applied in the second stage and the remaining austenite is transformed into martensite.
 - For thin strips, after cold rolling and continuous annealing, often combined with galvanizing or coating [6–7]. Conventional laminar cooling is applied after hot rolling and typical ferrite-pearlite microstructure is obtained. Cold rolling and continuous annealing is applied next and the required two-phase structure is obtained by relevant control of temperatures during the latter process.

3. Conventional model

The model is based on the Avrami type equation:

$$X_f = 1 - \exp(-kt^n), \quad (1)$$

where:

X_f – volume fraction of ferrite,

t – time,

k, n – coefficients.

Following [8], coefficient k in Equation (1) is introduced as modified Gauss distribution function of temperature:

$$k = k_m \exp \left\{ - \left[\frac{\sqrt{(T - T_{\text{nose}})^2}}{q} \right]^p \right\} \quad (2)$$

The four coefficients k_m , T_{nose} , q and p allow description of all shapes of the CCT curves in a quite intuitive way. Thus, k_m is the maximum value of k , T_{nose} is a temperature position of the nose of the Gaussian function, p is proportional to the nose width at mid height and q is related to the sharpness of the curve. Equation (2) is used for ferritic transformation only. Pearlitic and bainitic transformations are simulated also by Equation (1), but the coefficient k is defined by a simpler, then Equation (2), function of the temperature, which is not discussed here. Martensite volume fraction is calculated from the Koistinen and Marburger equation, see for example [9]. All coefficients in the model were determined using inverse analysis [10] of the dilatometric tests. For the ferritic transformation they are: $k_m = 0.0663$, $T_{\text{nose}} = 965.2$ °C, $q = 26.95$, $p = 2.41$. Avrami exponent $n = 2.475$. The coefficients for the remaining transformations are given in [5]. Comparison of the CCT diagram measured in the dilatometric tests and predicted by the model with optimal coefficients is shown in Figure 1. Except the end of the bainitic transformation, excellent agreement between measurements and predictions is obtained.

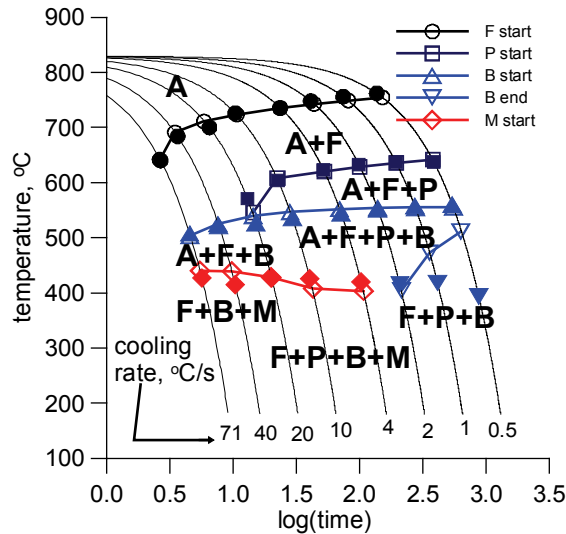


Fig. 1. CCT diagram for the DP steel obtained from measurements (filled symbols) and calculated by the model with the optimal coefficients (open symbols)

Following the idea presented in [11], the conventional model is implemented in the FE code, which simulates laminar cooling. The current values of temperatures calculated by

the FE code are used for simulations of phase transformations. On the other hand, the heat generated by the transformations, which is calculated by the phase transformation model, is accounted for in the FE analysis. This complex model is used for optimization of the laminar cooling for the process, in which the DP microstructure is obtained after hot rolling. Typical laminar cooling system, composed of 40 boxes in the first section and 40 boxes in the second section, is considered. As it is shown in [2], the square root error between calculated and required volume fraction of martensite is the objective function and optimization yields the cooling parameters, which give the minimum of this function. Figure 2 shows an example of relation between number of active boxes in the first section of the laminar cooling system and volume fraction of phases.

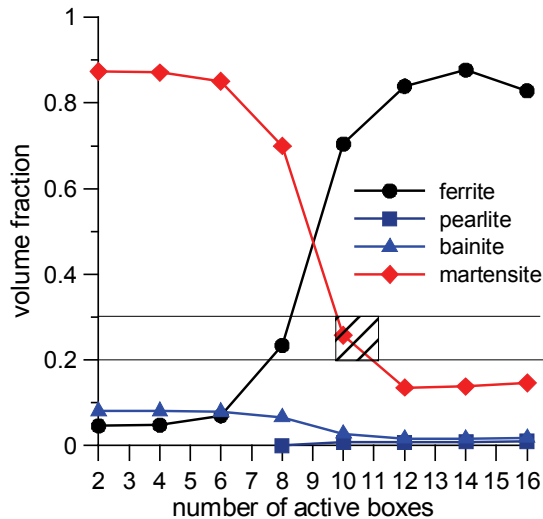


Fig. 2. Volume fraction of phases as a function of number of active boxes in the 1st section of the laminar cooling, when box no. 1 is the first active box in the 2nd section

It is seen that required volume fraction of martensite is obtained for 10–11 active boxes. The developed phase transformation model provides an information regarding the phase fractions in the material. However, very often it is also important to know the geometry of the obtained microstructure. To provide such information a discrete phase transformation model that takes the geometry of the microstructure into account has to be developed.

4. CA model

As it has been mentioned, predictive capabilities of the conventional model are limited to average values of the microstructural parameters. CA model was selected as a method, which can supply more advanced information about the microstructure evolution during the phase transformations. The approach based on digital material

representation is used in this work [12]. Basic principles of the CA model are given below. The conventional model, which is described above in Section 3, is used for validation of the developed CA model.

4.1. Description of the model

At this stage of the project the CA model is designed to simulate ferritic transformation during cooling in the 2D and 3D space. Each CA cell is described by the several state and internal variables in order to properly describe state of the material. The cell can be in three different states: ferrite (α), austenite (γ) and ferrite-austenite (α/γ), as shown in Figure 3. The last state is used to describe CA cells located at the interface between austenite and ferrite grains. Additionally, internal variables are defined to describe other necessary microstructure features. Cells contain information e.g. how many ferrite phase is in a particular cell X_{cf} , what is the carbon concentration in each cell C_c , the growth length l of the ferrite cell into the ferrite-austenite cell or the growth velocity v of an interface cell. The internal variables are used in the transition rules to replicate mechanisms of phase transformation. Similar solutions based on the CA method are also available in the literature [4].

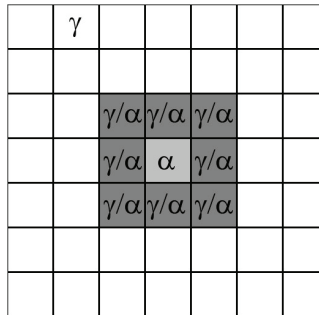


Fig. 3. Illustration of the nucleus of the ferrite phase and the surrounding cells in the ferrite-austenite (α/γ) state

Two transition rules are defined to describe nucleation and growth of ferrite phase. Nucleation is stochastic in nature. Various approaches to describe this process were proposed in [4]. In the present model, to replicate this stochastic character of nucleation, a number of nuclei N_{nuc} is calculated in a probabilistic manner at the beginning of each time step. Beyond this, locations of grain nuclei are generated randomly along grain boundaries. When a cell is selected as a nuclei, the state of this cell changes from austenite (γ) to ferrite (α). At the same time all the neighbouring cells of the ferrite (α) cell change their state to ferrite-austenite (α/γ) (Figure 1). After nucleus appears in the CA space, the growth of ferrite phase is calculated in the following steps. However, nucleation process has a continuous character and it occurs during the entire CA simulation until the end of transformation.

The transition rules describing growth of ferrite grains during phase transformation are designed to replicate experimental observations of mechanisms responsible for this process [2, 13]. It is well known that the recently formed ferrite nuclei grow into the austenite phase. The velocity of the γ/α interface is assumed to be a product of the mobility M and the driving force for interface migration F :

$$v = MF = M_0 D(T) F = M_0 D_0 \exp\left(\frac{Q}{RT}\right) F, \quad (3)$$

where:

- M_0 – mobility coefficient,
- T – absolute temperature,
- D – diffusion coefficient,
- D_0 – basic value of the diffusion coefficient.

The driving force for the phase transformation F is a sum of the mechanical driving force F_{mech} and chemical driving force F_{chem} . The former is neglected in the present model. The latter is due to differences in the chemical potential of iron atom in austenite (μ_{Fe}^γ) and ferrite (μ_{Fe}^α) phases at the interface:

$$F_{\text{chem}} = \mu_{Fe}^\gamma - \mu_{Fe}^\alpha. \quad (4)$$

The following transition rules are proposed in the paper to replicate the phenomena occurring at the austenite-ferrite boundary. When the ferrite phase is present in the material, the CA ferrite cells grow into the austenite phase. In the current time step t the growth length of the ferrite cell with indexes (i, j) towards a ferrite-austenite neighbouring cell with indexes (k, l) is described by [4]:

$$l_{i,j}^t = \int_{t_0}^t v_{i,j} dt, \quad (5)$$

where:

- t_0 – time when the CA cell (i, j) changed into the ferrite state,
- $v_{i,j}$ – the growth velocity of the CA cell (i, j) .

The growth velocity v is calculated from Equation (3) and then the ferrite volume fraction in the CA cell (k, l) is calculated as a results of the ferrite growth:

$$F_{k,l} = \sum_1^{N_{\text{neigh}}} \frac{l_{i,j}^t}{L_{CA}}, \quad (6)$$

where:

$F_{k,l}$ – total ferrite volume fraction in the CA cell (k, l), as a contribution from all the neighbouring ferrite CA cells,

L_{CA} – dimension of a CA cell in the space,

superscript t – number of the time step.

Based on these calculations the transition rule is defined as follows:

$$Y_{k,l}^{t+1} = \begin{cases} \text{ferrite} \Leftrightarrow Y_{k,l}^t = \alpha / \gamma \wedge F_{k,l}^t > F_{cr} \\ Y_{k,l}^t \end{cases}, \quad (7)$$

$$Y_{k,l}^{t+1} = \begin{cases} \alpha / \gamma \Leftrightarrow Y_{k,l}^t = \text{austenite} \wedge Y_{i,j}^t = \text{ferrite} \\ Y_{k,l}^t \end{cases}, \quad (8)$$

where:

$Y_{k,l}^t$ – state of the cell (k, l) in the time step t ,

$Y_{k,l}^t$ – state of the neighbouring cell (k, l) in the time step t ,

F_{cr} – critical value of the volume fraction of ferrite in a cell.

The CA cell changes the state from *austenite-ferrite* into *ferrite* when ferrite volume fraction in this cell exceeds the critical value F_{cr} . Otherwise the cell remains in the *austenite-ferrite* state. When the cell changes its state to *ferrite*, all the neighbouring cells in the *austenite* state change their states into the *austenite-ferrite*. When a change in the cell state occurs, the corresponding carbon concentration changes according to the FeC diagram. Since the diffusion is not considered directly in the present model, the carbon concentration in the austenite CA cells increases uniformly. The effect of diffusion is accounted for by relation of the phase boundary mobility on the diffusion coefficient, see Equation (3).

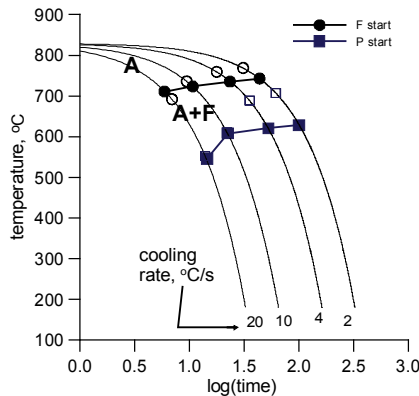


Fig. 4. Part of the CCT diagram obtained from measurements (filled symbols) and calculated by the CA model (open symbols) for the ferritic (F) and pearlitic (P) transformations

The parameters in the CA model were identified using an inverse analysis of the start temperature data obtained from the dilatometer. The results are presented in Figure 4. Good agreement between measurements and predictions is obtained.

Modelling of the three stage laminar cooling is selected for validation of the CA model. During the first stage the strip is cooled rapidly to the ferritic transformation temperature and maintained at this temperature until the required volume fraction of ferrite is reached. Rapid cooling is applied in the third stage and the remaining austenite is transformed into martensite. Three variants are considered. The rapid cooling is applied until the temperature reaches 650, 700 and 750 °C, respectively in variants 1 to 3. Calculated changes of the carbon concentration in the austenite during the two-stage cooling are presented in Figure 5. Corresponding microstructures obtained after these three variants are presented in Figure 6. Brighter phase in Figure 6 represents the ferrite grains obtained after transformation.

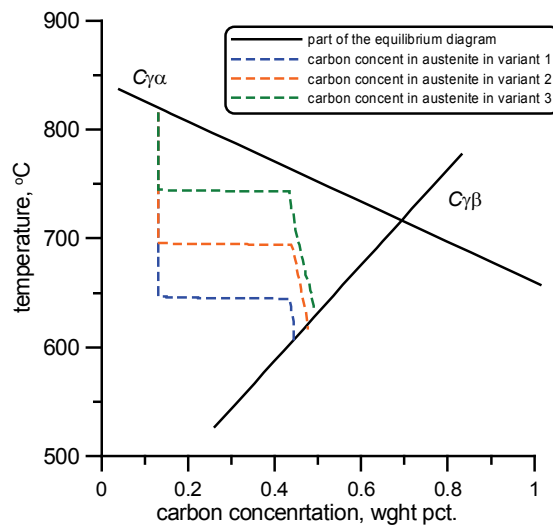


Fig. 5. Changes of the average carbon content in the austenite during two stage cooling of the DP steel, compared with the equilibrium carbon content at the austenite-ferrite ($C_{\gamma\alpha}$) and austenite-cementite ($C_{\gamma\beta}$) boundaries for four cooling variants

Comparison of the conventional and the CA models is shown in Figure 7. Predictions of the time necessary to obtain 70% volume fraction of the ferrite at various temperatures are compared. It is seen that large discrepancies between the two models occur for the temperatures of maximum rate of the transformation. It should be emphasized, however, that at this stage of the project the CA model is identified for the start temperature of the transformation only. As far as the kinetics of the transformation is considered, the coefficients of the model are not identified but assumed, what is the reason of discrepancies in predictions of the pearlite start temperatures (Figure 4) and predictions of the kinetics of the ferritic transformation in the temperature range 680–720 °C (Figure 7).

Improvement of the model, as far as the accuracy of predictions of kinetics of transformation are considered, is the objective of further work.

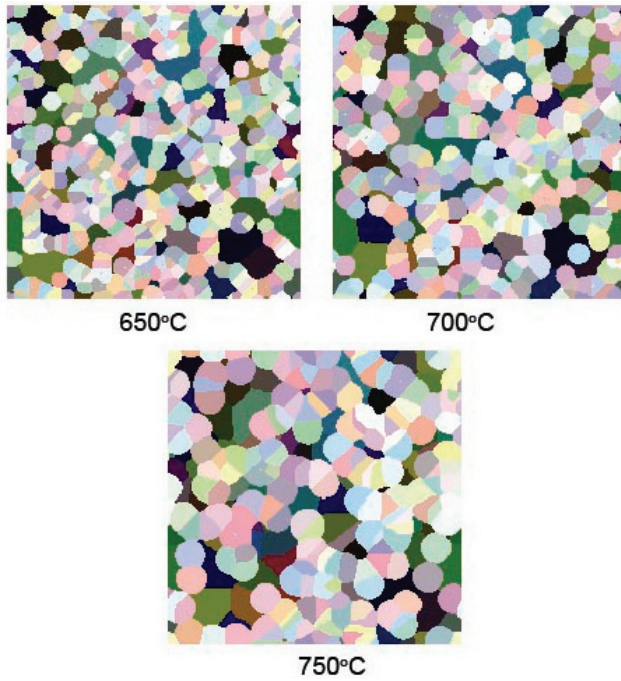


Fig. 6. Picture of the microstructures obtained after the two stage cooling of the DP steel for three cooling variants, (brighter phase represents the ferrite grains)

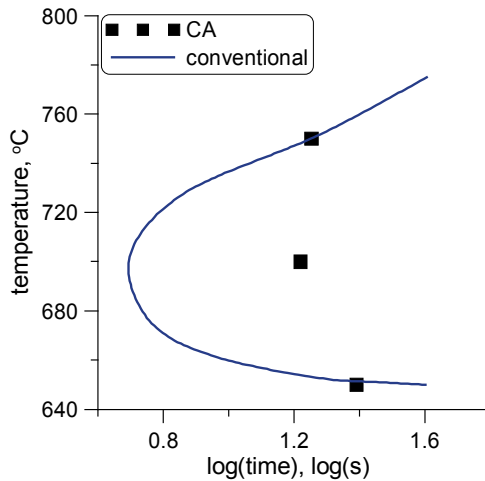


Fig. 7. Time to obtain 70% volume fraction of ferrite at various temperatures

5. Discussion

The first attempt of application of the cellular automata method to simulation of laminar cooling of DP steels is described in the paper. Behaviour of the cellular automata model for cooling schedules characteristic for DP steels was tested and good results were obtained. Changes of carbon concentration during laminar cooling of DP steels are in qualitative agreement with those predicted by the conventional model, which was identified using inverse analysis of dilatometric tests. It is shown that the CA model predicts properly start temperature for the austenite-ferrite transformation (Figure 4). Predictions of the kinetics of this transformation are in qualitative agreement with the conventional model (Figure 7) but quantitative agreement is not satisfactory. Identification of the coefficients of the CA model is the objective of future works.

It is shown in the paper, however, that predictive capabilities of the CA model are much wider comparing to the conventional models. They compose shape of grains and their distribution, as it is shown in Figure 6. Therefore, in future works the identified CA model will be implemented into the FE code and applied to the optimization of the laminar cooling process for DP steels.

Acknowledgements

Financial assistance of the MNiSzW, project no. 11.11.110.856, is acknowledged. One of the Authors (LM) is grateful for the financial support from the Foundation for Polish Science within the Start program.

References

- [1] Avrami M.: *Kinetics of phase change*, I. General theory, Journal of Chemical Physics, Vol. 7, No. 1, 1939, pp. 1103–1112.
- [2] Pietrzyk M., Kusiak J., Kuziak R., Zalecki W.: *Optimization of laminar cooling of hot rolled DP steels*, XXVIII Verformungskundliches Kolloquium, Planeralm, 2009, pp. 285–294.
- [3] Zhang L., Zhang C.B., Wang Y.M., Wang S.Q., Ye H.Q.: *A cellular automaton investigation of the transformation from austenite to ferrite during continuous cooling*, Acta Materialia, Vol. 51, No. 18, 2003, pp. 5519–5527.
- [4] Lan Y.J., Li D.Z., Li Y.Y.: *Modelling austenite decomposition into ferrite at different cooling rate in low-carbon steel with cellular automaton method*, Acta Materialia, Vol. 52, No. 6, 2004, pp. 1721–1729.
- [5] Pietrzyk M., Madej Ł., Rauch Ł., Spytkowski P., Kusiak J.: *Conventional and multiscale modelling of austenite decomposition during laminar cooling of hot rolled DP steels*, XXIX Verformungskundliches Kolloquium, Planeralm, 2010, pp. 41–46.
- [6] Pichler A., Hribernik G., Tragl E., Angerer R., Radlmayr K., Szinyur J., Traint S., Werner E., Stiaszny P.: *Aspects of the production of dual phase and multiphase steel strips*, Proc. 41st MWSP Conf., ISS Vol. XXXVII, Baltimore, 1999, pp. 37–60.
- [7] Hofmann H., Mattissen D., Schaumann T.W.: *Advanced cold rolled steels for automotive applications*, Steel Research International, Vol. 80, No. 1, 2009, pp. 22–28.

- [8] Donnay B., Herman J.C., Leroy V., Lotter U., Grossterlinden R., Pircher H.: *Microstructure evolution of c-mn steels in the hot deformation process: the STRIPCAM model*, Proc. Modelling of Metal Rolling Processes Conf., eds. J.H. Beynon, P. Ingham, H. Teichert, K. Waterson, London, 1996, pp. 23–35.
- [9] Umemoto M., Hiramatsu A., Moriya A., Watanabe T., Nanba S., Nakajima N., Anan G., Higo Y.: *Computer modelling of phase transformation from work-hardened austenite*, ISIJ International, Vol. 32, 1992, pp. 306–315.
- [10] Pietrzyk M., Kondak T., Majta J., Zurek A.K.: *Method of identification of the phase transformation model for steels*, Proc. COM 2000 Conf., Ottawa, 2000, CD ROM.
- [11] Pietrzyk M.: *Finite element based model of structure development in the hot rolling process*, Steel Research, Vol. 61, No. 12, 1990, pp. 603–607.
- [12] Madej L., Rauch L., Yang C.: *Strain distribution analysis based on the digital material representation*, Archives of Metallurgy and Materials, Vol. 54, No. 3, 2009, pp. 499–507.
- [13] Christian J.W.: *The theory of transformation in metals and alloys*, 1–2, Pergamon, London, 2002.

Wieloskalowy model rozwoju mikrostruktury podczas laminarnego chłodzenia stali DP walcowanych na gorąco

Tematem niniejszej pracy jest analiza zmian mikrostruktury podczas chłodzenia stali DP walcowanych na gorąco. W trakcie analizy wykorzystano dwa modele przemiany fazowej, bazujące na metodzie automatów komórkowych i na równaniu Avramiego. W każdym przypadku do identyfikacji opracowanych modeli przemian fazowych wykorzystano wyniki prób dylatometrycznych. Modele wprowadzono do opracowanego systemu komputerowego, który umożliwia projektowanie technologii kontrolowanego chłodzenia stali walcowanych na gorąco. Uzyskane wyniki symulacji numerycznych pokazujące wpływ parametrów procesu chłodzenia (np. ilość aktywnych skrzyń chłodzących w pierwszej i drugiej sekcji, czas przerwy pomiędzy sekcjami, grubość pasma, ciśnienie wody) na strukturę stali DP zamieszczono w niniejszej pracy. Głównym wynikiem jest opracowany optymalny schemat chłodzenia dla stali DP.



Analysis of the influence of a rivet yield stress distribution on the micro-SPR joint – initial approach

W. PRESZ, R. CACKO

Warsaw University of Technology, Narbutta 85, 02-524 Warszawa, Poland.

One of the limitations related with joining several micro parts is the temperature generated during joining methods based on material heating. Temperature concentration could be a reason of severe difficulties with micro-manufacturing applications. It seems that modern mechanical joining technologies could significantly facilitate micro-parts fastening, since there is lack of temperature development during the process. Recently mechanical joining methods undergo considerable development and become more and more competitive in the industry. Among them, the self-piercing – SPR – technology is one of the most advanced and flexible. Initially, the automotive industry was a first application of the SPR, and then have been started to be use in other industry areas. In the paper, possibility of micro-rivet production by micro-forming with heat treatment elimination has been researched by means of FEM analysis. Required rivet strength is achieved by designed cold forming process and followed by effect of material hardening.

Various stress distributions in the rivets are taken into account during numerical simulation to prove their influence on joining quality. Commercial FEM software MSC.Marc is used for numerical simulations.

Keywords: *self-piercing riveting, micro-forming, micro-mechanical joining*

1. Introduction

Miniaturisation of electronic and electric equipment is present during recent decades. Today one observes a stormy development of micro-mechanical systems often based on piezoelectric drives [1]. Construction of such systems needs suitable joining methods. In many cases joining process should not, even locally, results of temperature increase. Concerning this requirement the group of mechanical joining methods appears as a promising solution.

As it has been observed in case of almost all micro-technologies, knowledge concerning macro-processes can not be transferred into the micro world basing on simple geometrical scaling. One should here expect all consequences of similarity theory. Usually old knowledge must be thorough reformed. The new area for, let introduce now the name *micro-mechanical joining* processes, should be than reserved and isolated from mechanical joining processes in the macro-world. This suggestion seems to be analogical to that what has happened in the metal forming technology. At this area after many bad experiences the new topic called micro-forming was introduced. This

work depicts into this course. The self piercing riveting process was recognised as especially interesting for miniaturisation. Many works concerning various aspects of SPR, e.g. joinability or joint strength, are carried out recently, e.g. [2–3]. But there are no research concerning possibility of SPR miniaturisation, yet.

There are a lot of types of commercially available rivets depending on shape, material, preparation, etc. They are supplied usually in hardened and tempered form to assure suitable hardness to provide optimum joint properties in the full range of application materials. This kind of rivet preparation gives in general uniform yield stress distribution within a rivet. Some of the rivets are coated, mainly for certain applications, to satisfy higher corrosion resistance conditions. As it has been previously proved micro-forming technology let to obtain high accuracy and surface quality [4] that in some cases might be increased with process modifications [5] or ultra-fine grained materials usage [6]. In this research, strength requirements of micro-rivets are fulfilled by strain hardening effect during suitable cold micro-forming process. Comparison of joining ability of four types of micro-rivets were done. They are differed in the material properties only as a consequence of manufacturing technology.

2. Micro-rivets for numerical analysis

As a base for investigations one most commonly type of rivet shape marked as 5×7 [7] has been chosen, Figure 1. This shape was scaled to the micro-dimensions specified there and was used in all simulations. Four types of rivets were taken into account named as: micro-rivet-A, B, C and D.

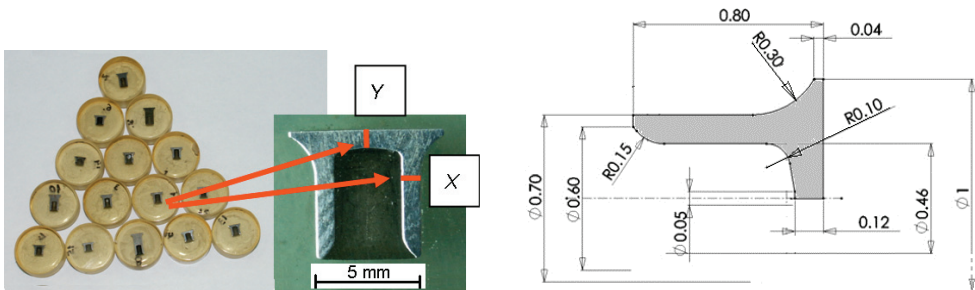


Fig. 1. Rivet 5×7 shape chosen from several types (left), micro-hardness test zone and micro-rivet dimensions

2.1. Micro-rivet-A and micro-rivet-B

Micro-rivets properties were defined based on investigations on already mentioned 5×7 rivet. Material of this rivet is 13CrMo4-5 DIN equivalent. Rivet manufacturing process is not precisely known. Rivets are provided in hardened state (usually by heat treatment) after manufacturing. To verify distribution and level of a yield stress in the rivet, micro-hardness tests have been done in two selected zones, Figure 1: along axis

of symmetry (the head of the rivet, Y) and through the rivet leg (X). Results collected in the Table 1 confirmed that uniform yield stress distribution is detected. The yield stress is calculated using simplified, engineering equation relating hardness and the yield stress [8], Table 2. Therefore, initial state of material of micro-rivet-B is defined as uniform, with calculated yield stress and specified stress-strain curve. For comparison and also for simulation method verification, micro-rivet-A has uniformly distributed yield stress equal to the initial yield stress of 13CrMo4-5 DIN material, Table 2.

Table 1. Selected examples of hardness tests for zone A and B (HV scale)

Riv. No.	Zone Y					Zone X				
1	254	257	263	257	262	257	263	269	263	257
2	267	252	253	255	259	265	261	259	260	260
3	259	262	263	249	264	260	255	262	256	249

2.2. Micro-rivet-C

The rivet resulting from numerical simulation of micro-forming and micro-forming scheme itself are presented in Figure 2.

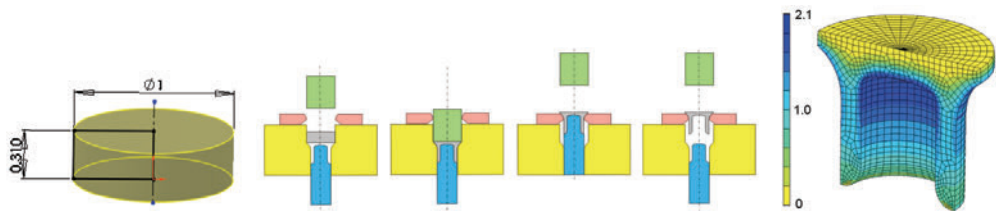


Fig. 2. Slag, final shape and schema of micro-forming process of micro-rivet-C, calculated strain distribution

Forming process includes: 1 – insertion of cylindrical preform of dimensions $D = 1$ mm and $h = 0.38$ mm, 2 – simultaneous forward bar extrusion with punch of a flat head and forward cup extrusion over the cylindrical counter-punch with a convex head with outer diameter $d_z = 0.7$ mm and inner diameter $d_w = 0.46$ mm, 3 – punch withdrawal, 4 – rivet remove with a counter-punch moved beyond the die space, 5 – clamping divided remover, 6 – counter-punch withdrawal, 7 – rivet removal.

2.3. Micro-rivet-D

Micro-rivet as a result of a numerical simulation and a rivet micro-forming process is shown in Figure 3.

The second process covers following stages: 1 – insertion into die cavity cylindrical preform of dimensions $D = 0.7$ mm and $h = 0.78$ mm, 2 – forward extrusion with a flat punch of a diameter $d_{s1} = 0.7$ mm against cylindrical counter-punch of inner diameter $d_w = 0.46$ mm, 3 – flat punch no. 1 withdrawal, ($d_{s1} = 0.7$ mm), 3 – bottom part of

a workpiece movement to conical part of the die, 4 – punch no. 1 replacement for punch no. 2, 5 – upsetting of a bottom part with a flat punch no. 2 of diameter $d_{s2} = 1$ mm, 6 – rivet push out by counter-punch beyond die space, 7 – divided remover clamping, 8 – counter-punch drawback, 9 – getting out a rivet from the remover.

Strain distribution obtained after micro-forming simulation, Figure 2 and 3, is taken into account as an initial state for further numerical simulation of micro-riveting.

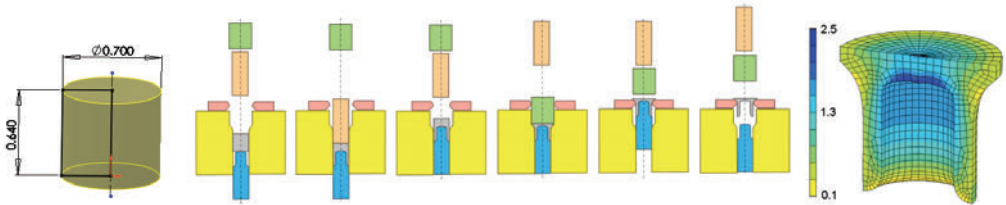


Fig. 3. Slag, final shape and schema of micro-forming process of micro-rivet-D, calculated strain distribution

3. Analysis of micro-SPR joinability

General numerical model of the micro-SPR, Figure 4, consists of two 0.3 mm deformable layers, deformable rivet and rigid tools: punch, blank holder and die. Die profile has been selected based on earlier experiments [9]. Uniform friction coefficient of $\mu = 0.1$ over all interfaces has been assumed. The model is isothermal and static. Elastic-plastic material model is assumed for deformable parts. Elastic properties of aluminum alloy sheets are defined by Young modulus $E = 75.000$ MPa, and for the rivet steel $E = 210.000$ MPa. Stress-strain curve for aluminium alloy: $\sigma_p = 306\epsilon^{0.189}$, and for steel 13CrMo4: $\sigma_p = 857\epsilon^{0.212}$. Initial yield stress for analysis is gathered in Table 2.

Table.2 Initial yield stress for rivets in particular simulation

	Rivet A	Rivet B	Rivet C	Rivet D
Initial stress [MPa]	$\sigma_{p0} = 290$ uniform	$\sigma_{p0} = 910$ uniform	calculated by FEM of rivet micro-forming non-uniform	calculated by FEM of rivet micro-forming non-uniform

There are four modifications of base numerical model. The differences rely on a rivet material state, described above. Final stages of the simulations are presented in Figure 5. In the first simulation, it was assumed that the rivet is without any initial stress (machining production), Figure 6 – A, material of the rivet for the second model has been defined with uniform yield stress field and yield stress 3 times higher than raw material, Figure 6 – B. The third and the fourth simulations have initial condition in form of yield stress distribution over the rivet. It was obtained from two different simulations of micro-rivet forming processes, Figure 6 – C and D.

Results show that a rivet made of a raw material, can not be applied for joining this particular materials. The second model, with uniform stress field corresponding with measured commercial 5×7 rivet gives expected good shape of a rivet joint. The most interesting, however, are results of the third and fourth models. It seems that both rivets are strong enough to fulfill good micro-SPR joints. Based on the standard guidelines for SPR qualitative strength of the joint might be estimated based on shape of a joint and joining force.

In those cases one can observe negligible differences in shape of the joints, and maximum clamping force, Figure 5, is almost the same. These two features promise a good strength of a joint.

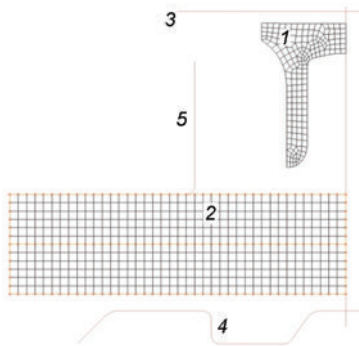


Fig. 4. FEM model of the SPR process;
1 – rivet, 2 – sheets, 3 – punch,
4 – die, 5 – blank holder

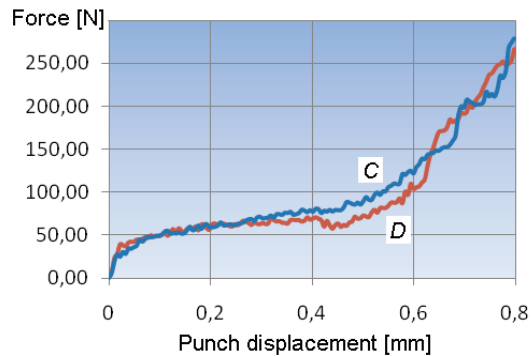


Fig. 5. Force flow for models C and D

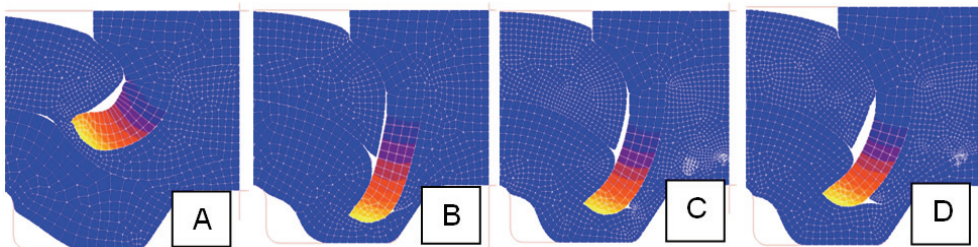


Fig. 6. Final stage of the micro-SPR process simulations for selected rivet material stages:
A – raw material, B – max. uniform stress field, C, D – stress distribution obtained
after different rivet forming process

4. Final remarks

The main goal of the research is to develop of manufacturing technique for mass production of micro-rivets by cold micro-forming operations. In this process required strength of a rivet is obtained by strain hardening to eliminate commonly used heat

treatment. This work is an initial stage of research that is FEM simulation of both forming of a micro-rivet and micro-joining.

It was numerically proven that two designed processes of micro-rivet forming gave rivets strong enough to obtain micro-SPR joints of a good quality.

In the future work it is planned first to take into account tools-strength aspects which were neglected in the current analysis. Then, carry on both experimental and numerical study of various phenomena of selected process, especially considering influence of scale effects.

Acknowledgements

The work has been done under scientific project N508 446136, financed by Polish Ministry of Science.

References

- [1] Presz W., Andersen B., Wanheim T.: *Piezoelectric driven micro-press for microforming*, Journal of Achievements in Materials, Vol. 18, No. 1–2, 2006, pp. 411–414.
- [2] Dae-Wook Kim, Jun Xu, Wei Li, Blake D.: *Force characteristics of self-piercing riveting*, Proceedings of the Institution of Mechanical Engineers, Part B: Journal of Engineering Manufacture, Vol. 220, No. 8, 2006, pp. 1259–1265.
- [3] Abe Y., Kato T., Mori K.: *Joinability of aluminium alloy and sheets by self piercing riveting*, Journal of Materials Processing Technology, Vol. 177, No. 1–3, 2006, pp. 417–421.
- [4] Presz W., Rosochowski A.: *The influence of grain size on surface quality of micro-formed components*, The 9th Int. Conf. ESAFORM, Glasgow, 26–28 April, 2006, pp. 587–590.
- [5] Presz W.: *Contact phenomena in micro-blanking*, The 11th Conf. ESAFORM, Lyon, April 23–25, 2008.
- [6] Olejnik L., Presz W., Rosochowski A.: *Backward extrusion using micro-blanked aluminium sheet*, The 12th Int. Conf. ESAFORM, Twente, Netherlands, April 27–29, 2009.
- [7] Cacko R., Czyżewski P.: *Verification of numerical modelling of the SPR joint by experimental stack-up*, Computer Methods in Material Science, Vol. 7, No. 1, 2007, pp. 124–129.
- [8] Rowe G.W.: *Principles of industrial metal forming processes*, Edward Arnold Ltd., 1986, pp. 30.
- [9] Cacko R., Czyżewski P., Kocańda A.: *Initial optimization of self-piercing riveting process by means of FEM*, Steel Grips, No. 2, 2004, pp. 307–310.

Wpływ rozkładu naprężenia uplastyczniającego w mikronicie na możliwość powstania połączenia w procesie mikro-SPR

W łączeniu niektórych mikroelementów ograniczeniem doboru technologii jest możliwość wystąpienia miejscowych wzrostów temperatury. Warunek ten spełniają nowoczesne metody mechanicznego łączenia. W pracy opisano wstępną analizę zastosowania jednej z tych metod

– nitowania bezotworowego. Metoda ta jest z powodzeniem stosowana w różnych dziedzinach techniki, ale nie była dotychczas użyta w odniesieniu do mikroelementów. W pracy przeanalizowano możliwość produkcji mikronitów technologią mikrokształtowania plastycznego na zimno. Efekt umocnienia materiału pozwala na wyeliminowanie standardowo stosowanej obróbki cieplnej. Na drodze symulacji MES porównano wpływ różnych sposobów uzyskania mikro-nitów na przebieg procesu mikrołączenia i jakość połączeń. Wykorzystano komercyjne oprogramowanie MSC.Marc.



On the problem of material properties in numerical simulation of tube hydroforming

H. SADŁOWSKA, A. KOCĄNDA

Warsaw University of Technology, Narbutta 85, 02-525 Warszawa, Poland.

Hydroforming is a cost effective way of shaping various metals and alloys into lightweight, structurally stiff and strong pieces. The largest applications of hydroforming can be found in the automotive and aerospace industries. Among them, exhaust system components such as T-shapes or X-shapes connectors have been often manufactured by tube hydroforming. Typical tube hydroforming operation is made by a controlled application of internal pressure and axial feeding of tube material into deformation zone. The loading path of internal pressure versus axial feeding is the most important. It can be found by means of FEM simulation of the process to limit costs of experiments. However, the appropriate numerical model requires experimental data on tube material properties. Some simplifications to use sheet metal properties instead of tube properties have not been reliable. Especially cold worked tubes with small diameters require special methods to determine material properties in axial and circumferential directions. Such methods have been presented in the paper including some remarks on specimens' preparation, experimental set-up and image processing for getting strain values.

Keywords: *tubes, material properties, anisotropy*

1. Introduction

With the increased use of shapes and tubes for hydroforming applications, it is important to evaluate the performance of formed material. In hydroforming process tubes can be formed into products with complicated geometry within the die cavity using internal pressure and axial compressive force. Tube hydroforming has many advantages over conventional manufacturing methods including: part consolidation, weight reduction, improved structural strength and fewer secondary operations [1]. However, the hydroforming process has some inherent problems like bursting, wrinkling and wall thinning. These phenomena depend on the choice of process parameters. These parameters can be obtained experimentally or by means of modern designing methods. Especially, FEM simulation has been the most often applied method in hydroforming design because of a relatively low cost. Therefore, the evaluation of optimized process parameters has been crucial within recent research on hydroforming. There are many papers describing numerical simulations on hydroforming. Many of them describe techniques detecting onset of failures (wrinkling, bursting, buckling) and designing of optimized load paths [2–5]. It is important to point out that the reliability of numerical simulation results depends on the quality of input data including material properties.

Generally, two kinds of tubes for hydroforming processes have been applied: tubes obtained by bending and seaming of sheet metal and drawn tubes. Mechanical properties of seamed tubes can be evaluated by standard methods before bending of sheet metal [6]. Then sheet metal properties can be used to estimate tube properties like elastic modulus, plastic strain-stress curve, anisotropy and limiting drawing curve. On the other hand, seamed tubes have a groove weld and heat-affected zone for which material properties are quite different than sheet metal properties. It is not a serious problem for most of the products. However, some automotive components cannot be hydroformed with using seamed tubes because of high quality requirements. Then seamless tube is the only choice to fulfil these requirements. Seamless tubes are produced by drawing. It means that material grains are elongated in the axial direction what results in different mechanical properties of tube material in circumferential and axial directions. This anisotropy would have a considerable influence on results of numerical simulations. Determination of mechanical properties of seamless tube in directions different than the axial one is quite difficult. This problem is especially serious as regarding to preparation of specimens for small diameter tubes.

Literature review reveals various attempts on finding mechanical properties of tubes for hydroforming processes. Standard tests of specimens cut out from tube in axial direction have usually been used [7–9]. However, there are two major limitations with using tensile test in the case of hydroforming. The firstly, the maximum strain before necking reached in tube hydroforming could be higher than found in the tensile [10]. The secondly, the properties of the tube during hydroforming may differ considerably from the properties of the base material due to the influence of the tube production [11]. Therefore, in FEM simulation, extrapolation errors may occur. For these reasons, the tube bulge test has been proposed for determination of material properties of tubes used in hydroforming processes. It has been shown that this test results better fits the material behavior than the tensile test results [10–13].

However, the tube bulge test requires specialized and expensive experimental set up and the range of tested tube diameters is usually limited. Tensile test is still an interesting choice to find tube material properties with relatively low cost of experiments. Tube specimens cut longitudinally and extended into the flat sheet could be tested in the same way as rolled sheets [14]. This method is not suitable for small diameter tubes with relatively high wall thickness. In such cases flattening of specimen introduces some strains and residual stresses into tube material. It results in different material properties of these specimens as comparing with the properties of initial tube.

The properties of tube material in circumferential direction can be found by means of tensile tests of rings cut from the tube [15]. This method has been suitable for high diameter tubes. This paper presents methods to determine material properties of cold worked seamless tubes with small diameters in axial and circumferential directions. Some details on specimens' preparation, experimental set-up and image processing for getting strain values are also presented.

2. Determination of tube properties in the axial direction

High dimensional accuracy seamless tube of 45 mm in outer diameter and 1.5 mm wall thickness (DIN 2391) was chosen for experiments. Tube material was St35 steel (Polish Standard) with chemical composition: 0.17% C, 0.4% Mn, 0.35% Si and 0.05% V. According to Polish Standard PN-EN 10002-1 + AC1 on testing tube material, specimens were cut out from the tube in axial direction, Figure 1.

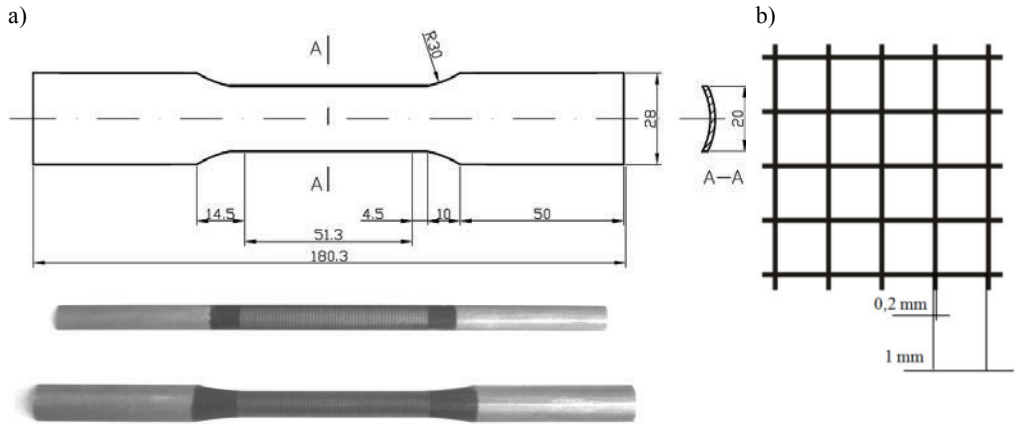


Fig. 1. Geometry of specimen cut out from the tube in axial direction (a), initial geometry of measuring grid (b)

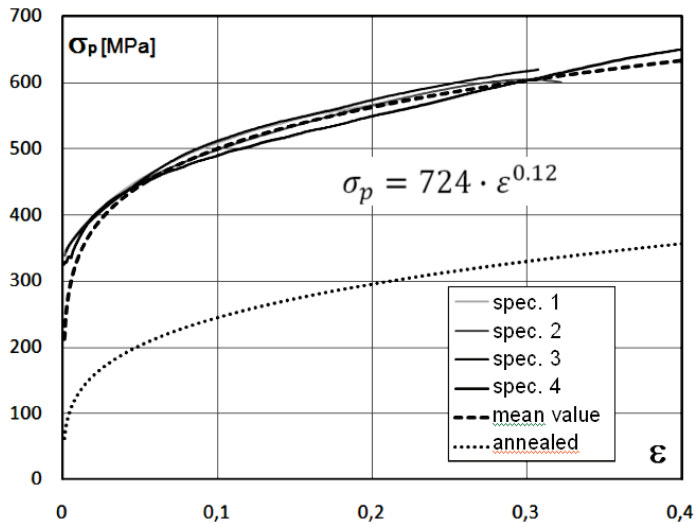


Fig. 2. Stress-strain curves obtained by means of tensile tests of 4 specimens cut out from the tube in axial direction

Universal testing machine combined with data acquisition system was used to carry out tensile tests of the specimens. The surface of gauge part of specimen was covered with quadratic grid made by laser. The grid was deformed during tensile test and the history of the deformation was registered by video system. Video camera was integrated with computer by means of Matrox Meteor card. Video images were analyzed with using Matrox Inspector software and especially its option Pattern Matching. Having found the coordinates of grid nodes for each step of specimen deformation, strain values were calculated. These strains were combined with stress values to get stress-strain curves, Figure 2. The mean course of stress-strain curve for 4 specimens is shown by broken line and could be described by the relation $\sigma = 724 \varepsilon^{0.12}$. As for comparison, stress-strain curve for annealed St35 steel is shown by dotted line. It is described by the relation $\sigma = 457 \varepsilon^{0.27}$. Hence stress-strain curve for drawn tube is much above stress-strain curve for annealed steel. This difference is caused by considerable strain hardening of drawn tube material.

3. Determination of tube properties in the circumferential direction

Ring specimens of 20 mm in width were cut out from tube and quadratic grids were made on the outer surfaces of rings. Tensile tests of ring specimens were carried out by means of special experimental set up shown in Figure 3. Teflon tape between specimen and moving inserts decreased frictional resistance what resulted in relatively high uniform elongation of the rings. Figure 4 presents the distribution of circumferential strain in the ring. Deformation of the grid was found by the same analysis of video images as described in chapter 2.

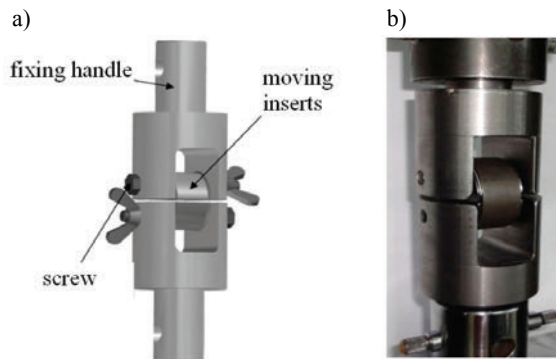


Fig. 3. Schematic presentation of grips used for tensile test of ring specimens (a) and a view of ring specimen placed over moving inserts (b)

It is clearly shown in Figure 4 that the maximum strains were obtained in the parts of ring adjacent to parting face of inserts. Finally, stress-strain curves for rings were found, Figure 5.

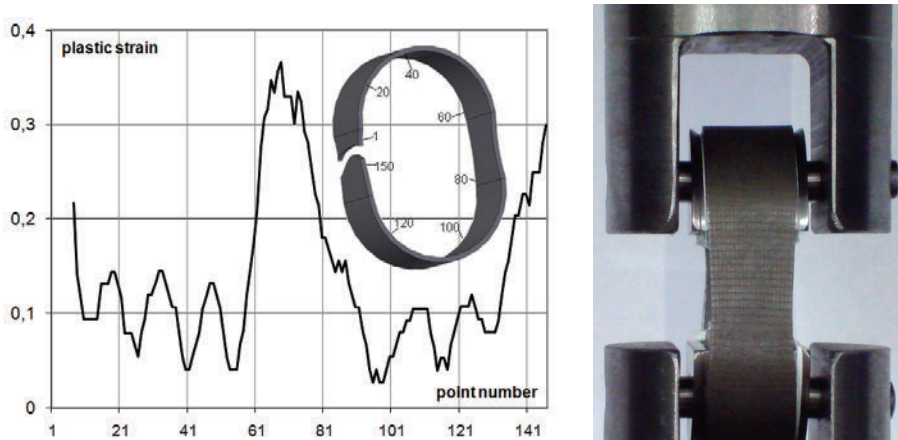


Fig. 4. Distribution of circumferential strain in the ring

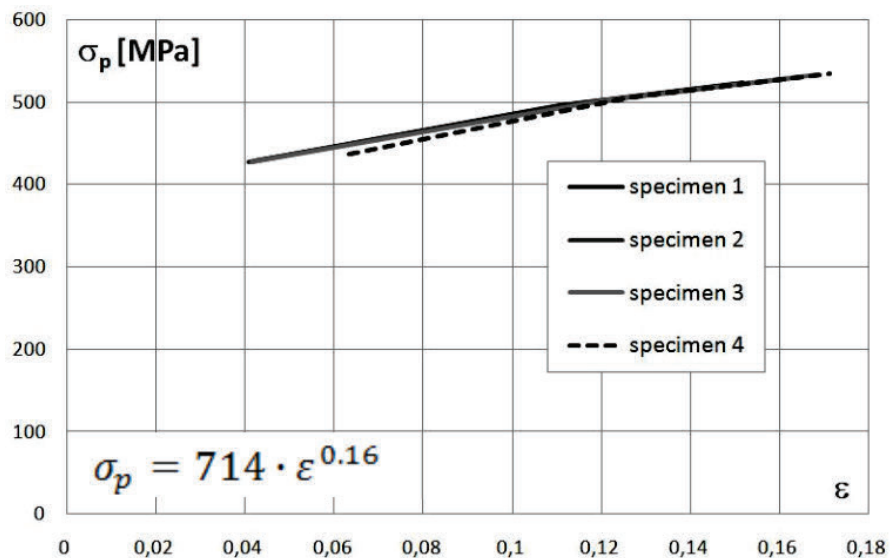


Fig. 5. Stress-strain curves obtained by means of tensile tests of 4 rings cut out from the tube in circumferential direction

Values of stress-strain curve coefficient were almost the same like in the case of specimens cut out axially from the tube. However, stress-strain curve exponents obtained from tensile tests of rings were much higher ($n = 0.16$). These differences in stress-strain curves obtained for specimens cut out in axial and circumferential directions of the tube should be seriously considered when preparing numerical models for hydroforming of tubes.

4. Concluding remarks

As shown by the results of experiments, determination of material properties of seamless tube cannot be limited to axial direction only. However, determination of the properties in direction different than the axial one is difficult. This problem is especially serious as regarding to preparation of specimens for small diameter tubes.

Tensile test of ring specimens proved to be very helpful in getting new data on material properties of tubes. Longitudinal specimens cut out in the axial direction of tube indicated higher strain hardening effect than ring specimens cut out in the circumferential direction of tube. This difference is related to the production method of such tubes, i.e. to cold drawing process in which material grains are elongated in the axial direction.

Specimens cut out from the tube in longitudinal and circumferential directions have curvature in the gauge area. Experimental method with using analysis of video images of deformed specimens has been very useful to get strain values and next – to obtain strain hardening curves.

The differences in material properties would have a considerable influence on results of numerical simulations. Taking into account these differences should result in more accurate calculated data and would be useful in better understanding of tube hydroforming processes.

Acknowledgements

This research work has been financially supported by the Ministry of Science and Higher Education, grant no. NN508390637.

References

- [1] Ahmeloglu M., Sutter K., Li X.J.: Altan T., *Tube hydroforming: current research, applications and need for training*, Journal of Materials Processing Technology, Vol. 98, 2000, pp. 224–231.
- [2] Strano M, Altan T.: *An inverse energy approach to determine the flow stress of tubular materials for hydroforming applications*, Journal of Materials Processing Technology, Vol. 146, 2004, pp. 92–96.
- [3] Koc M.: *Development of design guidelines for tube hydroforming*, Doctoral Dissertation Enginnering Research Center for Net Shape Manufacturing at Ohio State University, Columbus, OH, USA, 1999.
- [4] Shirayori A., Fuchizawa S., Ishigure H., Narazaki M.: *Deformation behavior of tubes with thickness deviation in circumferential direction during hydraulic free bulging*, Journal of Materials Processing Technology, Vol. 209, No. 10, 2009, pp. 4627–4632.
- [5] Sadłowska H.: *Application of modified forming limit diagram for hydroforming of copper tubes*, Steel Research International, Special Edition, Vol. 1, 2008, pp. 324–331.
- [6] Levy B.S., van Tyne C.J, Stringfield J.M.: *Characterizing steel tube for hydroforming applications*, Journal of Materials Processing Technology, Vol. 150, 2004, pp. 280–289.

- [7] Nickhare C, Weiss M., Hodgson P.D.: *FEA comparison of high and low pressure tube hydroforming of TRIP steel*, Computational Materials Science, Vol. 47, 2008, pp. 146–152.
- [8] Adebrabbo N., Worswick M. at al.: *Optimization methods for the tube hydroforming process applied to advanced high-strength steels with experimental certification*, Journal of Materials Processing Technology, Vol. 209, 2009, pp. 110–123.
- [9] Williams B.W., Worswick M.J., at al.: *Influence of forming effects on the axial crush response hydroformed aluminum alloy tubes*, International Journal of Impact Engineering, Vol. 37, 2010, pp. 1008–1020.
- [10] Bortot P., Ceretti E., Giardini C.: *The determination of flow stress of tubular materials for hydroforming applications*, Journal of Material Processing Technology, Vol. 203, 2008, pp. 381–388.
- [11] Elsenheimer D., Groche P.: *Determination of material properties for hot hydroforming*, Production of Engineering Research Development, Vol. 3, No. 2, 2009, pp. 165–174.
- [12] Cereti E., Braga D., Giardini C.: *Steel and copper flow stress determination for THF applications*, International Journal of Material Forming, Suppl., Vol. 1, 2008, pp. 309–312.
- [13] Velasco R., Boudeau N.: *Tube bulging test: Theoretical analysis and numerical validation*, Journal of Material Processing Technology, Vol. 105, 2008, pp. 51–59.
- [14] Takahashi H, Moro J., Tshida S.: *Plastic anisotropy in aluminum drawn tubes*, Metals and Materials, Vol. 4, No. 3, 1998, pp. 380–385.
- [15] Green D.E.: *Summary report of A/SP hydroforming work*, Industrial Research of Development Institute, 2004.

Własności materiałowe w modelowaniu komputerowym kształtowania hydromechanicznego rur

Kształtowanie hydromechaniczne rur należy do nowoczesnych procesów obróbki plastycznej i jest stosowane ze względu na swoje liczne zalety: materiałoszczędność, zwiększenie sztywności i wytrzymałości elementów, zmniejszenie kosztów produkcji. Kształtowanie hydromechaniczne polega na rozpęczaniu materiału cieczą pod ciśnieniem w celu uzyskania zadanego przez matrycę kształtu. Często w procesach tych stosowana jest również dodatkowa siła osiowa, której zadaniem jest uzyskanie większych odkształceń formowanej rury. Warunkiem prawidłowo zaprojektowanego procesu jest odpowiednie złożenie przebiegu ciśnienia rozpęczającego i siły osiowej w czasie trwania kształtowania. W tym celu wykorzystuje się Metodę Elementów Skończonych, co pozwala obniżyć koszty związane z projektowaniem procesu. Warunkiem zbudowania prawidłowego procesu jest wykorzystanie danych doświadczalnych, a w szczególności danych materiałowych. Uzyskanie tych danych jest utrudnione w przypadku rur, szczególnie jeśli planuje się wykorzystanie rur bezszwowych o niewielkich średnicach. W takim przypadku istnieje potrzeba znalezienia nowych metod określania własności mechanicznych, nie tylko na kierunku osiowym, ale także na obwodzie rury. W referacie została zaprezentowana metoda określania własności mechanicznych rur na kierunku osiowym i obwodowym dla rur stalowych.



Warm forming of stainless steel sheet

F. STACHOWICZ, T. TRZEPIECIŃSKI

Politechnika Rzeszowska, ul. W. Pola 2, 35-959 Rzeszów, Poland.

T. PIEJA

WSK "PZL Rzeszów" S.A., ul. Hetmańska 120, 35-078 Rzeszów, Poland.

The aim of warm sheet metal forming processes is to improve plastic flow of material, as well as to decrease the springback effect. This investigation deals with the effect of temperature in the range from 20 °C to 700 °C on basic material parameters of stainless steel sheet metal such as yield stress, ultimate strength, total and uniform elongation, strain hardening parameters and plastic anisotropy factor. The results of carried out investigations will be useful for deep drawing processes preparation and modification, especially considering proper forming temperature. It was determined that the most suitable temperature of warm forming of the AMS 5604 stainless steel sheet is 500 °C. Examination of the influence of the temperature, sheet thickness and material heating method (only sheet heating, sheet and forming die heating, isothermal conditions) on springback quantity was performed in air bending test. The MSC Marc Mentat commercial computer code was used for numerical simulation of analyzed forming processes.

Keywords: *stainless steel, sheet metal, warm forming, air bending, springback*

1. Introduction

Stainless steel sheets are increasingly used for making different parts because of their high corrosion-resistivity and good appearance. Nevertheless, under cold forming conditions the high content of martensite in such material due to the accumulated strain in forming process brings the rise in working force, the decrease in corrosion-resistivity, the magnetization and the delayed cracking. To avoid the martensitic transformations and omit the annealing process, warm forming is useful, since the martensitic transformation decreases with increasing temperature. This needs make sheet metal forming operations of stainless steel more complex than those performed on other materials because of the increase in number of process parameters affecting the deformation mechanisms at high temperatures. As a matter of fact, the occurrence of microstructural phenomena: grain growth, surface oxidation, friction condition, etc., can make the material sensitive to strain rate and temperature. As a consequence, the prediction of phenomena affecting the accuracy of the final product, such as the springback, that is the partial return of the sheet to its initial shape when forming load is removing, can be very difficult and more complex than the one in cold forming conditions.

Cold forming ($T < 0.35 T_m$) takes advantage of strain hardening to increase the strength of a material at the penalty of higher forming forces, while hot forming ($T > 0.55 T_m$) lowers the yield stress and allows simultaneous recrystallization, which controls the grain size refinement. To avoid high temperatures and forces, warm forming ($0.35 T_m < T < 0.55 T_m$) is used as the intermediate process [1], which allows recovery but not recrystallization. The aim of warm forming is to capitalize on the advantages of both hot and cold forming. The forming temperature affects both the behaviour of the material during deformation, properties and accuracy of finished parts. In comparison to hot forming processes, warm forming requires higher forces because of the greater material flow stress, thus making increased demand on the forming tools and equipment. From the other point of view, greater part accuracy in terms of dimensions, shape and surface finish can be achieved. The optimal temperature for a particular warm forming operation and formed material always represents a compromise. Its lower limit is determined by force which can be produced by the forming machines and by the formability of the material [2–3]. The upper limit is usually determined by the amount of oxidation which can be tolerated. For example the temperature range for warm forming of constructional steel is limited for these reasons to 720–1020 K [4]. At the temperatures typical for warm forming most grades of steel show specific plastic properties. These properties are due to recovery, partially to ageing and possibly to recrystallization, which in these temperatures occur at a definite rate. These effects make the yield stress dependent not only on the current values of temperature, strain and strain rate, but also on the course of the past deformation process, i.e. deformation history. It is also noteworthy to notice that the heat generated during deformation results in a non-uniform temperature field, which in turn affects the process of deformation of material whose properties at such temperatures are specific.

One of the main problems encountered in warm forming is a satisfactory lubricant which has to meet the following criteria: reduction of friction, stability at operating temperature, non-toxic, disinclination to decompose, good adhesion, ease of application, ease of removal, easy to recycle, and low cost. For example graphite-based lubricants have proved particularly suitable and are normally applied onto the tool surface since graphite oxides form above 770 K. But new lubricants and new lubrication methods are under investigation.

To date, there is not enough information in literature concerning sheet metal warm forming processes and temperature influence on mechanical properties of a material. For example some of them are related to stainless steel [1, 5–6] and the rest is related to magnesium alloy [7–12] and aluminium alloy sheet [13–18]. An increase in temperature up to the limit range characteristic for warm forming, up to 300 °C for aluminium alloy [12, 16] and magnesium alloy [12], improves their formability and causes decreasing of springback velocity in the case of air bending process [15]. Magnesium alloy is difficult to be deformed at room temperature for its hexagonal close-packed crystal structure. However, it shows excellent ductility and formability at elevated temperature. Forming of magnesium alloy sheets requires appropriate conditions

such as temperatures and drawing speed [9]. The investigations of aluminium alloys sheets forming have shown that drawability of the hardened materials in a warm forming process are better than the annealed alloys at room temperature, suggesting the possibility of drawing high strength aluminium alloys for structural parts at moderate elevated temperature rather than drawing them in the annealed state and heat-treating after forming [17]. Limited amount of such information in the case of stainless steel sheets was one of the reasons for the investigation presented in this paper.

2. Material and experimental procedure

In order to determine the optimum condition of deep drawing for the AMS 5604 stainless steel sheet (chemical composition: Cr 16.5, Ni 4.0, Cu 4.0, Mn 1.0, Mo 0.5, Si 1.0, Nb 0.3, C 0.07 wt. pct.), the effect of forming temperature on the basic mechanical properties (such as yield stress, ultimate strength, total and uniform elongation, strain hardening parameters and plastic anisotropy factor) of the material was experimentally investigated. Uniaxial tensile test was performed to determine mechanical parameters of the 1.0 mm thick stainless steel at different temperature: 20 °C (room temperature, cold forming conditions), 400 °C, 500 °C, 600 °C, 650 °C and 700 °C. The tensile specimens of 50 mm gauge length and 12.5 mm width were prepared from strips cut at 0°, 45° and 90° according to the rolling direction of the sheet. The tests performed at evaluated temperature were carried out in the protective argon gas atmosphere. The experiments were carried out using a special device which recorded simultaneously the tensile load and the current length of specimen. The strain-stress relation was described employing Hollomon equation in the form of: $\sigma = C\varepsilon^n$, where n is strain hardening exponent and C is strain hardening coefficient.

Some of the specimens were deformed (up to uniform elongation) in order to determine plastic anisotropy coefficient defined as:

$$r = \frac{\varepsilon_w}{\varepsilon_t},$$

where ε_w and ε_t are width and thickness strain respectively.

V-die air bending test was performed on 20 mm wide 1.0 and 1.2 mm thick sheet specimens using simple setup with 25 mm punch diameter (Figure 1). Four different method of specimen heating was applied:

- without heating – cold forming,
- only sheet metal induction heating (Figure 1),
- sheet metal induction heating and forming die flame heating,
- electric heating in isothermal conditions.

Bending temperature was approximately 500 °C. Bending process was performed gradually. For each sheet specimen four different bending depths were applied.

Specimen geometry (bending depth, angle and radius) was determined under loading and after load releasing, when springback phenomenon take place.

The MSC Marc Mentat commercial computer code based on FEM was used for numerical simulation. A fully 3D analysis of the V-die bending was performed. One half of the tooling and sheet blank were modelled using rigid quadrilateral and shell elements, respectively.

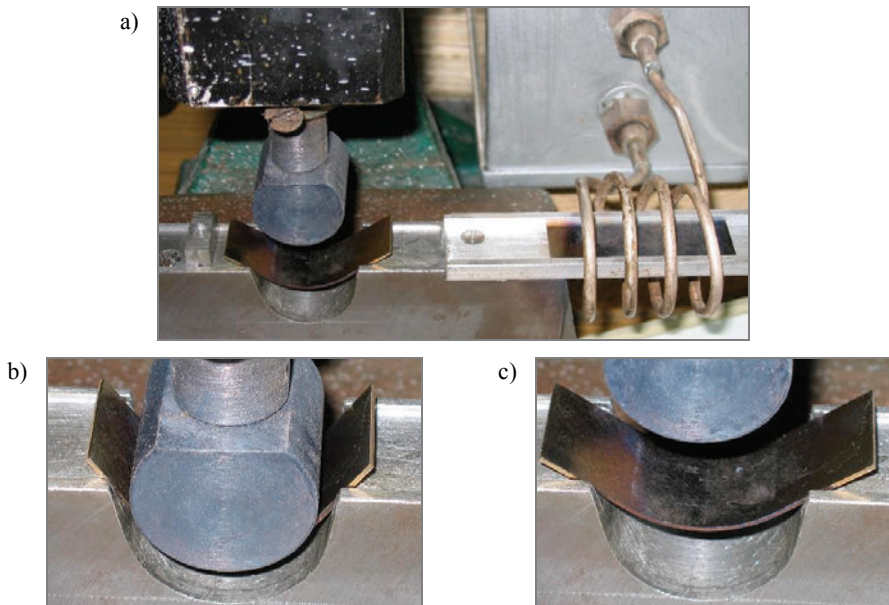


Fig. 1. Bending setup with sheet metal induction heating (a), sheet specimens under bending load (b) and after springback (c)

3. Results and discussion

The results of uniaxial tensile test visibly demonstrate temperature dependence of all determined mechanical parameters (Table 1). The value of strain hardening coefficient C drastically decreases when temperature of deformation increase, at least over 10 times. The specimens deformed at the temperature of 700 °C characterize higher value of plastic anisotropy coefficient than for the specimens deformed at room temperature. In order to make particular relations more visible graphical presentations were performed. The comparison of the uniaxial tensile characteristics obtained in different temperatures (Figure 2) enable for the following remarks:

- the shape of characteristics obtained at the temperature of 20 °C, 400 °C, 500 °C visibly differ from these obtained at the temperature of 600 °C, 650 °C and 700 °C,
- the uniaxial tensile curve obtained at temperature of 600 °C and 650 °C characterizes high value of postuniform elongation,

- the characteristic obtained at the temperature of 700 °C seemed to be typical for material deformed not under warm but under hot conditions.

Table 1. Mechanical parameters of stainless steel sheet obtained in different temperatures

L.p.	Temperature [°C]	R_e [MPa]	R_m [MPa]	A_r	A_{50}	r	C [MPa]	n
1	20	904	1061	0.040	0.058	0.90	3436	0.373
2	400	642	815	0.044	0.059		2607	0.362
3	500	537	694	0.052	0.071	0.96	1346	0.306
4	600	324	464	0.029	0.090		714	0.178
5	650	276	361	0.040	0.117		578	0.149
6	700	173	224	0.118	0.430	1.50	309	0.134

The value of all parameters has been averaged according to: $x = 1/4 (x_0 + 2x_{45} + x_{90})$ where subscripts refer to specimen orientation according to rolling direction

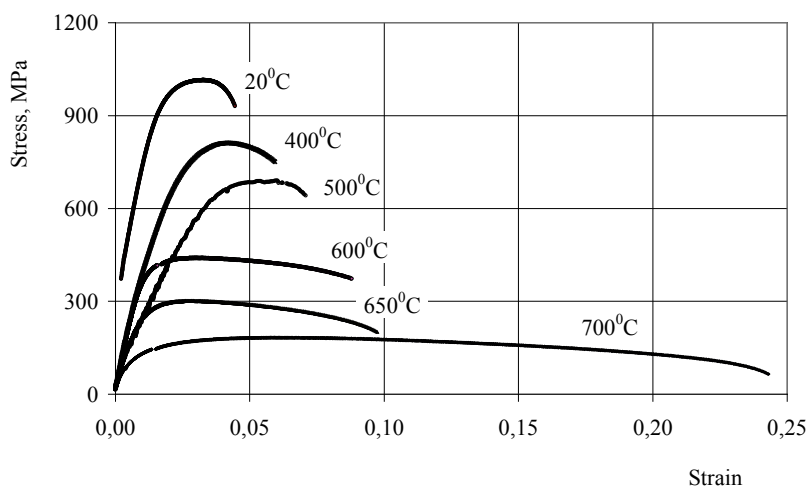


Fig. 2. Comparison of uniaxial tensile characteristics of 1.0 thick AMS 5604 stainless steel sheet obtained at different temperatures

As it was mentioned earlier increasing temperature of the specimen deformation facilitates the improvements of material plasticity. Both the value of yield stress and ultimate strength decrease with temperature of the specimen deformation and for the highest temperature the difference in the value of these parameters become smaller (Figure 3). The value of ultimate elongation increases with temperature of the specimen deformation, especially at the highest temperature. The relation between the temperature of the specimen deformation and uniform elongation is more complicated (Figure 4), the value of this parameter achieves local maximum at the temperature of 500 °C, then decrease and increases again at the temperature of 700 °C. The minimum value of uniform elongation the temperature of 600 °C and of 650 °C could be explained as the result of intensive changes in material structure taking place at this temperature range.

The value of strain hardening exponent (obtained for the uniform elongation range) decrease slowly with the temperature of the specimen deformation up to the temperature of 400 °C (Figure 5) and more rapidly in the higher temperature range. It is noteworthy that a representation of strain-stress relation in double logarithmic coordinate has shown that intensity of strain hardening decreases with elongation for all the specimens and temperatures of deformation.

According to preliminary results the Young modulus value decreases with temperature increasing and amounts 206 GPa at 20 °C and 186 GPa at 500 °C.

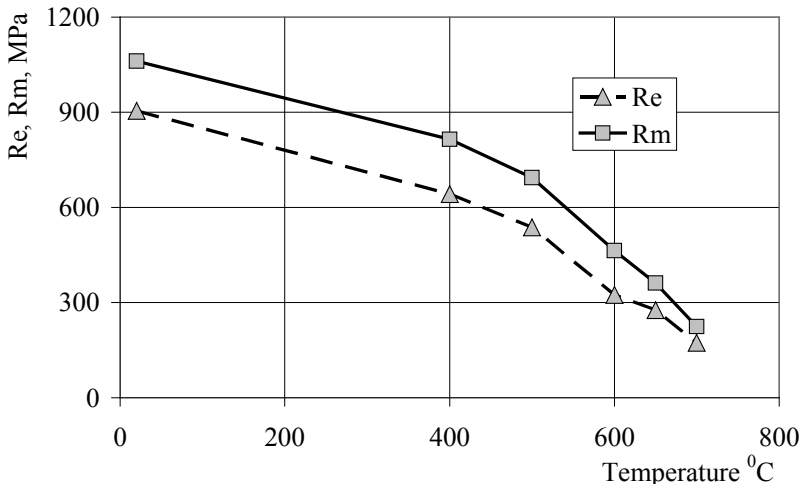


Fig. 3. Yield stress and ultimate strength dependence on testing temperature

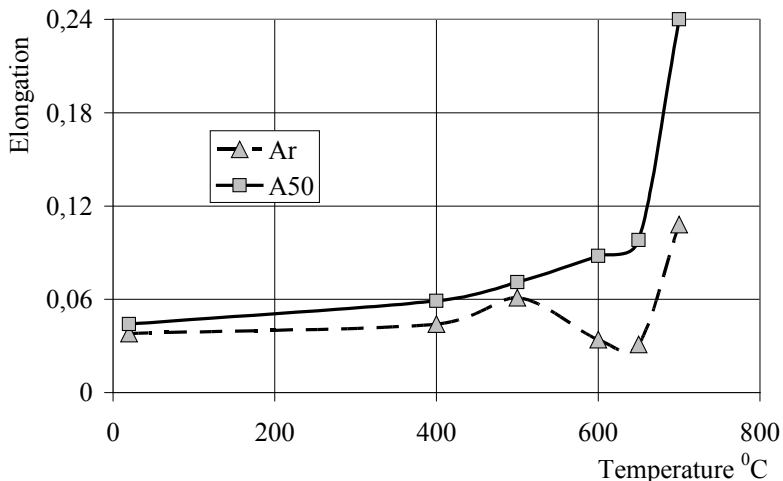


Fig. 4. Uniform and ultimate elongation dependence on testing temperature

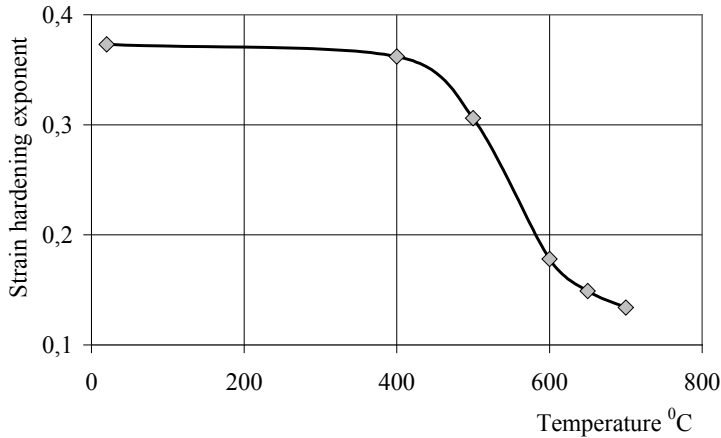


Fig. 5. Strain hardening exponent dependence on testing temperature

As it was expected forming temperature affected springback quantity during sheet specimen bending in the whole range of bending depth (Figure 6). The most efficient reduction of springback was achieved under warm bending in isothermal conditions, when both, the specimen, bending die and punch were placed in closed electric heating room. In the case of warm bending using induction heating of the sheet specimen in open air it was difficult to fulfil temperature regime and the reduction of springback in comparison to cold forming was less evident.

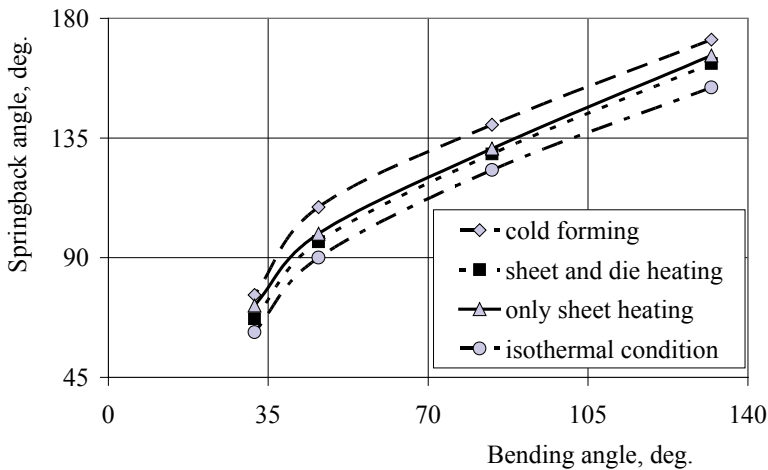


Fig. 6. Bend angle of specimen after springback versus bend angle under load for different bending die heating conditions

Numerical analysis of bending process is based on consideration of the plane strain condition. The finite-element computer code was used to simulate strain distribution

across the sheet thickness and springback coefficient calculation. Because of the symmetry of the plate, only one half portion of the tools and workpiece was modelled. An automatic mesh program was applied in this work to generate the finite-element mesh grid, which is a bilinear quadrilateral element with the selective reduced integration, efficient for sheet metal forming. A modified Coulomb's friction law was employed to treat the discontinuous alternation of the sliding-sticking state of friction at the contact interface. To realize satisfactory lubrication between the tool and the sheet, friction coefficient $\mu = 0.01$ was assumed in the calculation.

Satisfactory agreement between the numerical calculation and the experimental results was obtained in the case of both the warm and cold bending of 1.0 and 1.2 mm thick sheets (Figure 7). In all cases the springback characteristics were nearly linear. Larger value of springback coefficient (defined as the ratio bend radius of specimen under load and after unloading) for 1.2 mm thick sheet specimen resulted from larger plastic zone across sheet thickness. The effect of temperature on springback reduction was more visible for 1.0 mm thick sheet.

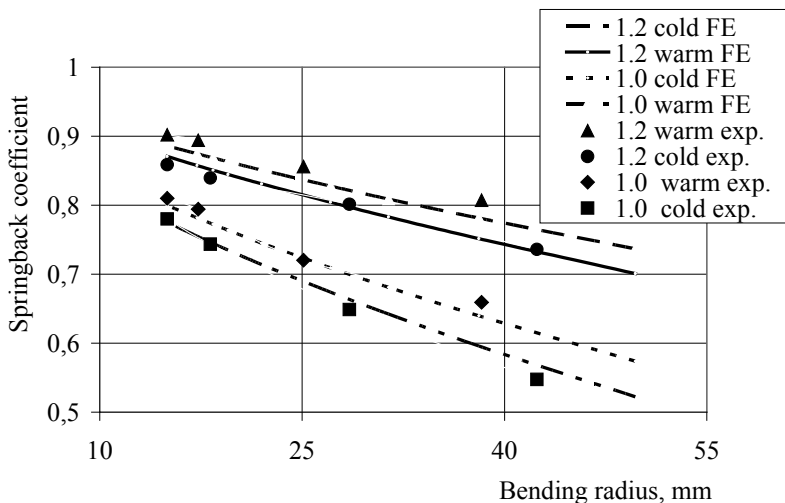


Fig. 7. Springback coefficient as a function of bending radius – comparison between results of experimental measurements (exp.) and numerical simulation (FE) of air bending process under cold (20 °C) and warm (500 °C) conditions for 1.0 and 1.2 mm thick AMS 5604 stainless sheet

4. Conclusions

On the basis of the obtained experimental results we can conclude that the optimal temperature of warm deformation of analyzed stainless steel is the temperature in the range of 500 °C. Material deformed at this temperature is characterized by the highest value of uniform elongation (except for 700 °C temperature which rather belongs to the range of hot forming) which assures satisfactory sheet metal deformation.

In the V-die air bending test the springback amount of both 1.0 and 1.2 mm thick stainless steel sheet show a visible reduction under warm forming at the temperature of 500 °C.

References

- [1] Frechard S., Redjaimia A., Lach E., Lichtenberger A.: *Mechanical behaviour of nitrogen-alloyed austenitic stainless steel hardened by warm rolling*, Materials Science and Engineering, Vol. A415, 2006, pp. 219–224.
- [2] Lange K. (ed.): *Handbook of metal forming*, McGraw-Hill Book Co., New York, 1985.
- [3] Erbel S., Kuczyński K., Marciniak Z.: *Obróbka plastyczna*, PWN, Warszawa, 1981.
- [4] Marciniak Z.: *Non-uniformity of strains in shearing within the warm-forming temperature range*, International Journal of Mechanical Sciences, Vol. 29, No. 10–11, 1987, pp. 721–731.
- [5] Takuda H., Mori K., Masachika W., Watanabe Y.: *Finite element analysis of the formability of an austenitic stainless steel sheet in warm deep drawing*, Journal of Materials Processing Technology, Vol. 143–144, 2003, pp. 242–248.
- [6] Switzer N.T., Van Tyne C.J., Mataya M.C.: *Effect of forging strain rate and deformation temperature on the mechanical properties of warm-worked 304L stainless steel*, Journal of Materials Processing Technology, Vol. 210, 2010, pp. 998–1007.
- [7] Bruni C., Forcellese A., Gabrielli F., Simoncini M.: *Air bending of AZ31 magnesium alloy in warm and hot forming conditions*, Journal of Materials Processing Technology, Vol. 177, 2006, pp. 373–376.
- [8] Sheng Z.Q., Shivpuri R.: *A hybrid process for thin-walled magnesium parts*, Materials Science and Engineering, Vol. A428, 2006, pp. 180–187.
- [9] Chang Q.-F., Li D.-Y., Peng Y.-H., Zeng X.-Q.: *Experimental and numerical study of warm forming of AZ31 magnesium alloy sheet*, International Journal of Machine Tools and Manufacture, Vol. 47, 2007, pp. 436–443.
- [10] Chang J.-K., Takata K., Ichitani K., Taleff E.M.: *Ductility of an aluminium-4.4 wt. pct. magnesium alloy at warm- and hot-working temperatures*, Materials Science and Engineering, Vol. A527, 2010, pp. 3822–3828.
- [11] Kim H.-K., Kim W.-J.: *Failure prediction of magnesium alloy sheets deforming at warm temperatures using Zener-Hollomon parameter*, Mech. Mar., Vol. 42, 2010, pp. 293–303.
- [12] Kurukuri S., Van den Boogaard A.H., Miroux A., Holmedal B.: *Warm forming simulation of Al-Mg sheet*, Journal of Materials Processing Technology, Vol. 209, 2009, pp. 5636–5645.
- [13] Zhang C., Leotoing L., Guines D., Rangneau E.: *Experimental and numerical study on effect of forming rate on AA5086 sheet formability*, Materials Science and Engineering, Vol. A527, 2010, pp. 967–972.
- [14] Takuda H., Mori K., Masuda I., Abe Y., Matsuo: *Finite element simulation of warm deep drawing of aluminium alloy sheet when accounting for heat conduction*, Journal of Materials Processing Technology, Vol. 120, 2002, pp. 412–418.
- [15] Keum Y.T., Han B.Y.: *Springback of FCC sheet in warm forming*, J. Ceramic Res., Vol. 3, No. 3, 2002, pp. 159–165.
- [16] Naka T., Nakayama Y., Uemori T., Hino R., Yoshida F.: *Effects of temperature on yield locus for 5083 aluminium alloy sheet*, Journal of Materials Processing Technology, Vol. 140, 2003, pp. 494–499.

- [17] Li D., Ghosh A.K.: *Biaxial warm forming behaviour of aluminium alloy sheet*, Journal of Materials Processing Technology, Vol. 145, 2004, pp. 281–293.
- [18] Kim H.S., Koc M., Ni J.: *A hybrid multi-fidelity approach to the design of warm forming processes using a knowledge-based artificial neural network*, International Journal of Machine Tools and Manufacture, Vol. 47, 2007, pp. 211–222.

Kształtowanie na półgorąco blachy ze stali odpornej na korozję

Celem procesów plastycznego kształtowania blach na półgorąco jest zwiększenie możliwości plastycznego płynięcia materiału, jak również zmniejszenie wartości powrotnych odkształceń sprężystych. Prezentowane wyniki badań dotyczą wpływu temperatury rozciągania próbek z zakresu 20 °C do 700 °C na wartość podstawowych parametrów mechanicznych blachy ze stali odpornej na korozję, takich jak: granica plastyczności, granica wytrzymałości, wydłużenie równomierne, wydłużenie całkowite, parametry krzywej umocnienia odkształceniowego, współczynnik anizotropii plastycznej. Uzyskane wyniki mogą być przydatne do opracowywania oraz modernizacji procesów plastycznego kształtowania blach, zwłaszcza w zakresie doboru temperatury kształtowania. Określono, że najbardziej odpowiednią temperaturą kształtowania na półgorąco blach ze stali odpornej na korozję AMS 5604 jest temperatura 500 °C. Ocenę wpływu temperatury kształtowania, grubości blachy oraz sposobu nagrzewania (nagrzewana tylko blacha, nagrzewana blacha oraz podgrzewane narzędzia, nagrzewanie izotermiczne w przestrzeni zamkniętej) na wartość powrotnych odkształceń sprężystych przeprowadzono w próbie gięcia swobodnego. Przeprowadzone zostało modelowanie numeryczne analizowanego procesu gięcia przy wykorzystaniu oprogramowania MSC Marc Mentat.



3D elasto-plastic FEM analysis of the sheet drawing of anisotropic steel sheet

T. TRZEPIECIŃSKI

Rzeszow University of Technology, ul. W. Pola 2, 35-959 Rzeszów, Poland.

The article presents the experimental and numerical results of rectangular cup drawing of DC03 cold-rolled steel sheet. The aim of the experimental study was to analyse material behaviour under deformation. The received numerical results were further verified by experimental results. A 3D parametric finite element model was built using the commercial package ABAQUS. If the material and friction anisotropy are taken into account in the numerical model, this approach undoubtedly gives the most approximate numerical results to real processes.

Keywords: *deep drawing, friction anisotropy, material modelling, finite element analysis*

1. Introduction

Knowledge of the deformation mechanisms is important in the design of the drawing operations because deep drawing processes are characterized by nonlinearity both in geometry, material behaviour and nature of contact. In the wall of the forming part may be distinguished regions involved stretching, drawing and various combinations of these basic modes of deformation. The deformation mechanism of rectangular cup drawing is very complicated for a theoretical analysis [1].

Numerical simulation using finite element method (FEM) approach is widely applied in the attempt to have better understanding of sheet metal forming processes. Among others, application of FEM allows predicting the forming defects and provides the knowledge of deformed shape, stress and strain distribution and punch loading. The accuracy of FEM simulation depends on the type and size of elements, type of constitutive equations, description of material behaviour and friction phenomenon. One of the most important elements of numerical simulation is the constitutive equation that usually describes the flow stress as a function of the deformation. The correctness of the material model depends on the mathematical structure of the model and the proper experimental determination of the material properties used in the model [2].

Plastic anisotropy is the result of the distortion of the yield surface shape due to the material microstructural state [3]. The anisotropy is of two types: normal and planar anisotropy. In normal anisotropy the properties differ in the thickness direction; in planar anisotropy however the properties vary with the orientation in the plane of the

sheet. Whereas drawability of sheets increases with normal anisotropy, planar anisotropy leads to the formation of ears in cup drawing [4]. However, after cold forming, the crystallographic directions of a metal gradually rotate towards a common axis thus creating anisotropy in the metal. Various approaches have emerged for developing anisotropic yield criteria. The anisotropic yield criteria proposed by Hill [5–6] does not completely represent the general state of anisotropy, even in plane stress conditions. Hill's criterion is simple to implement, but possesses a certain anomaly. The modified version of his criterion [6] is reported to be free of this defect but does not contain the shear stress term. Generally there are several quadratic and non-quadratic yield criteria which may be associated with isotropic hardening for industrial applications. Hill's yield criterion with the accompanied modifications is most often used for anisotropic model description of steel sheet [7–8]. Habraken [9] has presented reviews of state-of-the-art numerical models in sheet forming analysis dealing with mechanical anisotropy resulting from crystallographic texture.

The frictional behaviour depends on several parameters such as the contact pressure, sliding velocity, tools and sheet surface roughness as well as lubricant conditions. A friction model is completely defined by the friction condition which specify a set of admissible contact forces and the sliding rule which stipulates what directions of sliding are allowed [10]. The origin of this anisotropy can be attributed to two different sources. The first one is the material itself where the anisotropies of the materials constituting the bodies manifest themselves on the contact surface. The second one is technological. The industrial process used to fabricate the bodies can create striations along preferential directions. Currently, there are not so many publications focusing on frictional anisotropy and its implementation in numerical simulations of sheet metal forming processes. Attention should be paid to the work of Hjjaj et al. [10] where isotropic Coulomb's frictional contact law to anisotropic friction conditions with non-associated sliding rule were generalized. Based on a model of rigid anisotropic asperities, a theoretical investigation on friction limit surfaces and sliding rules has been carried out by Mróz and Stupkiewicz [11].

2. Material model

The drawing processes presented in this work were achieved with a form of DC03 cold-rolled steel sheet according to EN 10130. The sheet thickness measured using micrometer was 1 mm. The mechanical properties of the sheet metal have been determined through tensile tests along three directions with respect to the rolling direction. The elastic behaviour is specified in numerical simulations by the value of Young's modulus, $E = 210000$ MPa, and of Poisson's ratio $\nu = 0.3$. The isotropic hardening behaviour implemented in FEM model uses the Hollomon power-type law (1).

$$\sigma = C \cdot \varepsilon^n, \quad (1)$$

where:

C – material constant,

n – the strain-hardening exponent.

Values of C and n were determined by fitting the experimental flow curves from uniaxial tensile tests. Accuracy of approximation of Hollomon law parameters determined by coefficient of determination R^2 was equal 0.978, 0.972 and 0.988 adequate for samples cut at 0° , 45° and 90° according to the rolling direction.

Different material properties working in different directions can have a significant effect on the degree of difficulty of the forming operation. In particular, textures and orientation of the crystal structure to the rolling direction of the sheet metal lead to anisotropic directional behaviour. The anisotropy of plastic behaviour of sheet metals is characterized by the Lankford's coefficient r [3], which is determined by uniaxial tensile tests. The r value is defined as the ratio of the true strain ε_2 in width and the true strain ε_3 in the thickness direction of a specimen. For isotropic materials the normal plastic anisotropy ratio \bar{r} is equal to 1. $\bar{r} > 1$ when the strength in the thickness direction is greater than the average strength in the directions lying in the plane of the sheet. The higher \bar{r} value, the deeper draw can be achieved [3]. The mechanical parameters of DC03 steel sheet are presented in Table 1.

Table 1. Mechanical properties of DC03 steel sheet

Orientation	Yield stress [MPa]	Ultimate tensile strength [MPa]	Material constant C [MPa]	Hardening exponent n	Lankford's coefficient r
0°	162	310	554	0.21	1.55
45°	163	322	542	0.20	1.27
90°	168	312	530	0.21	1.67

The sheet metal exhibits in-plane anisotropy in the yield stress and the r value, while the hardening exponent value is not significantly affected by the sample orientation. The r value in the rolling direction is smaller than measured value in the transverse direction because it is inversely proportional to the thickness strain. The accommodation of strain in the width of the specimen is easier if the basal planes are more tilted to the width direction of the specimen.

3. Friction model

The friction properties of the deep drawing quality steel sheets used in the experiments were determined by using the pin-on-disc tribometer T01-M [12]. The values of friction coefficient were determined in dry friction conditions. To confirm that steel sheets are characterized by the anisotropy of tribological properties, friction anisotropy on a given surface has to be clearly distinguished from friction anisotropy for different perpendicular orientations between the pin and the surface. Variations of friction coefficient value exhibit two maxima for a rotation through 360° . They corre-

spond to the measurement of friction coefficient value transverse to the rolling direction. The anisotropic friction model was implemented by specifying different friction coefficients in two orthogonal directions on the contact surface. These orthogonal directions coincide with the defined slip directions. To use an anisotropic friction model two friction coefficients ($\mu = 0.142$ and $\mu = 0.157$) were specified, where the first is the coefficient of friction in the first slip direction along the rolling direction and second is the coefficient of friction in the perpendicular slip direction. For simulation models with isotropic friction an average friction coefficient value of 0.1495 was received.

As shown in Figure 1, the critical shear stress surface is defined by a piece of ellipse defined by Equation 2.

$$\tau_1 = \tau_1^{\max} \cos \alpha, \quad \tau_2 = \tau_2^{\max} \sin \alpha, \quad (2)$$

where $\alpha \in \left\langle 0, \frac{\pi}{2} \right\rangle$.

This elliptic surface has two extreme points given by $\tau_1^{\text{crit}} = \mu_1 p$ and $\tau_2^{\text{crit}} = \mu_2 p$. The size of ellipse will change with the change in contact pressure between surfaces.

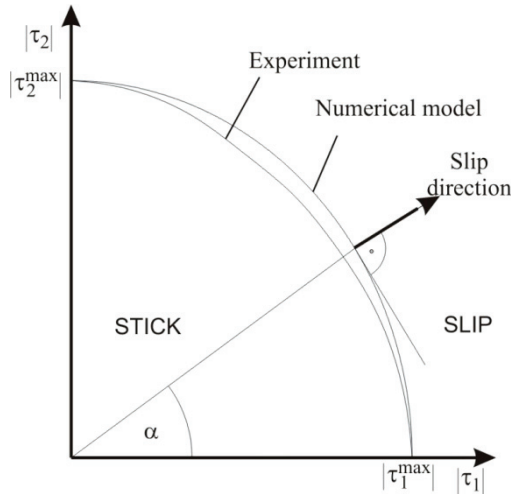


Fig. 1. Anisotropic friction model

4. Experimental procedure

In this experiment, deep drawings of rectangular cups were performed by a device consisting of a die, a punch and a blank holder (Figure 2). The die is a flat surface with a rectangular hole 61.4 mm by 41.4 mm, rounded at the edges with a radius of 2 mm.

The rectangular punch with a size 60 mm by 40 mm is chamfered by an angle of 30° and rounded at the lateral edges with the same 12 mm radius. The die set is constructed of cold-worked NC6 tool steel, hardened to a minimum of 58 HRC. The drawing of cups was run in dry friction conditions. The complete drawing apparatus was conducted within the Schenck UTS 100 hydraulic test machine with forming speed of 0.3 mm/s at a room temperature.

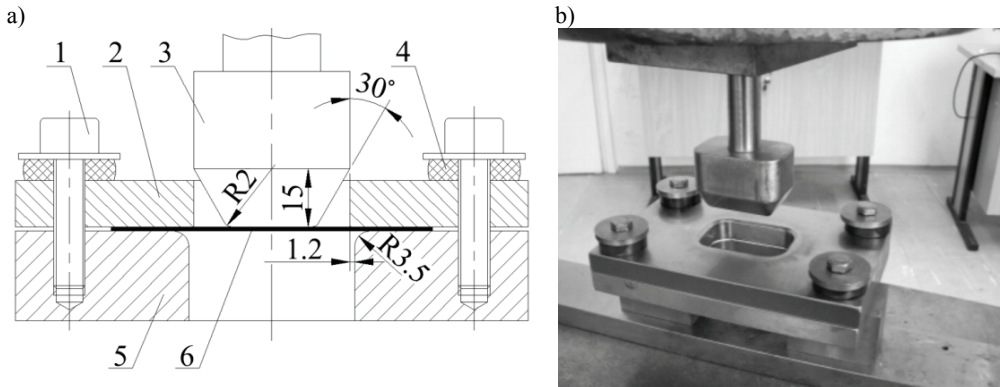


Fig. 2. Dimensions of the stamping tool (a) and view of setup in testing machine (b):
1 – set bolt, 2 blank holder, 3 – punch, 4 – rubber washer, 5 – die, 6 – blank

The trial-and-error method was used to determine the blank shape allowing to determine the final drawpieces with uniform height around the circumference. A starting-point to determine blank shape was rectangular shape with dimensions 92×74 mm rounded by radius $r = 28$ mm. During a deep drawing operation, the blank is subjected to radial stresses due to the blank being pulled into the die cavity and there is also a compressive stress normal to the element which is due to the blank-holder pressure. The radial tensile stresses lead to compressive hoop stresses because of the reduction in the circumferential direction. Unless constrained by the blank-holder, the flange of the blank attempts to wrinkle because of the hoop stress. The force on the blank holder was determined experimentally by trial-and-error method as a necessary minimal force to prevent a wrinkle formation. On the other hand, application of the blank holder increases the frictional resistance in flange region and decreases value of the limit strain of the sheet.

It is most advantageous if the blank holder pressure is varied during stamping by application of variable blank holder force (VBHF) [13]. This pressure improves formability of the sheet and can decrease the maximum tensile stress along the punch direction and the danger for breaking. The used rubber washers allow increasing the blank thickness in blank holder contact region and protecting against wrinkling formation simultaneous. The force to the blank holder was realized by screwing down a bolt with suitable torsion moment. The specimens were carefully positioned at the

center of the die to ensure a uniform distribution of the blank holder force; and the applied blank holder force was kept at 7.85 kN. The walls of the cup primarily practice a longitudinal tensile stress, as the punch transmits the drawing force through the walls of the cup and through the holder as it is drawn into the die cavity. Additional tensile hoop stress is also caused by the cup being held tightly over the punch.

Three cups with different height corresponding to punch strokes of 7 mm, 11 mm, 16 mm were experimentally carried out. Particular cups were cut along three directions with respect to the rolling direction, transverse, longitudinal and at 45° angle. The distribution of thickness was measured along vertical cross section of the cup formed using a microscope device.

5. Numerical model

The blank, die and punch were modelled corresponding to the experimental set-up. Symmetry of the process was utilized in order to reduce the CPU time, i.e., only one quarter of blank and tool with appropriate boundary conditions were modelled. The blank was modelled with 4-node doubly curved shell elements, called S4R in ABAQUS terminology [14]. S4R is a 4-node, quadrilateral, stress/displacement shell element with reduced integration and a large-strain formulation. This shell element type is intentionally applied for analysis of sheet metal forming processes [15], and this element accounts for the change of thickness in its output variables, unlike solid and plane strain elements. The blank model is composed of 3104 4-node elements. The tools were consisted of 9586 linear quadrilateral rigid elements. To prevent wrinkling, uniform blank holder force of 7.85 [kN] corresponding to the experiment was applied on the top surface of a blank holder plate. The boundary conditions applied to the blank holder allow displacement in the normal direction to the blank surface so that the wrinkling formation was prevented and the frictional resistance in flange region was minimized. Penalty formulation of friction contact was used to enforce the intermittent contact and sliding boundary condition between the sheet metal and tools. The contact between the blank and the tools is a standard master and slave contact interface. Both isotropic and anisotropic formulations were considered in the numerical simulations. The sheet material has been treated as an elasto-plastic.

Numerical simulations were performed with material behaviour described by Huber and Misses [16] yield criterion with isotropic hardening and with anisotropic yield condition described by Hill [5]. For ideal case of isotropic materials, Huber-Misses [29] yield condition is expressed as:

$$\bar{\sigma} = \sqrt{\frac{(\sigma_{11} - \sigma_{22})^2 + (\sigma_{22} - \sigma_{33})^2 + (\sigma_{11} - \sigma_{33})^2 + 6(\sigma_{12}^2 + \sigma_{23}^2 + \sigma_{31}^2)}{2}}. \quad (3)$$

As mentioned previously, Hill's [5] formulation is the most frequently used yield function for steel sheet metals. It can be regarded as an extension of the isotropic Huber-

Misses function, which can be expressed in terms of rectangular Cartesian stress components as follows:

$$\bar{\sigma} = \sqrt{(F(\sigma_{22} - \sigma_{33})^2 + G(\sigma_{33} - \sigma_{11})^2 + H(\sigma_{11} - \sigma_{22})^2 + 2L\sigma_{23}^2 + 2M\sigma_{31}^2 + 2N\sigma_{12}^2)} \quad (4)$$

where $\bar{\sigma}$ is the equivalent stress and indices 1, 2, 3 represent the rolling, transverse and normal direction to the sheet surface.

Constants F, G, H, L, M and N are defined anisotropy state of material and are equal:

$$F = \frac{1}{2} \left(\frac{1}{R_{22}^2} + \frac{1}{R_{33}^2} - \frac{1}{R_{11}^2} \right), \quad G = \frac{1}{2} \left(\frac{1}{R_{11}^2} + \frac{1}{R_{33}^2} - \frac{1}{R_{22}^2} \right), \quad H = \frac{1}{2} \left(\frac{1}{R_{11}^2} + \frac{1}{R_{22}^2} - \frac{1}{R_{33}^2} \right), \quad (5)$$

$$L = \frac{3}{2R_{23}^2}, \quad M = \frac{3}{2R_{13}^2}, \quad N = \frac{3}{2R_{12}^2}.$$

Parameters $R_{11}, R_{22}, R_{33}, R_{12}, R_{13}, R_{23}$ are defined in ABAQUS as user inputs consisting of ratios of yield stress in different directions with respect to a reference stress according to Equation 6.

$$R_{11} = \frac{\sigma_{11}}{\sigma_0}, \quad R_{22} = \frac{\sigma_{22}}{\sigma_0}, \quad R_{33} = \frac{\sigma_{33}}{\sigma_0}, \quad R_{12} = \frac{\sigma_{12}}{\tau_0}, \quad R_{13} = \frac{\sigma_{13}}{\tau_0}, \quad R_{23} = \frac{\sigma_{23}}{\tau_0}, \quad (6)$$

6. Results and discussion

In order to investigate the variations in the wall thicknesses of rectangular cups, several experiments were carried out through gradual increment of the punch displacement. While forming at each grade, thickness distribution was separately investigated. The formation process of the conical wall of the drawpiece satisfied a condition of free stretching of the drawpiece side-wall. Although bending tensions occur on the plate with the first contact of the punch on the sheet plate, these tensions transform into drawing and pressing tensions while moving the punch towards the deeper sections. Furthermore, friction forces appear due to the contact of the sheet plate with the punch and die, and only drawing and bending tensions occur at sections with no contact. With the penetration of the punch into the die, only drawing tensions play an active role at sections of the sheet plate that remains within the die. Verification of numerical results in characteristic sections was then carried out on the basis of the measurements of wall thickness of the drawpieces. Parts formed to examine the thickness changes after the stamping experiments were cut along the rolling and transverse directions starting from the centre of the part. Furthermore, the cups were cut in the corner at an angle of 45° with respect to the rolling direction (Figure 3). The cut sides are trimmed and the changes of thickness were measured by using an optical microscope. The measurement in rolling and transverse directions does not cause dif-

difficulties because the nodes under the whole forming process are in the symmetry plane. Besides rectangular shape of the punch and non-axisymmetrical shape of the blank material, the friction anisotropy caused position changes of the nodes in corner cup relative to the perpendicular plane of the blank and inclined angle of 45° with respect to the rolling direction.

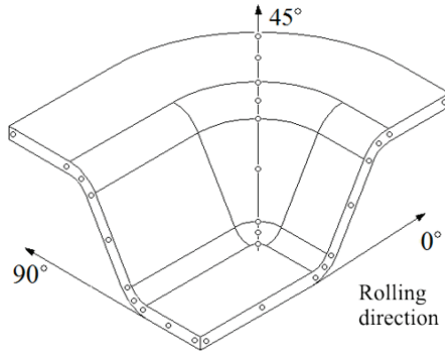


Fig. 3. Scheme of measurement points of wall thickness

The thickness strain distributions along 0° , 45° and 90° directions referred to the rolling direction are shown in Figures 4–6. Three deformed profiles determined for true distance along each path were compared with experimental measurements. As expected, the thickness strain distributions are different along these directions for all punch displacements. The decisive impact on this character exerts the non-axisymmetrical shape of parts. The thickness distribution of the sheet under the punch is found to be more or less uniform to the initial sheet thickness.

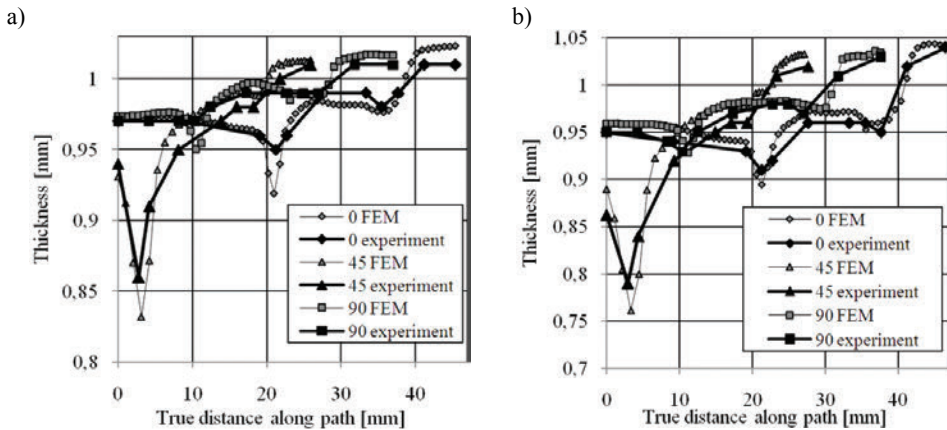


Fig. 4. Plot of thickness strain (Hill model + anisotropic friction) under punch displacement of 11 mm (a) and 16 mm (b)

However, the thickness of the sheet, which was above the flat portion of the die, is observed to be slightly larger than the initial thickness. The thickness measured in the rolling direction (the long side) is smaller than that from the transverse direction (the short side) near the punch shoulder. The main reason for this effect is the unsymmetrical shape of the process, where a higher fraction of radial tension stress exists along the short wall of the rectangular drawpiece along the long side wall. Other studies [17] also show that the short side of wall of the rectangular drawpiece near the punch edge is the most expose to the fracture.

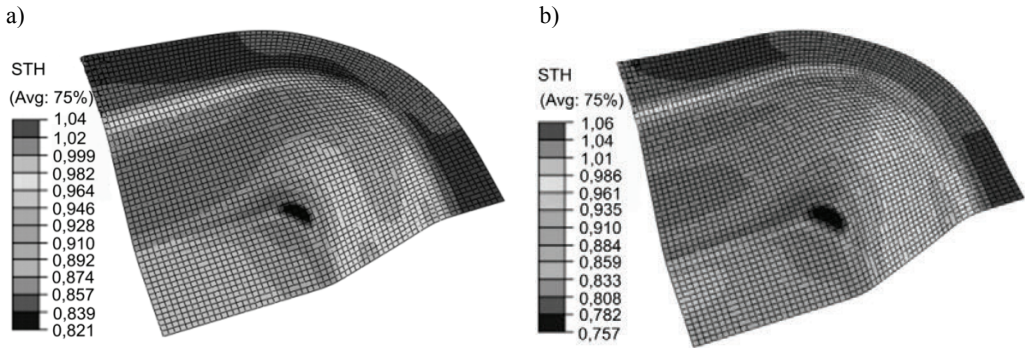


Fig. 5. Contour of the sheet thickness (Hill model + anisotropic friction) under punch displacement of 11 mm (a) and 16 mm (b)

The wall thickness varies especially in the corners and the maximum magnitude of the thickness strain for all analysed cases is observed along 45° . Apart from the fact that the neck which develops on the radius of the punch is more pronounced than in experiments, the strain distributions are well described by the FEM simulations. The thickness of sheet metal below the die corner is less than the initial thickness and the variation character is different in different directions. There is a nonlinear dependence of thickness strain with the punch displacement. The minimum thickness usually occurs in the portion of the sheet which is closer to the punch profile radius region. In the final configuration (Figure 6) the minimal thickness is almost 79% of the initial thickness.

Thickness of flat wall of the drawpiece formed by punch bottom decreases until the punch force reaches a maximal value. After exceeding the peak value, the wall thickness of the bottom remains constant until the forming process was finished. Compared with the other parts of drawpiece, the bottom part experiences a small variation of the thickness with punch displacement. Moreover, the thickness distribution is more uniform for different models and this is depicted in Figures 5–6. Thickness in flange region measured in the rolling direction is higher than in the remaining directions. Compared with the long side of the flange, there exists a major fraction of circumferential compression stress in the short side of drawpiece which causes increment of deformation resistance and as a result of major thickening.

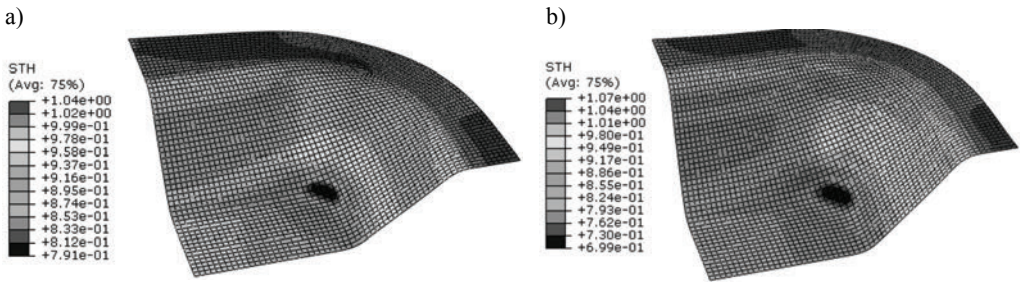


Fig. 6. Contour of the sheet thickness (Huber-Mises model + anisotropic friction) under punch displacement of a) 11 mm, b) 16 mm

The distributions of wall thickness measured and calculated at the end of drawing on the symmetrical lines of long and short sides and the diagonal line passing through the corner, are shown in Figure 7. The good predictive capability of the proposed Hill anisotropy model plus anisotropic friction (AF) has been demonstrated. Compared with deformation on the corner, the variation of thickness at bottom of drawpiece is relatively small. Replacement of anisotropy friction model by isotropic friction (IF) model in both models of material causes slight decrease in thickness. It is also clearly visible that the character of the thickness variation is similar at the bottom of drawpiece. In other parts of drawpiece this phenomenon is more complicated. Moreover the largest difference between analysed models exists at the corner. The thickness variation in the drawpiece wall measured along the diagonal line passing the corner is almost identical for all FEM models. For Huber-Mises material model with IF model, the difference between experimental and numerical data of maximal thickening in risk section were measured at 0° and 90° from the rolling direction.

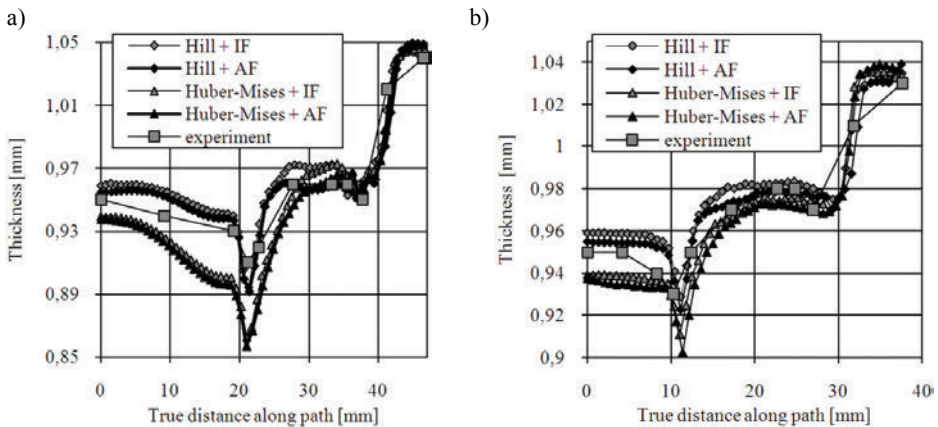


Fig. 7. Plot of thickness strain under punch displacement of 16 mm measured in the rolling (a) and transverse (b) direction

7. Conclusions

This study has attempted to investigate the anisotropy problem in sheet metal drawing using both experimental and numerical approach. Hill's yield criterion was implemented in the material description of the numerical model. Together with friction anisotropy condition, this model gave simulation results that can better approximate the experimental measurements. It is considered that distribution of wall thicknesses obtained by means of experiments and FEM includes material and friction anisotropy generally demonstrates a great harmony, and that minor differences are due to the fact that conditions in the finite elements method are considered ideal. Although the simulated thickness in the flange area along all directions is slightly overestimated, the agreement between predicted and experimental thickness distributions is generally excellent. Plastic anisotropy of sheet material is the main factor that determines high conformity of the numerical simulation results with the reality. Additionally, consideration of the anisotropy of resistance to friction slightly influences the numerical results on variation of the thickness and strain distribution compared with isotropic friction model.

References

- [1] Daxin E., Takaji M., Zhiguo L.: *Stress analysis of rectangular cup drawing*, Journal of Materials Processing Technology, Vol. 205, No. 1–3, 2005, pp. 469–475.
- [2] Gronostajski Z.: *The constitutive equations for FEM analysis*, Journal of Materials Processing Technology, Vol. 106, No. 1, 2000, pp. 40–44.
- [3] Banabic D., Bunge H.-J., Pohlandt K., Tekkaya A.E.: *Formability of metallic materials*, Springer-Verlag, Berlin–Heidelberg–New York, 2000.
- [4] Van Houutte P.: *Anisotropic plasticity*, [in:] Hartley P., Pillingar I., Sturgess C. (eds.): *Numerical modelling of material deformation process: research, development and applications*, Springer-Verlag, London, 1992.
- [5] Hill R.: *A theory of the yielding and plastic flow of anisotropic metals*, Proceedings of the Royal Society of London, Vol. 193, 1948, pp. 281–297.
- [6] Hill R.: *Theoretical plasticity of textured aggregates*, Mathematical Proceedings of the Cambridge Philosophical Society, Vol. 85, 1979, pp. 179–191.
- [7] Tikhovskiy I., Raabe D., Roters F.: *Simulation of earing of a 17% Cr stainless steel considering texture gradients*, Materials Science and Engineering A, Vol. 488, No. 1–2, 2008, pp. 482–490.
- [8] De Magalhães Correia J.P., Ferron G., Moreira L.P.: *Analytical and numerical investigation of wrinkling for deep-drawn anisotropic metal sheets*, International Journal of Mechanical Sciences, Vol. 45, No. 6–7, 2003, pp. 1167–1180.
- [9] Habraken A.M., Duchêne L.: *Anisotropic elasto-plastic finite element analysis using a stress-strain interpolation method based on a polycrystalline model*, International Journal of Plasticity, Vol. 20, No. 8–9, 2004, pp. 1525–1560.
- [10] Hjjaj M., Feng Z.-Q., de Saxe G., Mróz Z.: *On the modelling of complex anisotropic frictional contact laws*, International Journal of Engineering Science, Vol. 42, No. 10, 2004, pp. 1013–1034.

- [11] Mróz Z., Stupkiewicz S.: *An anisotropic friction and wear model*, The International Journal of Solids and Structures, Vol. 31, No. 8, 1994, pp. 1113–1131.
- [12] Stachowicz F., Trzepieciński T.: *Frictional resistance during car body sheet metal forming* (in Polish), Mat. Konf. SAKON, Przecław, 2003, pp. 297–302.
- [13] Zhang X., Long S., Ma Z., Pan Y., Zhou Y.: *Cup-drawing formation of steel sheet with nickel coating by finite element method*, Trans. Nonferrous Met. Soc. China, Vol. 17, 2007, pp. 37–40.
- [14] *ABAQUS version 6.7 – Theory Manual*, Inc., Hibbit, Karlsson & Sorenson, Dassault Systemes, 2007.
- [15] da Rocha A.B., Santos A.D., Teixeira P., Butuc M.C.: *Analysis of plastic flow localization under strain paths changes and its coupling with finite element simulation in sheet metal forming*, Journal of Materials Processing Technology, Vol. 209, No. 11, 2009, pp. 5097–5109.
- [16] Von-Mises R.: *Mechanik der festen Körper im plastisch deformablen Zustand*, Nachr. Ges. Wiss. Göttingen, Vol. 1, 1913, pp. 582–592.
- [17] Trzepieciński T., Stachowicz F.: *Numerical modelling of a process of forming rectangular drawpieces* (in Polish), Rudy Metale, Vol. 50, No. 10–11, 2005, pp. 582–585.

Sprężysto-plastyczna analiza 3D procesu wytłaczania blach stalowych anizotropowych za pomocą MES

W pracy przedstawiono wyniki badań eksperymentalnych oraz symulacji numerycznych procesu kształtowania wytłoczek z blachy stalowej głębokotłoczonej. Celem badań eksperymentalnych była analiza płynięcia materiału pod wpływem deformacji plastycznej. Otrzymane wyniki symulacji numerycznych zostały zweryfikowane z wynikami eksperymentalnymi. Model numeryczny 3D, bazujący na metodzie elementów skończonych, zbudowano w programie ABAQUS. Uwzględnienie w modelu numerycznym anizotropii plastycznej materiału oraz anizotropii tarcia warunkuje otrzymanie wyników bardziej zbliżonych do wyników rzeczywistego procesu kształtowania.



The influence of heat treatment on selected physical properties of aluminized steel strips

K. ŻABA

University of Science and Technology, al. Mickiewicza 30, 30-059 Kraków, Poland.

The selected examinations of physical properties of the aluminised steel strips intended for elements of exhaust systems are characterized in the paper. Strips in their initial state and after the heat treatment, at temperatures from 250 to 700 °C for 30 to 1440 minutes, were investigated. The macro and microscopic observations of the surface of the coating before and after heating are presented. The most of attention was dedicated to investigations of the erosion resistance in a stream of solid particles, simulating the behaviour of the coating exposed to various kinds of fine-grained particles. The results are presented as the mass losses, changes of the coating thickness and observations of the effect of the abrasive-penetrating agent. Examinations of microhardness and microscopic observations at the cross-section of the coating were also performed.

Keywords: *Al-Si coating, erosion resistance in a stream of solid particles, microhardness*

1. Introduction

Steel strips with Al-Si coating [1–3] are applied, among others, in household appliances and in an automotive industry. Elements of exhaust systems operate within a wide temperature range [4]. An influence of a heat treatment in a broad exposure range: air environment, vacuum and neutral gases, on changes in the coating and intermetallic layer thickness, in geometric structure of the coating surface, as well as the limit time values for materials being exposed to a certain temperature without any danger of unfavourable changes occurring in the coating (at taking into account the given coating thickness) was documented by the published investigation results [5–15].

However, until recently, certain essential elements were omitted in examinations. These are physical properties of coatings before and after a heat treatment, with a special emphasis on their abrasion resistance. Taking into account the character of operations of exhaust systems, being exposed to influences of various fine-grained elements (stones, sands and others), the performance of examinations of the influence of the heat treatment parameters of the aluminised steel strips on their erosion resistance in a stream of solid particles – was decided. In order to determine the influence of the heat treatment on structural changes and related to them resistance to abrasive-penetrating agents the examinations of the microhardness of coatings were performed. Changes on the coating surface and its cross-section are documented by macro and microscopic observations.

2. Experimental technique

Steel strips of the DX52D+AS120 type, 1.5 mm thick, with a double-sided aluminium-silicon alloy coating (18–23 μm thick) containing app. 10% of silicon, made by an immersion method, were examined. The chemical composition of the strip is presented in Table 1.

Table 1. Chemical composition of strip (wt. %)

C	Mn	Si	P	S	Cr	Ni	Nb	Cu	Al	Fe
0.004	0.15	0.007	0.009	0.011	0.02	0.022	0.014	0.017	0.045	Bal.

Strips were cut into samples of dimensions 50 \times 50 mm. Then samples were exposed to a heat treatment at temperatures from 250 to 700 $^{\circ}\text{C}$, every 50 $^{\circ}\text{C}$, for 30, 180 and 1440 minutes. The heat treatment was realized in the laboratory chamber furnace, in the air atmosphere. The furnace was heated to the needed temperature, and then samples were placed inside it. Samples were heated for the determined time and then air cooled to a temperature of app. 23 $^{\circ}\text{C}$. Three samples were used for each variant of the heat treatment. For a comparative purpose samples without any heat treatment were also examined. The obtained results are presented as macro and microscope observations.

Next, the samples were subjected to erosion resistance examinations in a stream of solid particles. The device used for these examinations is schematically presented in Figure 1.

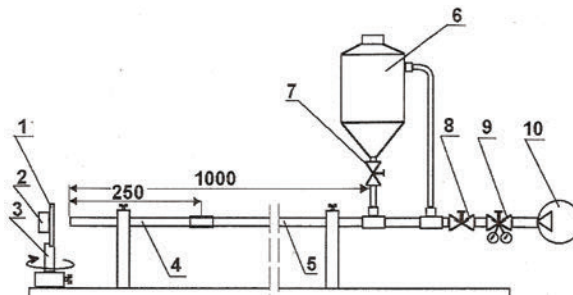


Fig. 1. Schematic presentation of the device for the erosion resistance examinations in a stream of solid particles: 1 – sample clamp, 2 – sample, 3 – rotational flange of a sample clamp, 4 – ceramic nozzle, 5 – steel pipe, 6 – container of abrasive material, 7 – valve with a flange, 8 – cut-off valve, 9 – reducer, 10 – compressor

Samples, before and after the heat treatment, were cut for dimensions 25 \times 25 mm. They were degreased in the ultrasound washer in $\text{C}_2\text{H}_5\text{OH}$ solution, dried and weighted on the laboratory scale. Then samples were placed in the special device for erosion resistance examinations. The corundum powder, in an amount of 2 g for each test, was applied as an abrasive material. After fastening of the samples the compressed

air jet ejecting the corundum powder with a velocity of 1 m/s was switched on. Samples were placed at an angle of 90° versus the abrasive material. After testing each sample was washed, dried and weighted in the same devices. The mass loss, the sample surface condition and the coating thickness were determined. The quantitative results are presented in diagrams, while surface observations, made by means of the MULTIZOOM AZ 100 microscope of the Nikon Company. The thickness of the coating was measured by a non-destructive method, performing 10 measurements and calculating their arithmetic mean.

The microhardness of coatings before and after the heat treatment was investigated to determine structural changes. Tests were performed on samples, which remained after cutting the ones for the erosion resistance examinations. Microhardness was tested by the Vickers method [16] by means of the metallographic optical microscope Zeiss Neophot with the Hanemann's device assembled. In this apparatus a diamond cone is directly built into the upper lens of the objective. All tests were performed at the same load, which enabled the direct comparison of results. The load was equal to 0.4903N (50g). 10 measurements of microhardness of coating on each sample were done. Averaged results are presented in the form of the diagram.

In order to display the coating and base structures the samples were observed in the microscope. Strip samples with a silumin coating were mechanically cut. Then metallographic micro-sections were prepared from each sample. These microsections were made by means of ROTOPOL 11 of the Struers Company. Samples were immersed in EPOFIX resin of the Struers Company. Then the samples were grinded on abrasive papers of a gradation of 220–1000 μm . Next, they were polished on polishing wheels with an application of diamond suspensions of a gradation 15, 9, 6, 3 and 1 μm . Structure observations of Al-Si coatings and bases were performed by using the scanning microscope HITACHI 3500N (SEM).

3. Results and discussion

3.1. Results of the surface observation of samples before and after the heat treatment

Examples of the results of the coating surface observation before and after the heat treatment are presented in Figure 2.

The influence of the temperature and time of the heat treatment is in a certain range very distinct. Up to a temperature of 450 °C the heat treatment time has no influence on the surface appearance. The surface of the coating (Figure 2b) does not differ from the surface in the initial state (Figure 2a). The surface is bright, silvery with a distinct gloss. Partial changes on the coating surface appear in the temperature range 500–600 °C. The coating – in several, not regular areas – changes into darker and matt (Figure 2c). This differentiation – as indicated by tests – is caused by an uneven coating thickness. Where the coating is thinner the darker and matt areas occur, while the thicker coating retains its bright

colour. In temperatures of 650–700 °C, in the applied time interval, the whole coating surface is dark, matt and porous – regardless of the thickness of the coating (Figure 2d).

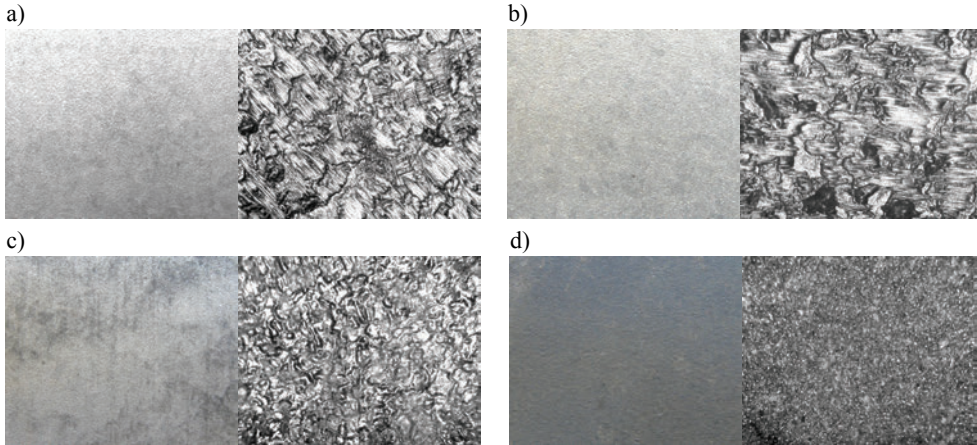


Fig. 2. Macro- and microscopic observation of the surface of the Al-Si coating after heat treatment
a) Initial state, b) 250 °C – 1440 min, c) 600 °C – 30 min, d) 700 °C – 180 min

3.2. Results of the erosion resistance examinations in a stream of solid particles

The results of the observation of coatings, both in their initial state and after the heat treatment, after the erosion resistance examinations in a stream of solid particles are presented in Figure 3.

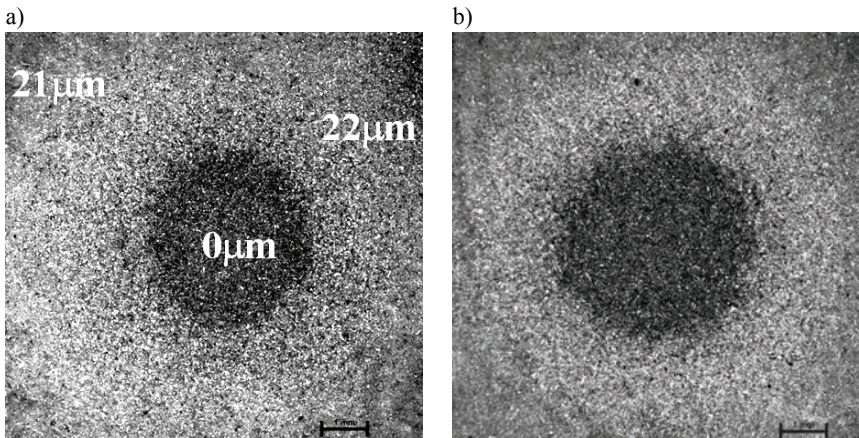


Fig. 3. The results of the observation of coatings, both in their initial state and after the heat treatment, after the erosion resistance examinations in a stream of solid particles:
a) Initial state, b) 450–180

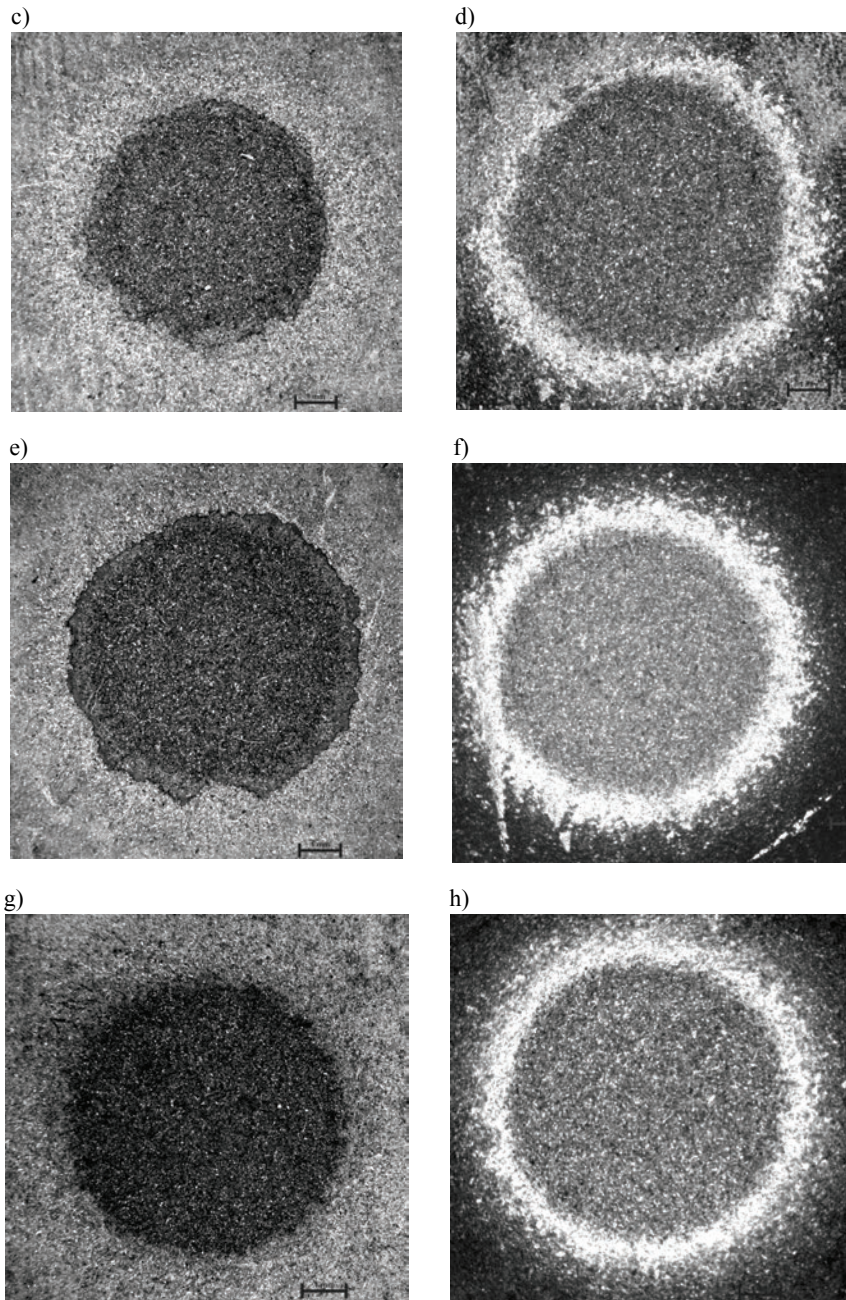


Fig. 3. The results of the observation of coatings, both in their initial state and after the heat treatment, after the erosion resistance examinations in a stream of solid particles:
c) 500-180, d) 500-1440, e) 550-30, f) 550-1440, g) 600-30, h) 600-180

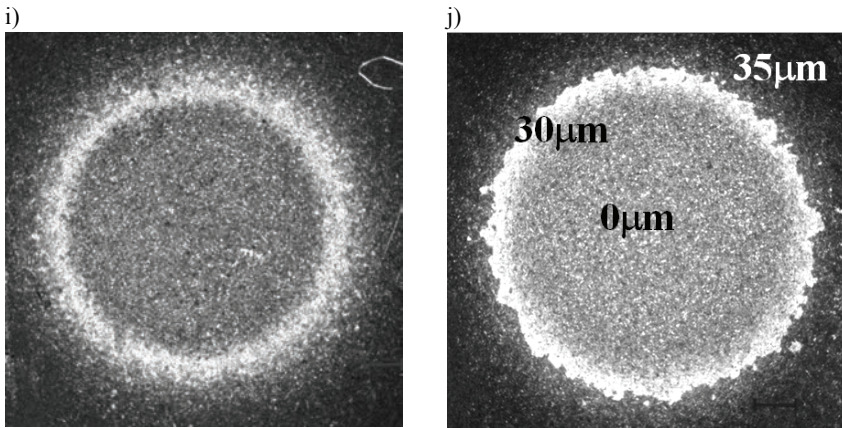


Fig. 3. The results of the observation of coatings, both in their initial state and after the heat treatment, after the erosion resistance examinations in a stream of solid particles: i) 700–180, j) 700–1440

The obtained results of the coating observation, after the erosion resistance examination in a stream of solid particles, indicate an occurrence of two areas being a result of the penetrating agent influence. The first area – of a nearly circular shape – is found in the middle part of the sample, while the second area – of a ring shape – is surrounding the first one. The total diameter of both areas, regardless the heat treatment parameters, is contained within: $D = 8.2\text{--}9.2$ mm. However, there is a significant difference in dimensions of these areas. The first area was exposed to the highest force and amount of the penetrating agent and depending on the heat treatment conditions has various diameters. For samples with a bright and glassy coating surface, it means for samples either without any heat treatment or heat treated only up to a temperature of 450 °C, in the whole time interval, the diameter of rubbed out places equals: $d = 3.5\text{--}5$ mm (Figure 3a–b). Whereas for samples of a dark and matt coating surface, it means for samples exposed to the heat treatment at a temperature of 550 °C for 1440 minutes, of 600 °C for 180 and 1440 minutes and at a temperature of $650\text{--}700$ °C in the whole time interval, the diameter of the rubbed out place is within: $d = 6.3\text{--}7.2$ mm (Figure 3f, h–j). An interesting situation occurs for the samples exposed to the heat treatment at a temperature of 500 °C in the whole time interval, at 550 °C for 30 and 180 minutes and at 600 °C for 30 minutes (Figure 3c–e, g). The surface of the coating – exposed to these conditions – is either still bright or partially covered by darker areas. The diameter of the first area is within: $5.8\text{--}7$ mm (larger values are for samples with dark areas). The abrasive-penetrating agent completely removes the coating from the first area. Thus, for samples with a dark and matt coating, for which diameters of rubbed out places are large, areas without coating are larger than for samples with a bright coating. This is related to the characteristic brittleness of the coating, which was heat treated at a high temperature for a long time, as compared to the soft plastic coating, which has no changes in its surface appearance.

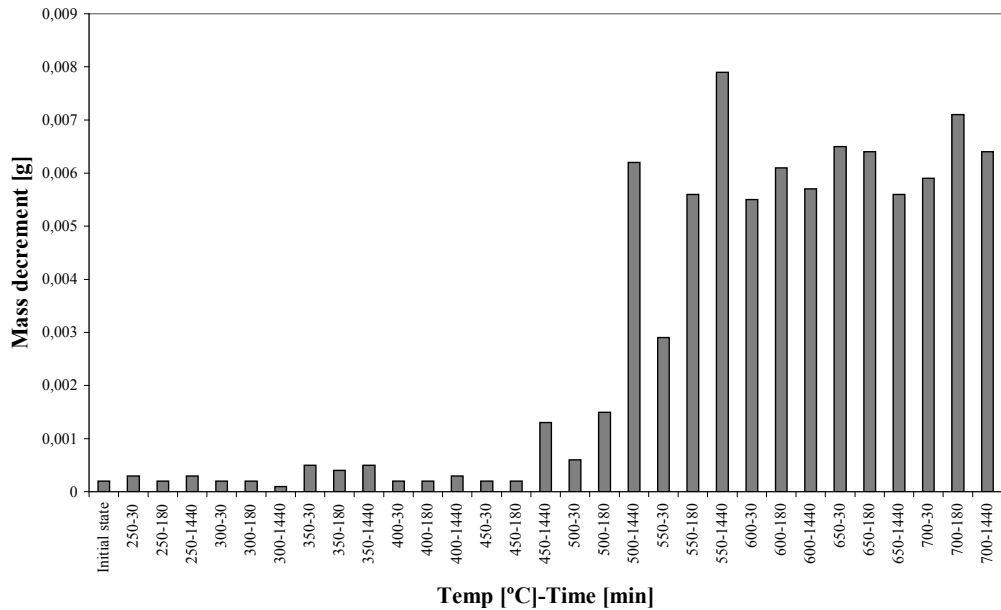


Fig. 4. Mass loss of samples subjected to the examination of the erosion resistance in a stream of solid particles

A width of the second area, in a form of a ring surrounding the first one, varies also in dependence of the temperature-time exposure conditions. It is larger ($L = 1.8\text{--}2.5$) for samples, which are not changed in their surface appearance. A brighter colour of this area as compared to the first area is quite characteristic. The thickness of the coating in this area is similar to the thickness after the heat treatment without any penetrating agent. A lack of distinct changes in the coating thickness in the second area corresponds to the decreased influence of the penetrating agent and to the high plasticity of the coating. The situation is different for samples exposed to the heat treatment, after which their coating surface becomes partially or fully dark and matt. In these cases the ring width $L = 0.9\text{--}1.2$ mm. The surface of the ring is significantly brighter not only than the surface of the first area – which is obvious – but also than the surface of the coating, which was not exposed to the penetrating agent. The reason of colour changing is a decisively weaker influence of the penetrating agent, which causes tearing off the dark and very brittle upper surface layer, but does not remove the remaining part of the coating. The thickness of the coating in the second area constitutes app. 80–90% of the thickness of the coating after the heat treatment.

Characteristics differences in sizes of the areas and thickness of the coating after examination of the erosion resistance in a stream of solid particles are reflected in mass losses of samples (Figure 4). The mass loss is quite small for samples, which coating surface appearance was not changed after the heat treatment, while it is significantly larger (by app. 40–70%) for samples of a dark and matt surface.

3.3. Results of the observations of the coating structure at the cross-section

The results of the observations of the coating structure at the cross-section – after the heat treatment – are presented in Figure 5. The coating in its initial state and after the heat treatment at temperatures up to 450 °C, in the whole time interval, as well as at a temperature of 500 °C for 30 and 180 min., is marked by the characteristic double layer structure. The first layer of a thickness app. 5–7 μm , adhering to the base, constitutes alloy phase: Al-Fe-Si. The second layer constitutes the main Al-Si coating, of a thickness app. 13–16 μm (Figure 5a, c). The heat treatment, performed at a temperature of 500 °C for 1440 minutes, at 550 °C for 30 and 180 minutes and at 600–700 °C in the whole time interval, changes this double-layered coating into the single-layer three-component coating. The analysis of the chemical composition of the coating after a multi-variant heat treatment is presented in references [13–14].

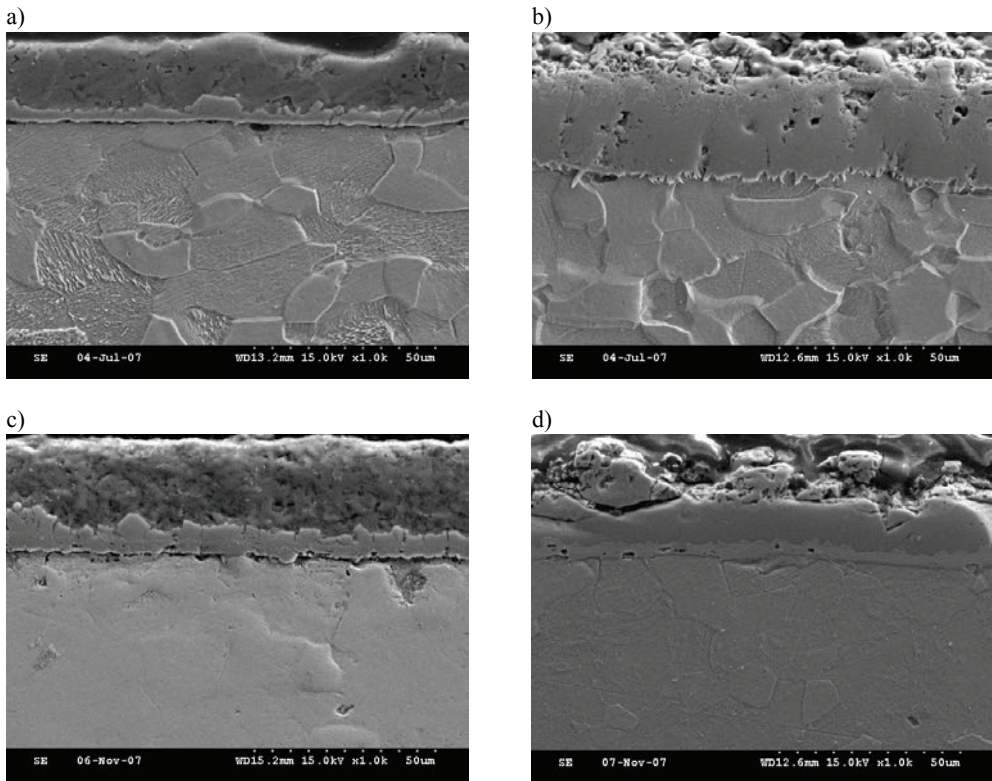


Fig. 5. Results of the observations of the coating structure at the cross-section: a) 250–1440, b) 500 °C – 1440 min, c) 550 °C – 30 min, d) 650 °C – 1440 min

Carbon and nitrogen are bound by niobium in the base material. A low percentage content of carbon is worth mentioning (Table 1) since it causes a lack of a eutectoid

transformation (ferrite and not numerous dispersive niobium carbides are present in a microstructure). Therefore during heating only the transformation of ferrite into austenite will take place in the material – however at higher temperatures than used in these investigations. This feature creates the possibility of the aluminised steel strip application in a wide temperature range. An attention should be directed to the fact, that the low carbon and elements strengthening solution (manganese, silica) content will cause a lower strength but accompanied by a higher plasticity of the material, which results in making it susceptible for forming. The lack of the eutectoid transformation will favour a higher adhesion of the Al-Si coating to the base, since – during heating – there will not be any abrupt expansion change of the base material.

The base microstructure constitutes ferrite of a grain size 7, acc. to ASTM (Figure 5a). During heating, in a temperature range of 250–700 °C for 30–1440 minutes, no significant changes in the ferrite grain size were observed in the steel strip microstructure (Figure 5b–d).

3.4. Results of the microhardness examinations of the coating

The obtained results of the microhardness examinations of the Al-Si coating before and after the heat treatment are presented in Figure 6.

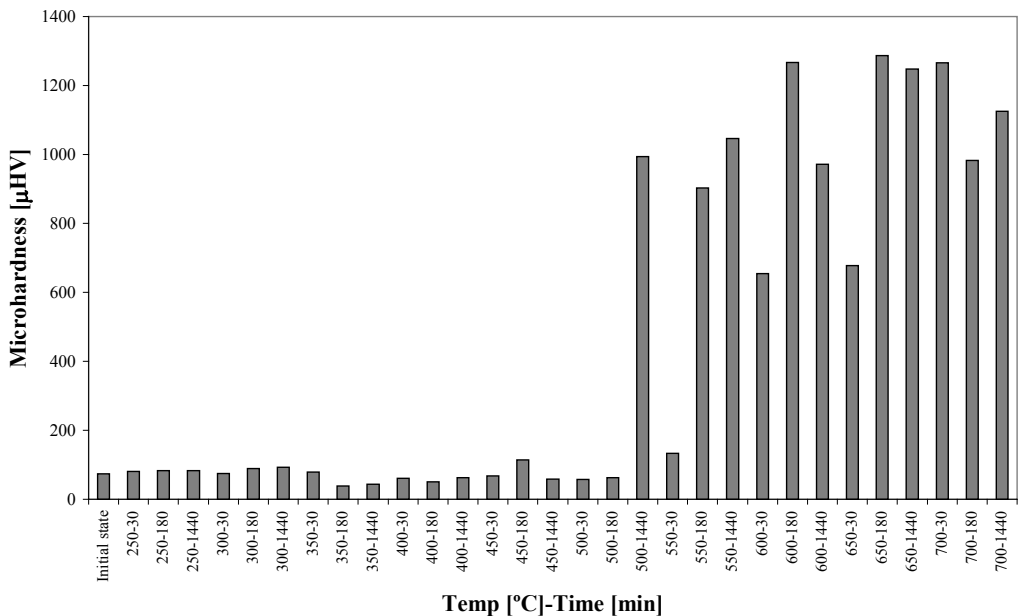


Fig. 6. Results of the microhardness

A diversified microhardness of the coating in dependence on the heat treatment temperature and time is quite characteristic. At the temperatures up to 450 °C in the

whole time range and at a temperature of 500 °C for 30 and 180 minutes as well as at a temperature of 550 °C for 30 minutes the coating microhardness is at a similar level (50–130 μHV). This microhardness range indicates that the coating is very soft and plastic. The obtained results can be correlated both with the state and appearance of the coating surface – bright and silvery, and with the structure of the coating consisting of the distinct very thin transient Al-Fe-Si layer and the main Al-Si coating. Taking into consideration the erosion examinations at the background of the coating microhardness, one can come to the conclusion that certain amount of the penetrating agent – in a form of corundum – stuck into the soft coating and remains visible as a bright second area.

The samples heat treated at a temperature of 500 °C for 1440 minutes, 550 °C for 180 and 1440 minutes and at temperatures 600–700 °C in the whole time range, which surface is dark and matt are characterized by a significant increase of the coating microhardness, being app. 650–1300 μHV . In this case there is also the correlation between the heat treatment parameters and the appearance and structure of the coating. It changes from the double layer form to the single layer three-component Al-Fe-Si form. In spite of its high hardness, in the analysed temperature-time range of the heat treatment, the coating is very brittle. This feature is the reason, that the coating is not resistant to effects of the abrasive-penetrating agent applied in the abrasion resistance investigations, which is reflected by the surface of the coating observation results and the diagram of the sample mass loss.

4. Summary

The obtained results of examinations of the influence of the heat treatment parameters on the selected physical properties of the aluminised steel strips are presented in the paper. The influence of the temperature-time exposure on surface and structural changes of the Al-Si coating, on changes of a microhardness and erosion resistance in a stream of solid particles was investigated in detail. Examinations were performed in a temperature range 250–700 °C, every 50 °C for 30, 180 and 1440 minutes.

The following conclusions can be drawn on the bases of the analysis of the obtained results:

- 1) The investigations proved that the surface and structural changes in the coating are strictly correlated with the influence of various parameters of the applied heat treatment.

- 2) The heat treatment up to a temperature of 550 °C, nearly in the whole time interval, does not change an appearance, structure and microhardness of the coating. The double-layered coating consisting of the main Al-Si coating and the diffusive Al-Fe-Si layer – in between the coating and the base – is soft (app. 100 μHV) and plastic.

- 3) The heat treatment at temperatures of 600–700 °C changes the coating appearance from bright and silvery into dark and matt and causes changes in its structure. The double-layered coating turns into the single three-component Al-Fe-Si

layer of an increased microhardness (even up to 1300 μHV), and also of an increased brittleness.

4) Investigations of the erosion resistance in a stream of solid particles, simulating an influence of small particles on external surfaces of exhaust systems, indicate a diversified resistance of the coating to effects of an abrasive-penetrating agent, manifesting itself by a significant loss of the coating, heat treated at temperatures of 600–700 °C.

5) Investigations of the erosion resistance indicate the possibility of wearing out of the Al-Si coating in elements of exhaust systems exposed to temperatures above 600 °C, generating a danger of the local loss of the corrosion resistance.

References

- [1] ASTM A463/A463M – 06: *Standard specification for steel sheet, aluminium-coated, by the hot-dip process.*
- [2] ASM Handbook: *Surface engineering*, ASM International, Handbook Committee, Vol. 5, 1994, pp. 346.
- [3] EN 10346:2009: *Continuously hot-dip coated steel flat products. Technical delivery conditions.*
- [4] Inoue Y., Kikuchi M.: *Present and future trends of stainless steel for automotive exhaust system*, Nippon Steel Technical Report, No. 88, 2003, pp. 62–69.
- [5] Kawase H., Takezoe A.: *Peeling of coated metal due to severe press-forming in aluminized steel sheet*, Transactions of the Iron and Steel Institute of Japan, Vol. 22, No. 5, 1982, pp. 371–376.
- [6] Kobayashi S., Yakou T.: *Control of intermetallic compound layers at interface between steel and aluminium by diffusion-treatment*, Materials Science and Engineering: A, Vol. 338, No. 1–2, 2002, pp. 44–53.
- [7] Żaba K., Nowak S., Kaç S., Wróbel M.: *Research on temperature time and atmospheric impact on Al-Si coat of low-carbon steel strips*, International Conference: *Problems of modern techniques in aspect of engineering and education*, Pedagogical University of Cracow, Institute of Technology – Cracow, Monography, 2006, pp. 73–78.
- [8] Wang Chaur-Jeng, Chen Shih-Ming: *The high-temperature oxidation behaviour of hot-dipping Al-Si coating on low carbon steel*, Surface and Coatings Technology, Vol. 200, No. 22–23, 2006, pp. 6601–6605.
- [9] Gul Hameed Awan, Faiz ul Hasan: *The morphology of coating/substrate interface in hot-dip-aluminized steels*, Materials Science and Engineering: A, Vol. 472, No. 1–2, 2007, pp. 1–9.
- [10] Kee-Hyun Kim, Van-Daele Benny, Van-Tendeloo Gustaaf, Young-Sug Chung, Jong Kyu Yoon: *Analysis of the intermetallic compound formed in hot dip aluminized steel*, Advanced Materials Research, Vol. 15–17, 2007, pp. 159–163.
- [11] Gul Hameed Awan, Faiz ul Hasan: *The morphology of coating/substrate interface in hot-dip-aluminized steels*, Materials Science and Engineering: A, Vol. 472, No. 1–2, 2008, pp. 157–165.
- [12] Wang Deqing: *Phase evolution of an aluminized steel by oxidation treatment*, Applied Surface Science, Vol. 254, No. 10, 2008, pp. 3026–3032.

- [13] Żaba K., Kać S.: *Badania efektów działania wysokiej temperatury, czasu i atmosfery na użytkowe własności powłoki Al-Si na stalowych rurach przeznaczonych na elementy układów wydechowych*, Rudy i Metale Nieżelazne, Vol. 53, No. 11, 2008, pp. 694–704.
- [14] Żaba K.: *The influence of annealing temperature and time on the structure and features of the Al-Si coatings on steel sheets, purposed for pressured welded pipes applied in exhaust systems*, Archives of Civil and Mechanical Engineering, Vol. 6, No. 2, 2006, pp. 145–152.
- [15] Żaba K.: *The influence of temperature and time of exhibition on a change of Al-Si coating thickness and surface texture on the steel plates*, Archives of Metallurgy and Materials, Vol. 55, No. 1, 2010, pp. 151–162.
- [16] PN-EN ISO 4516:2004 *Powłoki metalowe i inne nieorganiczne. Badania mikrotwardości metodą Vickersa i Knoopa*.

Wpływ obróbki cieplnej na wybrane właściwości fizyczne aluminiowanych taśm stalowych

W artykule scharakteryzowano wybrane badania własności fizycznych, aluminiowanych taśm stalowych, przeznaczonych m. in. na elementy układów wydechowych. Badaniom poddano taśmy w stanie bez i po obróbce cieplnej w temperaturze 250–700 °C w czasie 30–1440 min. Przedstawiono obserwacje makro i mikroskopowe powierzchni powłoki przed i po nagrzewaniu. Najwięcej uwagi poświęcono badaniom odporności na erozję w strumieniu cząstek stałych, symulujących zachowanie się powłoki narażonej na działanie różnego rodzaju elementów drobnoziarnistych. Wyniki przedstawiono w postaci ubytku masy, zmian grubości powłoki oraz obserwacji po działaniu czynnika ścierno-penetrującego. Wykonano także badania mikrotwardości oraz obserwacji mikroskopowych powłoki na przekroju.

